Durham University

Durham E-Theses

Manipulation of ultracold atoms using magnetic and optical fields

Pritchard, Matthew J.

How to cite:

Pritchard, Matthew J. (2006) *Manipulation of ultracold atoms using magnetic and optical fields*, Durham theses, Durham University. Available at Durham E-Theses Online: http://etheses.dur.ac.uk/2373/

Use policy

The full-text may be used and/or reproduced, and given to third parties in any format or medium, without prior permission or charge, for personal research or study, educational, or not-for-profit purposes provided that:

- a full bibliographic reference is made to the original source
- a link is made to the metadata record in Durham E-Theses
- the full-text is not changed in any way

The full-text must not be sold in any format or medium without the formal permission of the copyright holders.

Please consult the full Durham E-Theses policy for further details.

Academic Support Office, The Palatine Centre, Durham University, Stockton Road, Durham, DH1 3LE
e-mail: e-theses.admin@durham.ac.uk Tel: +44 0191 334 6107
http://etheses.dur.ac.uk

Manipulation of ultracold atoms using magnetic and optical fields

Matthew J. Pritchard

A thesis submitted in partial fulfilment
of the requirements for the degree of
Doctor of Philosophy

Department of Physics
University of Durham

September 2006

The copyright of this thesis rests with the author or the university to which it was submitted. No quotation from it, or information derived from it may be published without the prior written consent of the author or university, and any information derived from it should be acknowledged.

29 NOV 2006

Manipulation of ultracold atoms using magnetic and optical fields

Matthew J. Pritchard

Abstract

The loading and guiding of a launched cloud of cold atoms with the optical dipole force are theoretically and numerically modelled. A far-off resonance trap can be realised using a high power Gaussian mode laser, red-detuned with respect to the principal atomic resonance (Rb 5s-5p). The optimum strategy for loading typically 30% of the atoms from a Magneto optical trap and guiding them vertically through 22 cm is discussed. During the transport the radial size of the cloud is confined to a few hundred microns, whereas the unconfined axial size grows to be approximately 1 cm. It is proposed that the cloud can be focused in three dimensions at the apex of the motion by using a single magnetic impulse to achieve axial focusing.

A theoretical study of six current-carrying coil and bar arrangements that generate magnetic lenses is made. An investigation of focusing aberrations show that, for typical experimental parameters, the widely used assumption of a purely harmonic lens is often inaccurate. A new focusing regime is discussed: isotropic 3D focusing of atoms with a single magnetic lens. The baseball lens offers the best possibility for isotropically focusing a cloud of weak-field-seeking atoms in 3D.

A pair of magnetic lens pulses can also be used to create a 3D focus (the alternate-gradient method). The two possible pulse sequences are discussed and it is found that they are ideal for loading both 'pancake' and 'sausage' shaped magnetic/optical microtraps. It is shown that focusing aberrations are considerably smaller for double-impulse magnetic lenses compared to single-impulse magnetic lenses.

The thesis concludes by describing the steps taken towards creating a 3D quasi-electrostatic lattice for ^{85}Rb, using a CO_2 laser. The resulting lattice of trapped atoms will have a low decoherence, and with resolvable lattice sites, it therefore provides a useful system to implement quantum information processing.

Declaration

I confirm that no part of the material offered has previously been submitted by myself for a degree in this or any other University. Where material has been generated through joint work, the work of others has been indicated.

Matthew J. Pritchard
Durham, 21st September 2006

The copyright of this thesis rests with the author. No quotation from it should be published without their prior written consent and information derived from it should be acknowledged.

Acknowledgements

I'm very grateful to my joint supervisors Charles Adams and Ifan Hughes. Their passion for physics has been an inspiration. Their wealth of knowledge has been invaluable.

The majority of what I have learnt these past years has been through the interaction with other AtMol group members. Thanks to the three Simons, Robert, Nick and Griff for answering many questions. To Dave and Graham, your assistance was appreciated, your friendship highly valued. Special thanks to Kev, lab partner and the person who bore the brunt of my eccentricities on a daily basis. I hope you can iron out all the creases I put in the experiment and make some nice physics.

I'd also like to thank the physics department's technical support groups for their expertise they've shared with me over the years. Thanks to the personnel in: Audio Visual, Electronics, Engineering, Finance, UG teaching labs and Computing. Away from Durham, links with Strathclyde University have been fruitful. Aidan Arnold has been a constant source of new ideas and Mathematica fixes. Erling Riis and Robert Wiley have helped with the vacuum chamber design and construction.

Outside the world of physics (yes, it does exist!) I have enjoyed the friendship, support, guidance and fellowship from numerous people. Thanks to Mildert MCR for making me feel normal, Durham Improv for making me laugh and Kings Church massif for making it together. To my parents, your love and belief these last 25 years has been immense. And finally...thanks God.

"The fear of the LORD is the beginning of knowledge, but fools despise wisdom and discipline."

Proverbs 1v7

Contents

List of Figures

List of Tables

Chapter 1

Introduction

"I think I could, if I only knew how to begin. For, you see, so many out-of-the-way things had happened lately that Alice had begun to think that very few things indeed were really impossible." Lewis Carroll

When the laser was first invented in 1960 it was described as "a solution looking for a problem." It has since become arguably one of the most significant and widely used measurement tools of the 20th century. The atom-laser interaction provides a powerful way of controlling and probing the properties of matter. The ability to laser cool atoms, ions and molecules to ultracold temperatures started a scientific revolution that is going from strength to strength [1, 2]. Research labs around the world routinely cool down atoms to μK temperatures [3]. This has led to the production of new forms of matter: Bose-Einstein Condensates (BEC) [4, 5], and quantum degenerate Fermi gases [6]. Furthermore, an atom is a very sensitive probe of the external world. This fact is exploited in measuring weak magnetic [7] and gravitational [8, 9] fields, and is used in producing the most accurate atomic clocks [10, 11]. Another important application of ultracold atoms is in Quantum Information Processing (QIP), whereby neutral atoms are used as qubits, one of the basic building block of quantum computers [12, 13, 14].

1.1 Atom optics

Whatever use ultracold atoms are put to, there is a need for tools and techniques to manipulate them in a non-destructive manner. One of the goals in the field of atom optics is to realise atom-optical elements that are analogues of conventional optical devices, such as mirrors, lenses and beam-splitters [15, 16]. An atom mirror reverses the component of velocity perpendicular to the surface and maintains the component parallel to the surface. An atom lens can modify both the transverse velocity component and the longitudinal component. It is now possible to drastically modify the centre-of-mass motion of atoms, in direct contrast with the small angular deflection of fast beams studied prior to the development of laser cooling [17]. Four main types of interactions have been used to focus ultracold atoms and molecules: matter, electric, magnetic, and light.

1.1.1 Matter interactions

The interaction with other matter has historically concentrated on diffracting atoms off structures. Building on Stern's work on atoms diffracting off crystal structures in the 1930s [18, 19] and later micro-fabricated periodic structures [20], a Fresnel zone plate was used to achieve atom focusing in 1991 [21]. A different focusing approach involves reflecting hydrogen atoms off a liquid helium-vacuum interface [22]. Nowadays focusing using matter interactions has largely been abandoned due to the large atom number losses suffered, however some work on Helium scattering off atomic mirrors continues [23, 24].

1.1.2 Electric field interactions

The interaction between an inhomogeneous electric field and an atom's induced, or a heteronuclear diatomic molecule's permanent, electric-dipole moment can be used for focusing. Making use of static electric fields Gordon *et al.* focused ammonia molecules [25]. In 1999 Maddi *et al.* demonstrated slowing, accelerating, cooling and bunching of molecules and neutral atoms using time varying electric field gradients [26]. The use of this technique is a very active field of

research [27, 28, 29], with particular applications in measuring a permanent electron electric-dipole moment [30].

1.1.3 Magnetic field interactions

The magnetic dipole moment of paramagnetic atoms interacts with a magnetic field. If there is a spatial variation in the field, a force arises called the Stern-Gerlach force (see ref. [31] for a review of magnetic manipulation of cold atoms). To date, the Stern-Gerlach force has been used to realise flat atomic mirrors [32, 33, 34], curved atomic mirrors [35, 36, 37, 38], and pulsed mirrors for both cold (thermal) [39] and Bose condensed atoms [40, 41, 42]. It has also been demonstrated that the surface of a magnetic mirror can be adapted in real time with corrugations that can be manipulated in times shorter than the atom-mirror interaction time [43, 44].

An atomic beam was focused in 1951 by Friedburg and Paul using a hexapole magnetic field [45, 46]. Over 30 years later the first laser-cooled atomic beam was focused using an electromagnetic lens in 1984 [47]. Developing this further, two lenses built from strong rare-earth permanent magnets were used to increase the atomic flux density of a laser-cooled atomic beam [48].

The first demonstration of 3D focusing using pulsed magnetic lenses was conducted in 1991 by Cornell *et al.* [49]. The group of Gorceix have made experimental and theoretical studies of cold atom imaging by means of pulsed magnetic fields [50, 51, 52]. However, neither group addressed the optimum strategy for achieving a compact focused cloud, nor the limiting features for the quality of their atom-optical elements. As well as achieving a compact cloud in space, it is also possible to use pulsed magnetic fields to reduce the momentum spread of an expanding cloud with appropriate magnetic impulses. This can be viewed as an implementation of δ-kick cooling, which has been demonstrated with atoms [53, 54], ions [55] and BECs [40, 41, 42].

It is also possible to load atoms into a magnetic trap, and transport the atoms whilst they are still trapped into a new position. Greiner *et al.*'s scheme involves an array of static coils, with the motion of the trapped atoms facilitated by time-dependent currents in neighboring coils in the chain [56]. There are some drawbacks to this scheme - a large number of coils and power supplies are

required. Care must be taken to preserve the shape of the magnetic trap as it is transferred which necessitates a complex time sequence of currents to be maintained. Another scheme uses coils mounted on a motorised stage, so that they can be easily moved, thereby transporting the magnetically trapped atoms [57, 58, 59]. These experiments used a three dimensional quadrupole trap, which has a magnetic zero at its centre. For certain applications a trap with a finite minimum is required, and this year transport of atom packets in a train of Ioffe-Pritchard traps was demonstrated [60].

1.1.4 Light field interactions

As will be explained in Chapter 2, the atom-light interaction leads to two distinct forces that act on an atom. The dissipative scattering force arising from the absorption and spontaneous emission of light can lead to cooling; first proposed in 1975 [61, 62]. In 1985 Chu *et al.* demonstrated what is now called 'laser cooling' by cooling an atomic gas in 3-dimensions [63]. The addition of a magnetic field, creating a magneto-optical trap, allowed both the cooling and trapping of atoms [64]. Although an excellent method of collecting and trapping cold atoms, the incoherent and dissipative process is undesired in atom optics.

The second atom-light force is the optical dipole force which arises from the interaction between the atom's electric dipole moment and an inhomogeneous light-field. The coherent scattering by the absorption and stimulated emission of photons means the force is conservative. In Chapter 2, where the theory of dipole trapping is discussed in more detail, it will be shown that the sign of the detuning of the trapping laser's frequency from the atomic resonance frequency affects the type of trap formed. If the detuning is positive (blue-detuned) the atoms are attracted to regions of intensity minima, which has the advantage of minimising heating caused by scattering. If the detuning is negative (red-detuned) the atoms are attracted to regions of intensity maxima and unless the detuning is large, significant heating can occur.

The use of a dipole trap for atoms was first proposed in 1962 by Askar'yan [65] and the idea was developed further by Letokhov [66] and Ashkin [67, 68]. In 1978 Bjorkholm *et al.* focused an atomic beam co-propagating with a laser [69]. The first optical trap for atoms was demonstrated in 1986 by Chu *et al.* [70].

The dipole force can be used to perform atom optics (see ref. [15] for a review). For example, in 1992 Sleator *et al.* demonstrated focusing by reflecting a laser off a glass plate causing a standing wave to be set up, which resulted in an approximate parabolic potential at the anti-nodes of the wave [71]. An atom mirror can also be constructed from the evanescent wave of blue-detuned light subject to total internal reflection within a glass block [72, 73].

However, the dipole force is most often used in the context of guides to transport, or traps to store cold atoms. Laser guiding has been achieved both in free space [74, 75, 76, 77, 78], within Laguerre-Gaussian light beams [79] and also within optical fibers [80, 81, 82, 83]. Bose-Einstein condensates have also been transported from one chamber to another with an optical tweezer [84]. Further details of optical guiding experiments can be found in the reviews [85, 86].

The crudest example of a dipole trap is a tightly focused red-detuned laser beam which confines in all three spatial directions. An excellent review of the variations in dipole trap designs and operation can be found in ref. [87]. The problem of heating in red-detuned traps can be reduced by using far-off resonance optical traps [88]. At extreme detunings the traps can be viewed as Quasi-Electrostatic traps (QUESTs), where the atomic polarisability behaves as a static quantity. This trap for cold atoms was first demonstrated by Takekoshi *et al.* using a CO_2 laser and was shown to have negligible scattering [89, 90]. As the ground state dipole potential does not depend on the hyperfine states of atoms, different atomic species and states can be trapped simultaneously [91, 92]. One further advantage of using a CO_2 laser with its long wavelength ($\lambda_T = 10.6\ \mu m$) is that an optical lattice created from interfering multiple beams will have large lattice spacings. It is therefore possible to observe and manipulate individual sites [93, 94].

In the race to produce the first BEC, the optical trap was largely ignored in favour of magnetic traps. At that time the low collision rates resulting from a low initial phase-space density made optical traps unsuitable for evaporative cooling to quantum degeneracy [95]. Instead rf-evaporation out of magnetic traps was used [96]. Subsequent research groups followed the magnetic trap route, and it is only in recent years that optical traps have become popular again in the BEC community. In 2001 Barrett *et al.* produced the first all-optical BEC by evaporating ^{87}Rb atoms using a crossed CO_2 dipole trap [97]. Scaling

laws for evaporation out of dipole traps were studied by O'Hara [98]. The very first ^{133}Cs BEC was obtained using dipole trap evaporation [99]. Recently a compressible crossed dipole trap was used to produce a ^{87}Rb BEC [100, 101] and an optical surface trap was used to create a ^{133}Cs BEC [102]

In general the optical dipole force is much weaker than the magnetic force discussed earlier, with typical trap depths on the order of 1 mK and 100 mK respectively. However there are a number of advantages, both fundamental and practical, of using optical rather than magnetic forces to manipulate and trap neutral atoms. The variety of atomic states and species available for trapping is much larger. For example, atoms can be trapped in their lowest internal state thus avoiding two body loss mechanisms and elements without a ground state magnetic moment can be trapped (eg. Ytterbium [103]). Furthermore, multiple spin states can be trapped simultaneously, an example of this is the spinor BEC experiment of Barrett *et al.* [97]. If no magnetic fields are present then Feshbach resonances can be used to tune the scattering length [104]. On a practical front, high magnetic field gradients require coils in close proximity to the vacuum chamber, thus reducing optical access for cooling beams. The high currents flowing in the coils may also require water cooling. Optical traps do suffer from disadvantages including: small capture volume; inefficient loading; the extra complication of another laser system; extra dangers from intense and far-infrared laser light.

Optical lattices

Periodic arrays of traps, called optical lattices, can be created by interfering multiple light fields [105, 106]. These crystals built from light have applications in simulating condensed matter systems and in quantum computing. In recent years, interest in optical lattices has been heightened by populating the lattices with BECs or degenerate Fermi gases. An exciting development is the reversible Mott insulator transition performed by Bloch *et al.* [107]. A BEC is placed into a 3D optical lattice with low enough trap depth to allow quantum tunneling between sites, thus allowing the phase coherence to be retained. By ramping up the laser intensity, the tunneling freezes out slowly enough to allow each site to be populated with exactly the same number of atoms per site. A number coher-

ence has been created at the expense of destroying the phase coherence, as the atoms can no longer communicate through the potential barrier. The potential can now be lowered, resulting in the destruction of the number coherence but the rebirth of the phase coherence.

One extension to the experiment was to perform coherent spin-dependent transport of atoms [108]. In this case, an optical lattice was created that had a spin dependence; atoms in the lower hyperfine ground state experienced one potential, and atoms in the upper hyperfine ground state experienced another potential. By changing the polarisation of the lasers, it was possible to move the two potentials in opposite directions. By placing atoms in a quantum superposition of the ground and excited states, and then shifting the lattice sites, it was possible to coherently transport atoms.

Another recent experiment by Phillips *et al.* demonstrated patterned loading of BECs in optical lattices [109]. The experiment started with a BEC placed into an optical lattice. Then a second lattice, with lattice spacing an integer m times smaller than the original, is switch on. In the final stage the original lattice is switched off, leaving the second lattice populated at every m^{th} site.

1.2 Research aims and outline

The research presented in this thesis concentrates on the manipulation of cold atoms using magnetic and optical fields. There are two parallel topics of research. The motivation, aims and scope of each area are outlined below.

1.2.1 Atom guiding and focusing

Many cold atom experiments employ a double-chamber vacuum setup that is differentially pumped. The first collection chamber generally employs a relatively high pressure ($\sim 10^{-9}$ Torr) magneto-optical trap (MOT) to collect a large number of cold atoms. These atoms are then transported to a lower pressure 'science' chamber to allow for longer trap lifetimes. The act of moving the atoms between the two regions results in an undesired density decrease unless steps are taken to counteract the atomic cloud's ballistic expansion. One ap-

proach is to catch the atoms transported into the science chamber in a second MOT. However, an undesirable feature is the restriction placed on subsequent experiments by the laser beams and magnetic-field coils required to realise the second MOT. An alternative approach is to focus or guide the atoms such that they can be collected in a conservative trap. This would be ideal for remotely loading tight traps with relatively small depth, e.g. optical dipole traps [87], atom chips [31, 110, 111], miniature magnetic guides [112, 113, 114], and storage rings [115, 116]. Furthermore, a very similar procedure could be used in atom lithography [117] and a cold low-density atomic source for fountain clocks [11].

In comparison to an unfocused cloud, the density of the cloud can be increased by many orders of magnitude after magnetic focusing. To date, the studies of pulsed magnetic focusing have been analysed under the assumption that the magnetic lens potential is harmonic - this work addresses the validity of this approximation, and the effects of aberrations. Lens designs for 1D and 3D are presented that minimise aberrations due to the lens potential's departure from the perfect harmonic case. The timing calculations required to bring an atomic cloud to focus after either a single- or double-impulse are explained and the lens system is modelled in terms of $\mathcal{ABCD}$ matrices.

In addition, research presented in this thesis investigates a far-off resonance laser guide to radially confine a vertically launched atomic cloud. The optimisation of the guide parameters was studied, and an analysis of loss mechanisms are presented. However, the atoms remain largely unperturbed in the axial direction. The hybrid technique of combining radial confinement, via far-off resonance guiding, with an axially focusing magnetic lens is investigated.

1.2.2 Enhanced loading of optical lattices

When atoms are trapped within a 3D quasi-electrostatic optical lattice the long trap lifetimes, periodic structure, high trap frequencies and large lattice spacings make the system ideal to implement quantum information. The system satisfies the "DiVincenzo" criteria for creating a suitable quantum computer [118, 119].

One obstacle to overcome is the problem of a differential light-shift. For a CO_2 dipole trap the excited state has a $\sim$ 2.6 times larger shift than the ground state. This has the undesired effect of turning the laser cooling mechanism into

a heating mechanism in regions of high intensity. Thus loading is inhibited. Recently colleagues at Durham University have shown it is possible to engineer the light-shift by adding a second laser frequency [120]. The introduction of a Nd:YAG laser was shown to enhance the loading into a 1-Dimensional CO_2 lattice.

The second half of this thesis describes the design and construction of a 'second generation' experiment. The aim is to produce a face-centred cubic CO_2 lattice and load Rb atoms into it. Once complete the goal is to test a proposal that light-shift engineering can be performed with a diode laser operating close to the laser cooling frequency transition. Furthermore, it is planned to implement qubit rotations on lattice sites [121, 122] and ultimately produce entanglement between sites.

1.3 Thesis structure

Chronology and the immediate application of new material have been sacrificed to present the work in a methodical order: background → theory → experimental method → results and discussion → conclusions. The structure of the thesis is depicted in Figure 1.1. The research has two parallel areas of research (magnetic and optical potentials) and this is manifest in the thesis structure. Diversions from this structure, long proofs and supplementary information have been placed in the appendices. Special mention should be made of: common abbreviations (Appendix A); symbols and their meanings (Appendix B); values of fundamental constants (Appendix C); atomic structure of Rubidium (Appendix D). At the end of each chapter a summary of the key results is presented.

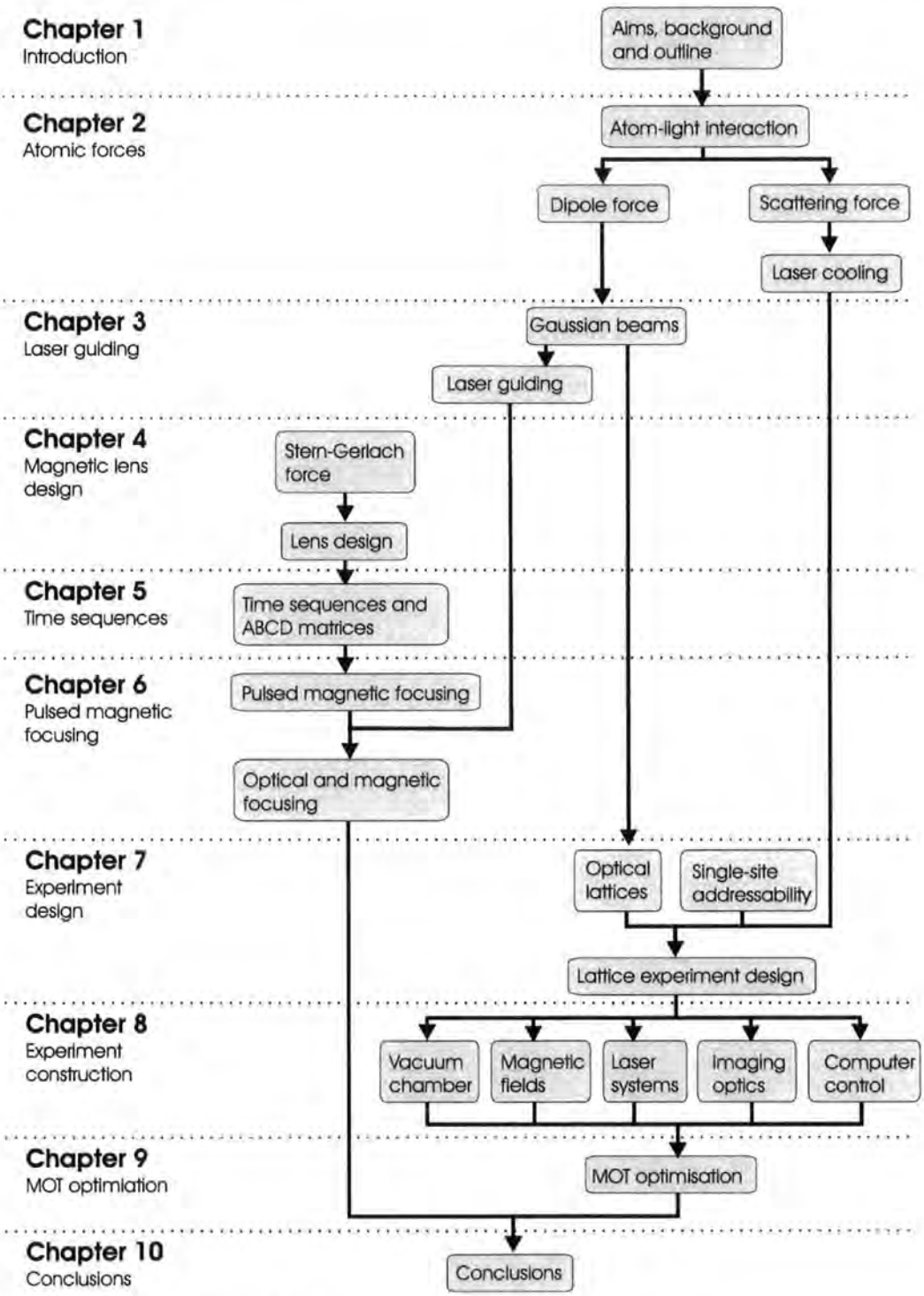

Figure 1.1: A schematic diagram of the thesis structure.

1.4 Publications

The work in this thesis has been partially covered in the following publications:

- *Single-impulse magnetic focusing of launched cold atoms*,
  M. J. Pritchard, A. S. Arnold, D. A. Smith and I. G. Hughes,
  J. Phys. B: At. Mol. Phys. **37**, pp. 4435-4450 (2004).

- *Double-impulse magnetic focusing of launched cold atoms*,
  A. S. Arnold, M. J. Pritchard, D. A. Smith and I. G. Hughes,
  New J. Phys. **8** 53 (2006).

- *Cool things to do with lasers*,
  I. G. Hughes and M. J. Pritchard,
  Accepted for publication in *Physics Education.*

- *Transport of launched cold atoms with a laser guide and pulsed magnetic fields*,
  M. J. Pritchard, A. S. Arnold, S. L. Cornish, D. W. Hallwood, C. V. S. Pleasant and I. G. Hughes,
  In preparation.

- *Experimental single-impulse magnetic focusing of launched cold atoms*,
  D. A. Smith, A. S. Arnold, M. J. Pritchard, and I. G. Hughes,
  In preparation.

Chapter 1 summary

- The research history of magnetic and optical manipulations of cold atoms has been briefly presented.
- The thesis aims have been stated.
- The thesis structure has been explained.
- Publications produced during the Ph.D have been listed.

Chapter 2

Background theory: Atoms and light

"The most beautiful thing we can experience is the mysterious. It is the source of all true art and science." Albert Einstein

2.1 Optical forces

In order to understand the origin of light-induced atomic forces and their applications in laser cooling and trapping it is instructive to consider an atom oscillating in an electric field. When an atom is subjected to a laser field, the electric field, $\mathbf{E}$, induces a dipole moment, $\mathbf{p}$, in the atom as the protons and surrounding electrons are pulled in opposite directions. The dipole moment is proportional to the applied field, $|\mathbf{p}| = \alpha|\mathbf{E}|$, where the complex polarisability, α, is a function of the laser light's angular frequency ω_{L}.

The interaction potential, equivalent to the AC-stark shift, is defined as:

$$U_{\mathrm{Dip}} = -\frac{1}{2}\langle \mathbf{p}.\mathbf{E} \rangle = -\frac{1}{2\epsilon_0 c}\mathrm{Re}(\alpha) I(\mathbf{r}), \tag{2.1}$$

where the angular brackets indicate a time average, $I(\mathbf{r}) = \epsilon_0 c|\mathbf{E}|^2/2$ is the laser intensity, and the real part of the polarisability describes the in-phase component of the dipole oscillation. The factor of a half in front of eqn. (2.1)

is due to the dipole being induced rather than permanent. A second factor of a half occurs when the time average is made.

Absorption results from the out-of-phase component of the oscillation (imaginary part of α). For a two-level atomic system, cycles of absorption followed by spontaneous emission occur. Due to the fact that the above process depends explicitly on spontaneous emission, the absorption saturates for large laser intensities. There is no intensity limit on the dipole potential however. The scattering rate is defined as the power absorbed by the oscillator (from the driving field) divided by the energy of a photon $\hbar\omega_L$:

$$\Gamma_{sc}(\mathbf{r}) = \frac{\langle \dot{\mathbf{p}}.\mathbf{E} \rangle}{\hbar\omega_L} = \frac{1}{\hbar\epsilon_0 c}\mathrm{Im}(\alpha)I(\mathbf{r}). \tag{2.2}$$

2.1.1 Two-level model

For a two-level atomic system, away from resonance and with negligible excited state saturation, the dipole potential and scattering rate can be derived semiclassically. To perform such a calculation the polarisability is obtained by using Lorentz's model of an electron bound to an atom with an oscillation frequency equal to the optical transition angular frequency ω_0. Damping is also introduced; classically this occurs due to the dipole radiation of the oscillating electron, however a more accurate model uses the spontaneous decay rate, Γ, of the excited state. If the ground state is stable, the excited state has a natural line width equal to Γ. The natural line width has a Lorentzian profile as the Fourier transform of an exponential decay is a Lorentzian. The two-level model expressions calculated by Grimm *et al.* (eqns. (10) and (11) in ref. [87]) are quoted here:

$$U_{\mathrm{Dip}}(\mathbf{r}) = -\frac{3\pi c^2\Gamma}{2{\omega_0}^3}\left(\frac{1}{\omega_0 - \omega_L} + \frac{1}{\omega_0 + \omega_L}\right) I(\mathbf{r}), \tag{2.3}$$

$$\Gamma_{sc}(\mathbf{r}) = \frac{3\pi c^2\Gamma^2}{2\hbar{\omega_0}^3}\left(\frac{\omega_L}{\omega_0}\right)^3\left(\frac{1}{\omega_0 - \omega_L} + \frac{1}{\omega_0 + \omega_L}\right)^2 I(\mathbf{r}). \tag{2.4}$$

The model does not take into account the excited state saturation and the multilevel structure of the atom. However, the above results are useful to understand

the scalings and the effect of the sign of laser detuning, which is defined as:

$$\Delta = \omega_{\mathrm{L}} - \omega_0. \tag{2.5}$$

Figure 2.1 shows pictorially the relationship between the frequencies and detuning. If the laser has a frequency less than the transition frequency ($\Delta < 0$) one calls this a *red-detuned* laser and the opposite case is called a *blue-detuned* laser.

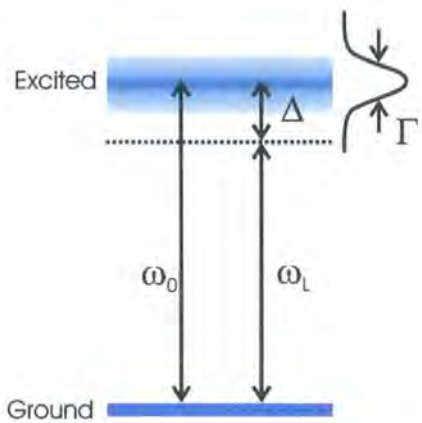

Figure 2.1: The two-level model showing the atomic transition angular frequency ω_0, the laser light's angular frequency ω_{L}, the detuning Δ and the natural line width of the excited state Γ.

For small detunings ($\Delta \ll \omega_0$ and $\omega_{\mathrm{L}}/\omega_0 \approx 1$), the *rotating wave approximation* (RWA) can be made and the $1/(\omega_0 + \omega_{\mathrm{L}})$ terms in eqns. (2.3) and (2.4) are ignored. This assumes that the term oscillates twice as fast as the driving frequency, and therefore time averages to zero. Under such an assumption the scalings of the dipole potential and scattering rate are:

$$U_{\mathrm{Dip}} \propto \frac{I(\mathbf{r})}{\Delta}, \quad \text{and} \quad \Gamma_{\mathrm{sc}} \propto \frac{I(\mathbf{r})}{\Delta^2}. \tag{2.6}$$

The consequence of such scalings will be explored further in Section 2.3. When the laser frequency is much lower than the atomic transition frequency, the static polarisability limit is reached. Such a limit is often referred to as the *quasi-electrostatic* (QUEST) regime. For alkali metal atoms this can be approximated by setting $\omega_{\mathrm{L}} \to 0$ in eqns. (2.3) and (2.4):

$$U_{\mathrm{Dip}}(\mathbf{r}) = -\frac{3\pi c^2}{{\omega_0}^3}\frac{\Gamma}{\omega_0} I(\mathbf{r}), \tag{2.7}$$

$$\Gamma_{sc}(\mathbf{r}) = \frac{3\pi c^2 \Gamma^2}{\hbar {\omega_0}^3} \left(\frac{\omega_L}{\omega_0}\right)^3 \left(\frac{\Gamma}{\omega_0}\right)^2 I(\mathbf{r}). \tag{2.8}$$

2.2 Laser cooling and the scattering force

In *Doppler cooling*, the scattering force is utilised in a way that makes it velocity dependent, resulting in a friction-like force which can be harnessed to cool atoms. The physical processes involved in laser cooling are described in detail in numerous sources, see for example refs. [2, 123] for a comprehensive description. A simplified account designed for teaching laser cooling to Physics A-level[1] students can be found in ref. [124]. A very brief sketch of the technique is presented below, before describing how it is applied to the specific case of cooling ^{85}Rb atoms.

The technique originates from the recoil kick an atom experiences when it absorbs a photon from a laser beam. The excited atom later decays via spontaneous emission and receives a second momentum kick. As the photon's spontaneous emission can occur in any direction, over many absorption-spontaneous emission cycles the second momentum kick averages to zero. Thus on average, for each cycle the atom receives a momentum kick of $\hbar\mathbf{k}$, where $\mathbf{k}$ is the laser wavevector, see Figure 2.2. The scattering rate is maximised on resonance ($\Delta = 0$), however the natural line width of the excited state means scattering can still occur off-resonance.

In order to take into account the saturation of the excited state population and to work close to resonance, the *Optical Bloch equations* are used (see, for example, ref. [123] or [125]). The scattering rate is given by:

$$\Gamma_{sc}(\mathbf{r}) = \frac{\Gamma}{2} \frac{I(\mathbf{r})/I_{sat}}{1 + I(\mathbf{r})/I_{sat} + 4(\Delta)^2/\Gamma^2}. \tag{2.9}$$

The saturation intensity is given by:

$$I_{sat} = \frac{2\pi^2 \hbar \Gamma c}{3{\lambda_C}^3}. \tag{2.10}$$

[1] A *Further education* course in England and Wales taken by students 16–18 years old.

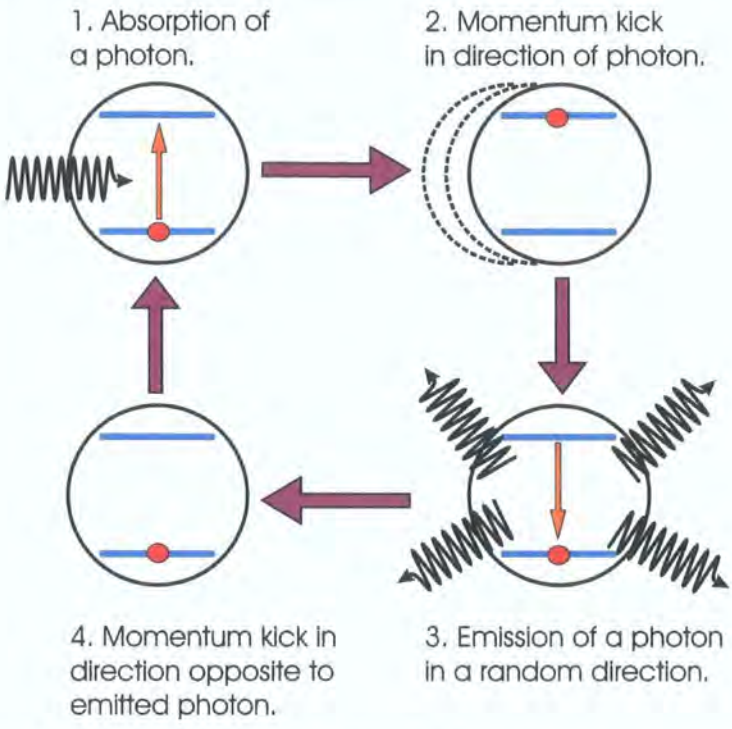

Figure 2.2: A simplified picture showing the absorption-spontaneous emission cycle that results in giving an atom a momentum kick.

For a Rb atom on the D2 line ($\lambda_C = 780$ nm, subscript C used to denote the cooling transition), and with a natural line width of $2\pi \times 5.9$ MHz [126], the saturation intensity is $I_{sat} = 1.6$ mW/cm^2.

A moving atom with velocity $\mathbf{v}$ will see the laser frequency Doppler shifted. This can easily be incorporated in eqn. (2.9) by making the replacement: $\Delta \rightarrow \Delta + \mathbf{k}.\mathbf{v}$. The scattering force is obtained by multiplying the scattering rate by the photon momentum $\hbar\mathbf{k}$. In the 1D case of two counter-propagating laser beams the scattering force is the resultant of the two beams, $F_{tot} = F_+ + F_-$, where the individual beam forces are:

$$F_\pm = \pm\frac{\hbar k\Gamma}{2}\frac{I/I_{sat}}{1 + 2I/I_{sat} + 4(\Delta \mp kv)^2/\Gamma^2}, \tag{2.11}$$

The extra factor of two in the denominator accounts for the contribution of the two beams towards the saturation of an atom. The forces of the individual beams, F_+ and F_-, and the total force, F_{tot}, are plotted in Figure 2.3. In the

regime $|kv/\Gamma| < 1$ the force can be approximated by:

$$F_{\text{tot}} \simeq \frac{8\hbar k^2 \Delta}{\Gamma} \frac{I/I_{\text{sat}}}{(1 + 2I/I_{\text{sat}} + 4(\Delta/\Gamma)^2)^2} v = \beta v. \tag{2.12}$$

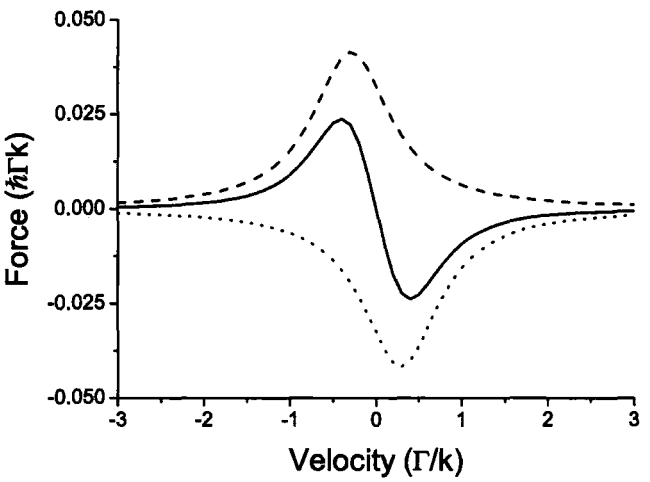

Figure 2.3: The combined force of two counter propagating red-detuned laser beams is plotted against velocity. The dashed line is F_+, the dotted line is F_-, and the solid line is the total force F_{tot}. The parameters used to produce the plot were $I/I_{\text{sat}} = 0.1$ and $\Delta/\Gamma = -1/\sqrt{12}$.

For red-detuned laser beams ($\Delta < 0$), β is negative and the force is friction-like, therefore resulting in cooling as the atom's kinetic energy is dissipated. It can be shown by taking the derivative of eqn. (2.12) that the maximum friction for weak beams is achieved when $\Delta/\Gamma = -1/\sqrt{12}$. The extension from 1D to 3D involves the use of 3 pairs of counter-propagating laser beams. This is called *optical molasses* due to the 'sticky' environment that the atom now moves in. The minimum temperature that can be achieved by Doppler cooling is given by balancing the cooling rate ($-\beta v^2$) with the heating rate due to the random nature of spontaneous emission ($(\hbar k)^2 \Gamma_{\text{sc}}/m$). This temperature is called the Doppler limit [123]:

$$\mathcal{T}_{\text{D}} = \frac{\hbar\Gamma}{2k_{\text{B}}}. \tag{2.13}$$

Which for alkali metals is typically a few hundred μK. Sub-Doppler cooling mechanisms exist that overcome the Doppler cooling limit and can create an atomic gas with low μK temperatures. The origin of such mechanisms is the

spatial variation in the AC-stark shift due to polarisation gradients, see ref. [127] for more details.

2.2.1 The Magneto-optical trap

Whilst Doppler cooling can reduce the temperature of an atomic gas, it does not spatially confine the gas. Even at very low temperatures the atoms will escape from the cooling region due to Brownian motion random-walks. Raab *et al.* in 1987 invented a solution that combines optical and magnetic fields to both cool and trap the atomic gas [64]. Their solution involved applying a magnetic field linear with position to lift the degeneracy of the m_F states. In addition they used counter-propagating laser beams with opposite circular polarisations to produce $\sigma^{\pm}$ transitions. This results in an atom moving away from resonance being *Zeeman shifted* into resonance with a beam that pushes it back to the centre, see Figure 2.4 (a). The simplest combination of circularly polarised light and anti-Helmholtz coils to produce a quadrupole magnetic field is shown in Figure 2.4 (b). The design can be adapted to suit specific applications, see for example the pyramid MOT in Chapter 8.

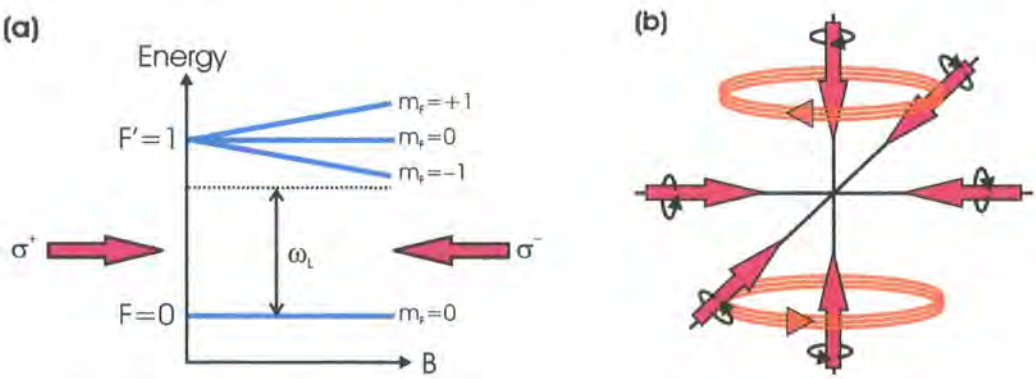

Figure 2.4: Plot (a): The principle of a magneto-optical trap is demonstrated for the $F = 0 \rightarrow F' = 1$ transition. An atom that has moved away from the trap centre is more likely to absorb a photon from the beam pushing it back. This results in a harmonic force. Plot (b): The simplest design for a 3D magneto-optical trap made from six circularly polarised laser beams. The anti-Helmholtz coils created a quadrupole magnetic field.

2.2.2 Implementing laser cooling in ^{85}Rb

In the above description it has been assumed that we are dealing with a two-level atom (with magnetic sub-levels). In reality atoms have a multi-level structure. It is possible though to find so called *closed transitions* that exploit the electric dipole selection rules to produce an approximation to a two-level system. For the case of ^{85}Rb, a closed transition occurs on the D2 line from $5^2S_{1/2}\,, F = 3$ state to the $5^2P_{3/2}\,, F' = 4$ state; where F is the total angular momentum of the atom and the prime indicates the excited state. This is illustrated in Figure 2.5.

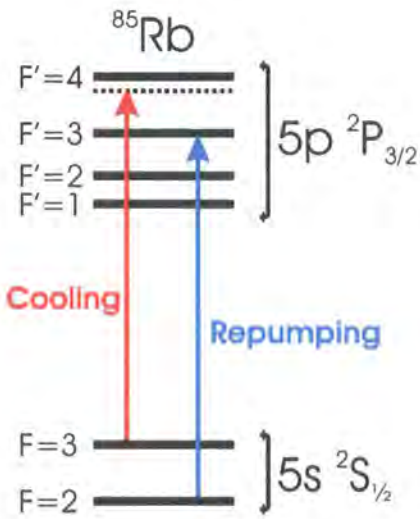

Figure 2.5: The energy level diagram for ^{85}Rb. The transition frequencies for the cooling and repumping lasers are also shown. This figure should be contrasted with the simpler two-level model in Figure 2.1. The level spacings are given in Appendix D.

Due to the selection rule $\Delta F = -1, 0, +1$ (see for example ref. [128]), the only decay route from the excited state is back to the original ground state, thus a closed cycle ensues. For cooling to occur, the laser frequency has to be red-detuned by a few line widths. Unfortunately there is a small probability that the transition from $5^2S_{1/2}\,, F = 3$ state to the $5^2P_{3/2}\,, F' = 3$ state will occur, as the laser is far blue-detuned from this frequency. Being in this excited state means that there is a probability that the atom will decay down to $5^2S_{1/2}, F = 2$ state, and thus be lost from the cycle. Therefore a second laser frequency is required to *repump* the lost atoms back into the cooling cycle. This laser operates on the $5^2S_{1/2}\,, F = 2$ state to the $5^2P_{3/2}\,, F' = 3$ state transition.

When laser cooling from a vapour, one typically uses a detuning of around -2Γ ($-2\pi \times 12$ MHz for Rb). The laser operates at a wavelength of $\lambda_C = 780$ nm which corresponds to a frequency of $\sim 10^{15}$ Hz. Care must be taken to know and accurately stabilise the laser frequency. This is discussed further in Chapter 8.

2.3 Laser trapping and the dipole force

The previous section outlined how the scattering force can be used to cool atoms with laser fields, we now turn to trapping them with light. The spatial variation of the intensity term in the dipole potential, eqn. (2.1), results in the conservative dipole force:

$$\mathbf{F}_{\text{Dip}} = -\nabla U_{\text{Dip}} = \frac{1}{2\epsilon_0 c}\text{Re}(\alpha)\nabla I(\mathbf{r}). \tag{2.14}$$

As can be seen from eqn. (2.6), a blue-detuned laser ($\Delta > 0$) will produce a positive AC-stark shift. Therefore the dipole force will cause atoms to be attracted to regions of low intensity. An atom will be attracted to red-detuned regions of high intensity. The scalings in eqn. (2.6) illustrate that a far red-detuned dipole trap with negligible scattering and sufficient trap depth requires a high intensity. For a CO_2 laser ($\lambda_T = 10.6$ μm, subscript T used to indicate the trapping laser's wavelength) this regime is readily achieved, as it is possible to buy bench-top lasers with powers of $\sim$ 100 W. Such a laser operates in the quasi-electrostatic regime, and eqn. (2.7) is an approximation of the dipole potential.

With knowledge of the polarisability and laser beam intensity profile, the force can be characterised via eqn. (2.14). In Chapter 3 laser beam profiles will be explained. The remainder of this chapter discusses the calculation of the polarisability in a more robust manner than the two-level approximation.

2.3.1 Polarisability

The real part of the polarisability has two parts: a scalar term, α_0, that corresponds to a dipole being induced parallel to the direction of the electric field and a tensor term, α_2, that corresponds to an induced dipole perpendicular to

the electric field. The scalar term shifts all hyperfine and magnetic sublevels equally. The tensor term mixes the hyperfine and magnetic sublevels through an operator Q, and therefore the degeneracy of the m_F states is lifted. The exception to this is for the ground state in alkali atoms ($J = 1/2$), where the lack of orbital angular momentum stops the spin-orbit coupling producing a perpendicular induced dipole moment and hence $\alpha_2 = 0$.

The light-shift is given by the eigenvalues of the matrix [129, 130]:

$$E = E_{\text{hfs}} - \frac{1}{2\epsilon_0 c}(\alpha_0 \mathbb{I} + \alpha_2 Q) I(\mathbf{r}), \tag{2.15}$$

where $\mathbb{I}$ is the identity matrix. The non–zero and diagonal matrix elements of the hyperfine interaction can be written in the $|F\, m_F\rangle$ basis as [131]:

$$\langle F\, m_F | E_{\text{hfs}} | F\, m_F \rangle = -\frac{\hbar}{2} A_{\text{hfs}} K + \hbar B_{\text{hfs}} \frac{\frac{3}{2}K(K+1) - 2I_{\text{n}}(I_{\text{n}}+1)J(J+1)}{2I_{\text{n}}(2I_{\text{n}}-1)\,2J(2J-1)}\,, \tag{2.16}$$

where I_{n} is the nuclear spin quantum number, J is the total electronic angular momentum quantum number and K is defined as:

$$K = F(F+1) - I_{\text{n}}(I_{\text{n}}+1) - J(J+1)\,. \tag{2.17}$$

For the $5P_{3/2}$ states of ^{85}Rb, the hyperfine structure constants are $A_{\text{hfs}} = 2\pi \times 25.009$ MHz and $B_{\text{hfs}} = 2\pi \times 25.88$ MHz [132].

The matrix Q has components $\langle F m_{\text{F}} | Q_\mu | F' m'_{\text{F}} \rangle$ where:

$$Q_\mu = \frac{3\hat{J}_\mu^2 - J(J+1)}{J(2J-1)}. \tag{2.18}$$

The operator $\hat{J}_\mu$ is the electronic angular momentum operator in the direction of the laser field. When the electric field is aligned along the quantisation axis,

the non-zero elements in the Q-matrix in the $|F\, m_F\rangle$ basis are given by [133]:

$$\begin{aligned}\langle F\, m_F|Q|F'\, m_F\rangle = &\left[\frac{(J+1)(2J+1)(2J+3)}{J(2J-1)}\right]^{1/2} \\ &\times(-1)^{I_n+J+F-F'-m_F}\sqrt{2(F+1)(2F'+1)} \\ &\times\begin{pmatrix} F & 2 & F' \\ m_F & 0 & -m_F \end{pmatrix}\begin{Bmatrix} F & 2 & F' \\ J & I & J \end{Bmatrix}.\end{aligned} \tag{2.19}$$

The object contained within the semi-circular brackets is a (3-j) symbol and the curly brackets contained a (6-j) symbol, see ref. [134]. It is interesting to note that the $|m_F|$ states are degenerate, a consequence of using a linearly polarised field. The general form of the Q-matrix for ^{85}Rb ($I_n = 5/2$) is shown in Figure 2.6. When $m_F = \pm F_{max}$ the problem is simplified as the two 1×1 matrices contain the value 1, thus $\alpha_{max} = \alpha_0 + \alpha_2$.

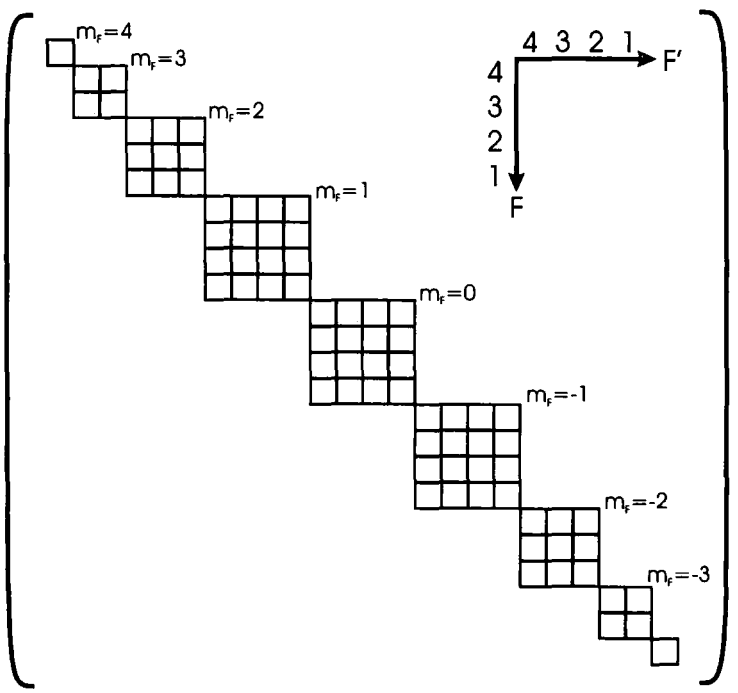

Figure 2.6: The general form of the Q-matrix for an atomic state $J = 3/2$, $I_n = 5/2$. The non-zero matrix elements occur along the diagonal of the matrix.

The ground state shift

In most instances, knowledge of the ground state shift is sufficient to understand dipole trap dynamics. There is a vast simplification for the ground state shift; as already mentioned, the tensor polarisability is zero. Therefore, with knowledge of α_0, the dipole force is known through eqn. (2.14). Various groups have theoretically calculated and experimentally measured polarisabilities in Rb, see for example refs. [120, 135, 136, 137, 138, 139, 140]. Since for this thesis the light shifts of ^{85}Rb at only two wavelengths are needed (Nd:YAG $\lambda_T = 1.064$ μm and CO_2 $\lambda_T = 10.60$ μm), the relevant polarisabilities are quoted in Table 2.1 for two recent calculations. Griffin *et al.*'s calculations are non-relativistic and slightly overestimate the values Safronova *et al.* obtain in their relativistic calculations.

Polarisability	λ_T (μm)	Griffin *et al.* [120]	Safronova *et al.* [137, 140]
$\alpha_0[5s]$	1.064	722	693.5(9)
$\alpha_0[5p]$	1.064	-1162	–
$\alpha_2[5p]$	1.064	566	–
$\alpha_0[5s]$	10.60	335	318.6(6)
$\alpha_0[5p]$	10.60	872	–
$\alpha_2[5p]$	10.60	-155	–

Table 2.1: The scalar and tensor polarisabilities for Rb atoms. The two wavelengths quoted correspond to that of a Nd:YAG and CO_2 laser. To convert the values into SI units they must be multiplied by $4\pi\epsilon_0 {a_0}^3$, where a_0 is the Bohr radius (0.529 Å).

The differences between ground state polarisabilities for the two-level model from Section 2.1.1 and the more accurate multi-level calculations of Safronova *et al.* [137, 140] are tabulated in Table 2.2. For far-detuned lasers, the rotating wave approximation significantly underestimates the polarisability. The static limit for the CO_2 wavelength is within 1% of the two-level value. However, all values based upon the two-level model have a $\sim$ 7% underestimate of the polarisability calculated by including multi-level structure. Therefore, the values of Safronova *et al.* will be used throughout this thesis for calculating dipole traps.

State	λ_T (μm)	2-level model	RWA	Static limit	Polarisability [137, 140]
$\alpha_0[5s]$	1.064	642.5	556.8	–	693.5
$\alpha_0[5s]$	10.60	298.9	160.4	297.2	318.6

Table 2.2: A comparison of the ground state polarisability calculated using: the two level model (eqn. (2.3)); the rotating wave approximation applied to eqn. (2.3); the static limit (eqn. (2.7)); Safronova *et al.* calculated polarisability [137, 140]. To convert the values into SI units they must be multiplied by $4\pi\epsilon_0 a_0{}^3$, where a_0 is the Bohr radius (0.529 Å).

The excited state and differential-shifts

As can be seen in Table 2.1, the ground and excited states have different polarisabilities, resulting in a *differential light-shift*. This has consequences if in addition to a laser trapping the atoms, there is also a separate Doppler cooling laser present. A common occurrence in far-detuned dipole trap experiments is to have the trap laser switched on throughout the cooling and MOT loading process, then, when the cooling beams are switched off, a fraction of the atoms gets loaded into the trap. A differential light shift means that the cooling laser's detuning becomes dependent on the intensity of the trapping laser – generally an unwanted effect.

The sign of the polarisability of the excited state changes between the Nd:YAG and CO_2 laser wavelengths. The Nd:YAG laser light shifts the excited state upwards, whereas the CO_2 laser shifts the state downwards. The effect on detuning is illustrated in Figure 2.7. The Nd:YAG laser causes the red-detuned cooling laser to be further detuned. However, the CO_2 laser causes the detuning magnitude to decrease, and at some point the detuning will turn positive. For deep potential wells, this causes the focus region, where the intensity is greatest, to heat the atoms. This has been observed experimentally, see for example ref. [94]. Griffin *et al.* experimentally demonstrated that, using a combination of a Nd:YAG and CO_2 laser, the excited state shift can be engineered to be the same as the ground state shift, hence causing enhanced trap loading [120].

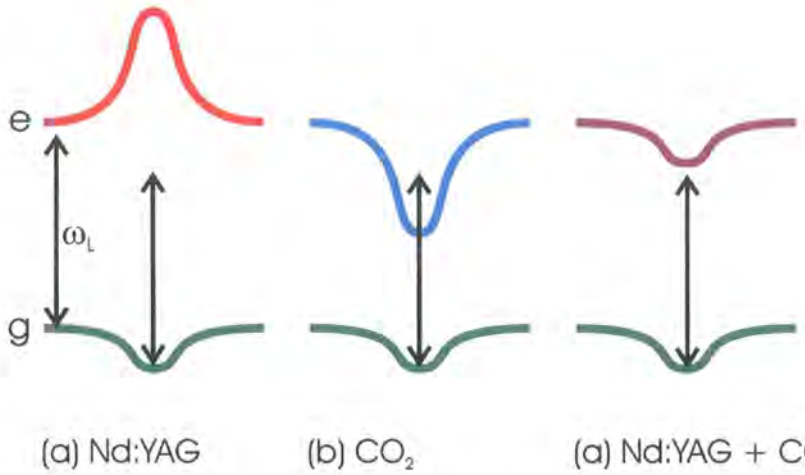

Figure 2.7: The differential light-shift for three combinations of trapping lasers are illustrated: (a) Nd:YAG laser only, the negative excited state polarisability shifts the level upwards causing the cooling laser to be further red-detuned; (b) CO_2 laser only, the positive excited state polarisability shifts the level downwards causing the cooling laser to be blue-detuned for sufficient trapping laser intensities; (c) Nd:YAG and CO_2 lasers, when the powers have been chosen correctly the differential light-shift is canceled [120].

Chapter 2 summary

- The physical origin of the scattering and dipole forces was described.
- A two-level atomic model was presented that led to intensity and detuning scalings.
- The technique of laser cooling was described along with how it is implemented in ^{85}Rb.
- The scalar and tensor polarisability contributions to the the dipole force were discussed. The approach was compared with the simpler two-level approach.
- The differential light-shift and the problem this causes with dipole trap loading was explained. The concept of light-shift engineering was introduced.

Chapter 3

Laser guiding

"Computers are useless. They can only give you answers." Pablo Picasso

This chapter will describe how a laser beam can be used to efficiently guide a cold atomic cloud. Work contained within this chapter led to the publication of ref. [141] and has been carried out in collaboration with the other authors.

3.1 Gaussian laser beam profile

For laser light, with power P, traveling along the z-axis, with a radially symmetric Gaussian transverse profile, the form of the intensity is:

$$I(r,z) = \frac{2P}{\pi w(z)^2} \exp\left(\frac{-2r^2}{w(z)^2}\right), \tag{3.1}$$

where $r = \sqrt{x^2+y^2}$. The $1/e^2$ intensity radius of the beam, $w(z)$, is the radial distance from the z-axis to the point where the intensity has decreased by a factor of e^2 ($= 7.389$), and is given by:

$$w(z) = w_0\sqrt{1+\left(\frac{z-z_0}{z_\mathrm{R}}\right)^2}. \tag{3.2}$$

Here w_0 is the beam waist[1], z_0 is the focal point, and z_R is the Rayleigh length, given by:

$$z_R = \frac{\pi w_0^2}{\lambda_T}. \tag{3.3}$$

The Rayleigh length is a measure of the length scale of the diffraction that is introduced via eqn. (3.2). It is the axial distance required for the laser beam's area to double in size. The quantities parameterising a Gaussian beam are shown in Figure 3.1.

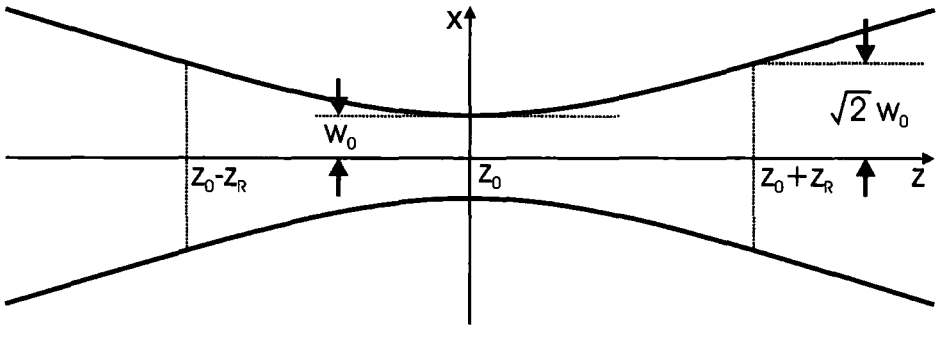

Figure 3.1: Diagram showing the important quantities that define a Gaussian laser beam. The thick black lines indicate the $1/e^2$ radius. The diagram is a cut through the $y = 0$ plane.

3.2 Laser guide modelling

In this chapter a specific experimental setup is modelled, however the analysis can be easily applied to other setups. Figure 3.2 (a) shows a diagram of the guiding experiment. A Magneto-optical trap (MOT), centred at $\{0, 0, 0\}$, collects cold ^{85}Rb atoms at a temperature of $\mathcal{T} = 20.0$ μK (with corresponding velocity standard deviation $\sigma_V = \sqrt{k_B \mathcal{T}/m} = 4.42$ cm s^{-1}) and with an isotropic Gaussian spatial distribution in each Cartesian direction, with standard deviation of $\sigma_R = 0.20$ mm. The atoms are launched vertically upwards as a fountain using the moving molasses technique [142]. The initial launch velocity is chosen so that the centre of mass parabolic trajectory will have an apex at a height of $h = 22.0$ cm above the MOT centre. This requires a

[1]The use of the term 'beam waist' to measure a radius is misleading. However, as the term is in common use, this terminology will be adopted.

launch velocity of $v_{z_i} = \sqrt{2gh} = 2.08$ m s^{-1}. The MOT to apex flight time is $T = \sqrt{2h/g} = 212$ ms. At 18.0 cm above the MOT there is a 0.5 mm radius aperture, to allow the atoms to pass into a lower pressure 'science' chamber (typically 2 orders of magnitude lower pressure). The time to reach the aperture is 121 ms for unperturbed motion.

A vertically oriented red-detuned laser provides radial guiding via the optical dipole force. The dipole trap depth is proportional to the laser power. Therefore a far-detuned guiding experiment (with negligible scattering) will always have more efficient loading by increasing the laser power. A Nd:YAG ($\lambda_T = 1,064$ nm) guide laser that has a maximum power of 19 W was chosen to be modelled. These parameters match a similar experiment conducted by Davies *et al.* [75]. The beam waist and focal point are chosen to optimise the guiding efficiency, and this optimisation process is contained in Section 3.3.

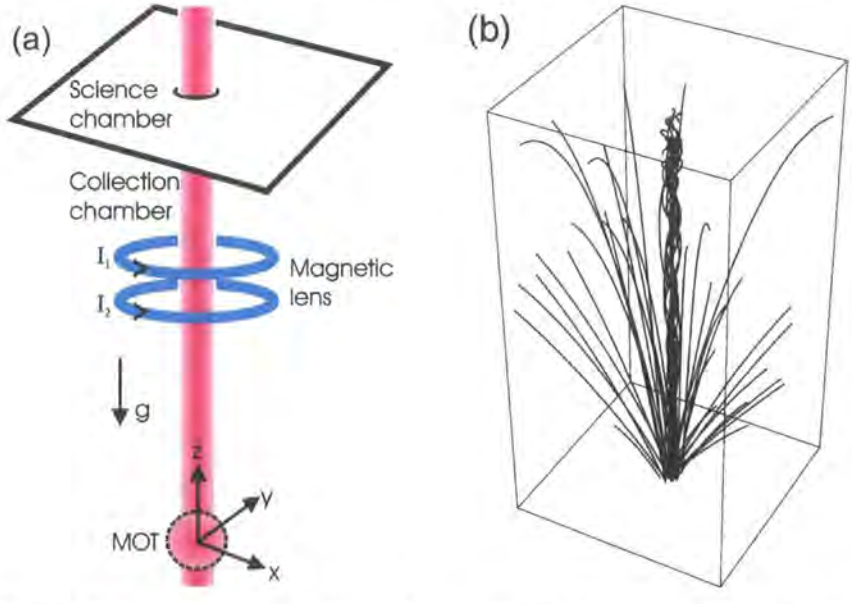

Figure 3.2: Diagram (a) shows the experimental setup with guiding laser beam, magnetic lens and aperture for differential pumping. Atoms are collected in a MOT and then launched vertically. In (b) a numerical simulation shows the trajectories of launched atoms. Roughly 30% of the atoms are guided within the laser beam, these constitute the central column of the simulation. The unguided atoms follow ballistic trajectories.

In Figure 3.3 (a) and (b) the Rayleigh length and the $1/e^2$ radius at the aperture height of 18.0 cm are plotted against beam waist for the simulated experiment. The minimum $1/e^2$ radius at the aperture occurs when the Rayleigh length

equals the aperture height. From eqn. (3.2) the minimum beam radius is $w(z) = \sqrt{2}w_0$.

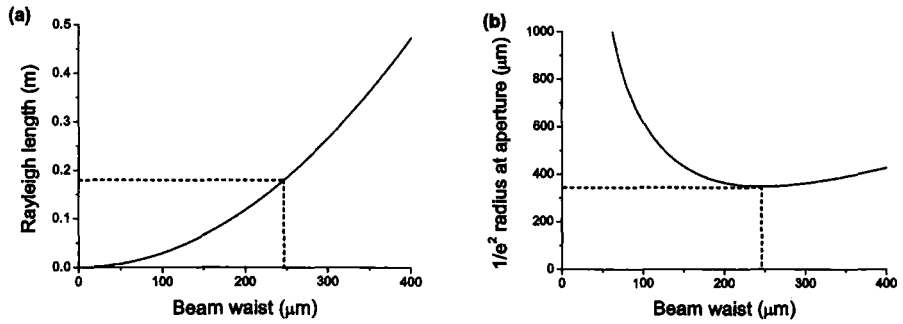

Figure 3.3: Plot (a) shows the Rayleigh length (eqn. (3.3)) plotted against beam waist w_0. In (b) the $1/e^2$ radius at the aperture height ($z = 18.0$ cm) is plotted against beam waist. The minimum of 349 μm occurs when $z_R = 18.0$ cm.

3.2.1 The dipole force

Combining the expressions for the dipole potential (eqn. (2.1)) and the laser intensity (eqn. (3.1)), gives the potential an atom in the ground state experiences:

$$U_{\mathrm{Dip}}(r,z) = -\frac{\alpha_0 P}{\epsilon_0 c\,\pi\, w(z)^2} \exp\left(\frac{-2r^2}{w(z)^2}\right), \tag{3.4}$$

Using $\alpha_0 = (4\pi\epsilon_0) \times 693.5\ a_0^3$ C m^2 V^{-1} for Rb in the presence of $\lambda_T = 1.064$ μm light [140], a 19 W laser with a beam waist of 250 μm (peak intensity of 1.94×10^8 W m^{-2}) produces a trap depth of $U_{\mathrm{Dip}}/k_B = 30.2$ μK. The force an atom experiences due to the laser guide is given by $\mathbf{F}_{\mathrm{Dip}} = -\nabla U_{\mathrm{Dip}}$. The radial and axial accelerations for a ^{85}Rb atom have been plotted in Figure 3.4. The radial acceleration is comparable with g and 3 orders of magnitude larger than the axial case. It is sufficiently large to provide an adequate guide for the cold atoms. On the contrary one wouldn't expect to see much evidence of perturbation from the ballistic motion in the axial direction. The length scales over which the radial and axial accelerations change are characterised by the beam waist and the Rayleigh length respectively. The radial angular frequency

for the laser guide is given by:

$$\omega_{r_L} = \sqrt{\frac{4\alpha_0 P}{m\,\epsilon_0 c\,\pi\,w(z)^4}}\,. \tag{3.5}$$

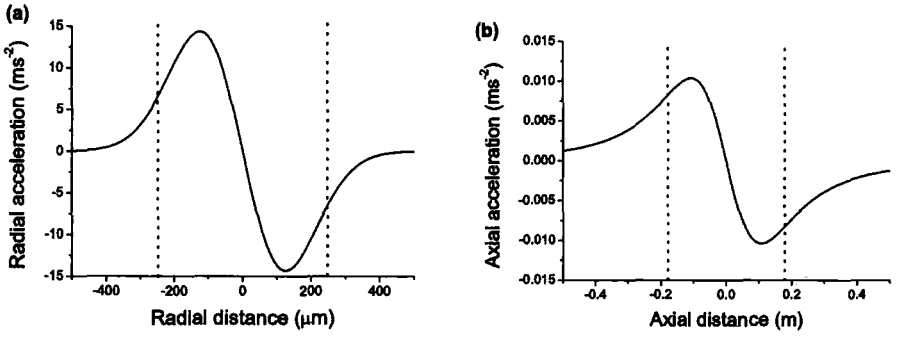

Figure 3.4: In plots (a) and (b) the radial and axial accelerations are plotted against distance from the beam centre. A 19 W laser with beam waist of 250 μm is used in the calculation. The radial acceleration is $\sim 10^3$ times larger than the axial case. The dashed vertical lines in (a) and (b) are $\pm w_0$ and $\pm z_R$ respectively.

3.2.2 Computer simulation

The expression for the force can be used in a numerical simulation of atomic trajectories within the laser guide. The computer program generates an atomic cloud made up of atoms that have random positions and velocities, the Gaussian distribution of which match the standard deviations given earlier. It is assumed that the only perturbations that the atoms experience are a downwards force due to gravity and the dipole potential. The effect of heating due to light scattering is negligible. A calculation for the above parameters, using eqn. (2.4), gives a scattering rate of ~ 0.1 photons per second. Collisions can be ignored as the average elastic collision rate within the MOT is 3 s^{-1}, see the calculation in Appendix E. The atoms are treated as point like particles, moving classically due to a force that is derived from quantum mechanics. The numerical solving of the differential equations was performed by *Mathematica*. A sample program to aid the understanding of the program has been included in Appendix F.

3.3 Loading the guide

Calculating the guiding efficiency can be broken down into two separate problems: loading atoms from the MOT into the guide, and subsequent transport losses. The fraction of atoms initially captured by the laser beam can be calculated analytically based on the work of Pruvost *et al.* [77] and extended by Wolschrijn *et al.* [143]. An atom will be radially bound if its total energy E is less than zero:

$$E = \frac{p^2}{2m} + U_{\mathrm{Dip}}(r,z) < 0, \tag{3.6}$$

where $p = \sqrt{{p_x}^2 + {p_y}^2}$ is the radial momentum and m is the atomic mass.

The initial atom distribution can be divided into two groups: energetically bound ($E < 0$) and unbound ($E > 0$). The normalised initial position and momentum distribution of the atomic cloud for a given temperature $\mathcal{T}$ is given by:

$$\Phi(r,p) = \frac{e^{-r^2/2{\sigma_R}^2}}{2\pi{\sigma_R}^2} \frac{e^{-p^2/2mk_B\mathcal{T}}}{2\pi m k_{\mathrm{B}}\mathcal{T}}. \tag{3.7}$$

The momentum standard deviation is given by: $\sigma_P = m\,\sigma_V = \sqrt{mk_{\mathrm{B}}\mathcal{T}}$. The loading efficiency, χ, is calculated by integrating $\Phi(r,p)$ and imposing the bound condition of eqn. (3.6) as the momentum integration limit:

$$\chi = \int_0^{\infty} \int_0^{\sqrt{2mU_{\mathrm{Dip}}(r,z)}} \Phi(r,p)\; 2\pi r \;\mathrm{d}r\; 2\pi p \;\mathrm{d}p. \tag{3.8}$$

By using the substitution $q = e^{-2r^2/w(z)^2}$ for the second integral, the solution is:

$$\chi = 1 - \frac{w(z)^2}{4{\sigma_R}^2} \left(\frac{\alpha_0 P}{\epsilon_0 c\,\pi\, w(z)^2 k_{\mathrm{B}}\mathcal{T}} \right)^{-\frac{w(z)^2}{4{\sigma_R}^2}} \Gamma\left(\frac{w(z)^2}{4{\sigma_R}^2}, 0, \frac{\alpha_0 P}{\epsilon_0 c\,\pi\, w(z)^2 k_{\mathrm{B}}\mathcal{T}} \right), \tag{3.9}$$

where $\Gamma(a,b,c) = \int_b^c q^{a-1}e^{-q}\,\mathrm{d}q$ is the generalised incomplete gamma function. The loading efficiency is plotted against beam waist and focal point in Figure 3.5 (a). The optimum $1/e^2$ radius for loading the modelled experiment is 252 μm, and this produces a load efficiency of 28.9%. The maximum exhibits a large plateau ($\chi > 25\%$ when the $1/e^2$ radius is between 175 μm and 360 μm) which results in great flexibility in choosing initial parameters. Due to this flexibility it was decided to study laser guiding when the beam focus coincides

with the MOT centre ($z_0 = 0$ cm). The reason for this is that an expanding beam will cool the cloud in the radial direction during the flight [77]; this is a consequence of Liouville's theorem [144]. For the rest of this thesis, all results presented will use a laser that is focused on the MOT centre, see Figure 3.5 (b). Alongside the analytical result, a Monte Carlo simulation of atomic trajectories was performed by solving the equations of motion that include gravity and the dipole force. The data points on the plot show the fraction of atoms from the MOT that are initially energetically bound and therefore satisfy eqn. (3.6).

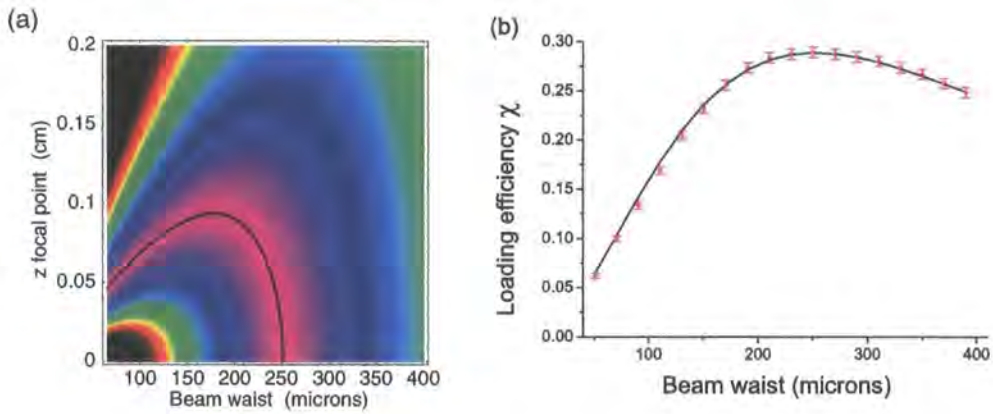

Figure 3.5: Plot (a): The analytical load efficiency, χ, is plotted against beam waist and z focal point. The black contour represents the optimum $1/e^2$ beam radius of 252 μm which corresponds to a load efficiency of 28.9%. Plot (b): The $z_0 = 0$ cross section of (a). The solid line is the analytical result and the data points are the result of a numerical simulation consisting of 10,000 atoms.

The loading efficiency can be increased by using a more powerful laser, a lower temperature atomic cloud or a smaller cloud size. The first two are intuitively obvious, however the reduction in cloud size is misleading because atom number is the important experimental quantity one wishes to maximise. For a MOT with constant atom density, the atom number increases proportional to the cube of the cloud radius. Although for large clouds a smaller cloud fraction is loaded, there is a greater number of atoms present and therefore the overall load increases with cloud radius.

3.4 Transport losses

Having considered the initial loading of the MOT into the laser beam, attention is now turned to the guiding properties and losses from the beam. Apart from heating and collisions (which are assumed to be negligible) there are two loss mechanisms: aperture truncation and diffraction.

3.4.1 Truncation losses

Without laser guiding, the transmission from a ballistically expanded cloud passing through a 0.5 mm radius aperture at a height of 18 cm is 0.4%. With guiding, this transmission can be increased by 75 times. This is shown in Figure 3.6 (a) where the transmission through the aperture is plotted against height above the MOT. The black line represents the transmission of an unguided atomic cloud. The aperture height of 18.0 cm was chosen to minimise ballistic transmission but still allow sufficient distance between the aperture and trajectory apex at 22 cm. The red and blue lines demonstrate laser guiding for 100 μm and 250 μm beam waists respectively. Again there is the initial decay due to the unguided atoms passing through the aperture. However, unlike the unguided case, a fraction of the atoms have been bound in the laser guide which significantly increases the aperture transmission. This corresponds to the tight core evident in Figure 3.2 (b). There is also atom loss from the guide due to diffraction. This is more obvious in the tightly focused 100 μm beam (red line), although all expanding laser beams will suffer losses. This diffraction loss is examined in Section 3.4.2.

In Figure 3.6 (b) there is a plot of transmission versus aperture radius at 18.0 cm above the MOT centre. The sharp spike in the distribution is the guided atoms and the broader distribution is due to the ballistically expanded atomic cloud. The aperture size should be large enough to allow the guided atoms to pass through unhindered. The highest achievable loading efficiency for the setup modelled has a beam radius of $w(z) = 349$ μm at the aperture. The $1/e^2$ radius is twice the radial standard deviation: $w(z) = 2\sigma_r$. With this definition the beam radius is $\sigma_r = 175$ μm and therefore the 0.5 mm aperture has a radius of 2.86 σ_r, corresponding to a 99.6% transmission through the aperture. A much

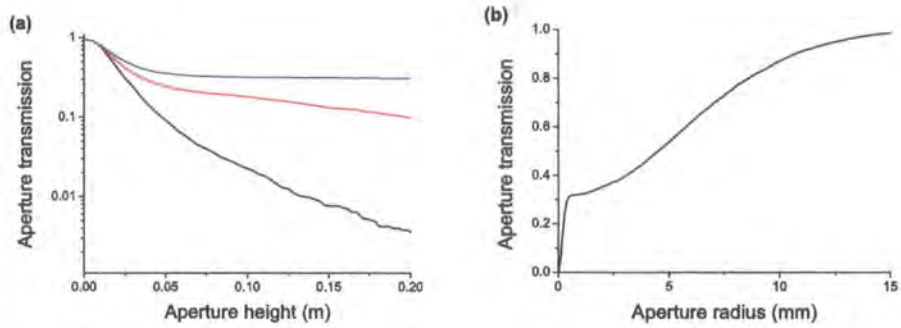

Figure 3.6: Plot (a): Transmission through a 0.5 mm radius aperture is plotted against aperture height above the MOT centre. The black line is with no laser present, the red line is with a laser of waist 100 μm and the blue line is with a 250 μm waist. Plot (b): The transmission is plotted against aperture radius for an aperture at a height of 18.0 cm above the MOT. The distribution consists of a tightly guided core due to a laser of waist 250 μm and the ballistically expanded cloud (σ_r = 5.4 mm). The simulation follows the trajectories of 5,000 atoms to obtain the aperture transmission.

larger beam radius could result in high losses when passing through the small aperture.

3.4.2 Diffraction losses

Away from the focus, diffraction causes the guiding potential to relax. For some bound atoms this can mean their kinetic energy becomes larger than the depth of the confining potential - the atoms are therefore lost from the guide. Ideally a transportation scheme requires a laser profile that doesn't change size on the scale of the guiding distance. The Rayleigh length is a good measure of this, and therefore for efficient guiding one must ensure that the transport distance is on the order or less than the Rayleigh length. A Monte Carlo simulation of 5,000 atoms being transported within the laser guide was run to investigate the loss due to diffraction. In Figure 3.7 (a) the red data points are the ratio of the number of energetically bound atoms at the aperture to the number of initially bound atoms. For small beam waists the Rayleigh length is much smaller than the transport length and the increased diffraction reduces the transport efficiency.

The overall transport efficiency is shown in Figure 3.7 (b). In this plot the fraction of atoms passing through the aperture is plotted against beam waist. In

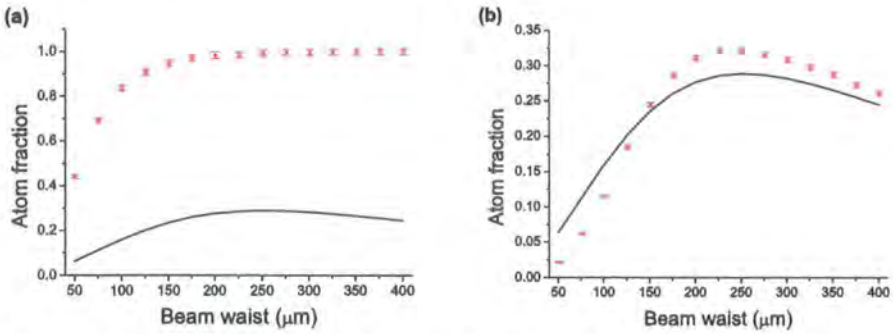

Figure 3.7: Plot (a): The ratio of the number of energetically bound atoms at the aperture to the number of initially bound atoms is plotted against beam waist. Values less than one represent losses due to diffraction. Plot (b): The fraction of atoms passing through the aperture (transport efficiency) is plotted against beam waist. The quantity represents the overall transport efficiency. The solid line in both plots is the loading efficiency χ given by eqn. (3.9).

addition to the fraction of bound atoms passing through the aperture (obtained by multiplying the two curves in Figure 3.7 (a)), there is an extra contribution from nearly bound atoms that have been 'funneled' through the aperture. Those nearly bound were either just outside the bound criteria of eqn. (3.6) at the initial MOT loading, or have been lost from the guide due to diffraction. Their trajectories loosely follow the laser guide, and therefore there is an increased probability of passing through the aperture. Simulations show that the distribution of unbound atoms that are transmitted through the aperture peaks at 6%, which accounts for the extra 4% contribution to the transport efficiency curve in Figure 3.7 (b). The peak in the unbound atom distribution is centred at a smaller beam waist, due to the unbound atoms having a hotter temperature than their bound counterparts. This explains why the transport efficiency curve has its peak shifted to 225 μm.

It is instructive to look at phase-space plots to get an understanding of the initial capture and subsequent loss due to diffraction, see Figure 3.8. The left (right) column simulates a laser with a 100 μm (250 μm) beam waist. The diffraction of the laser beam can be seen by studying the evolution of the thick red $E = 0$ contour. The 250 μm beam provides a better guide as it both captures more atoms initially and suffers from less diffraction loss. In both plots the nearly bound atoms can be seen just outside the $E = 0$ line. It takes a finite time for them to be ejected from the guide. It is these atoms that are the extra contribution in Figure 3.7 (b).

Chapter 3 summary

- The Gaussian laser intensity profile was described.
- A numerical simulation of an experiment to guide a vertically launched atomic cloud was outlined.
- An analytical formula for guide loading was derived. The beam parameters were optimised to produce a loading efficiency of 28.9% into the guide.
- The truncation and diffraction loss mechanisms from the guide were investigated.

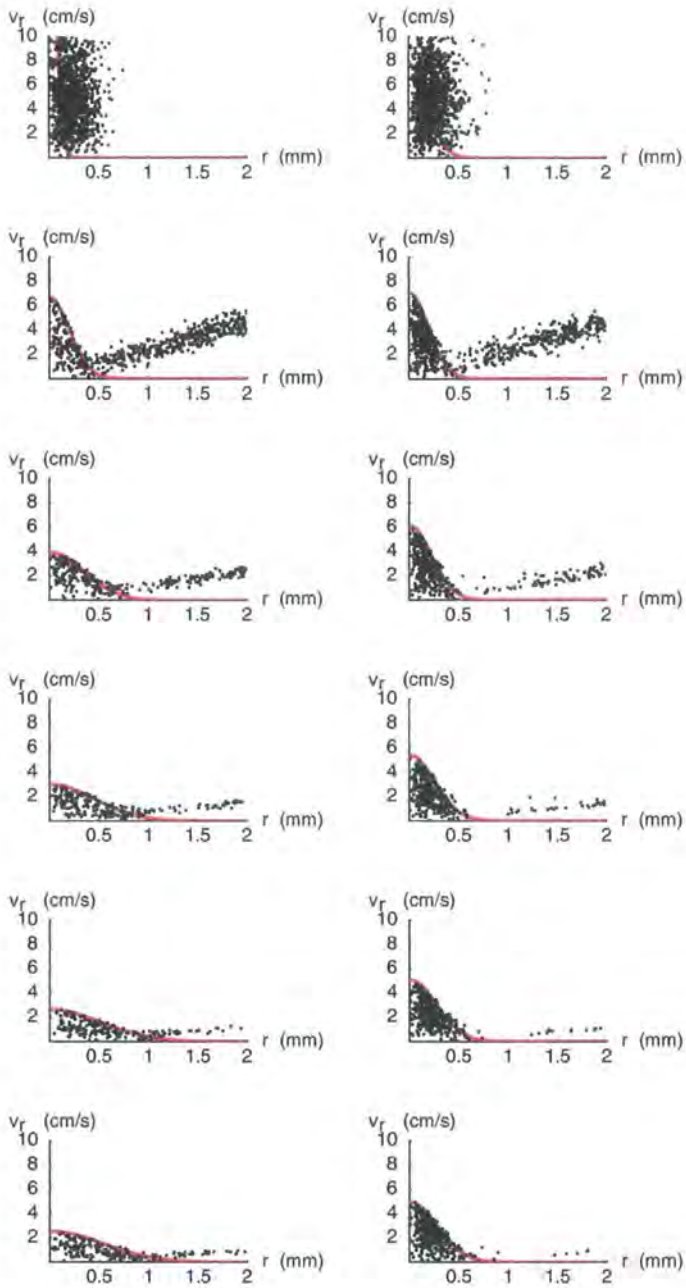

Figure 3.8: Phase-space plots (radial velocity, v_r, versus radial position, r) showing the evolution of atoms within a laser guide for a 100 μm (left column) and 250 μm (right column) beam waist. Proceeding down the page, the times are $t = 0, 42, 85, 127, 169$ and 212 ms. The red line on the plot is the $E = 0$ energy contour.

Chapter 4

Magnetic lens design

"Perfection is achieved, not when there is nothing more to add, but when there is nothing left to take away." Antoine de Saint-Exupery

This chapter will describe how the Stern-Gerlach force can be harnessed to produce magnetic lenses for cold atoms. Work contained within this chapter led to the publication of refs. [145, 146] and has been done in collaboration with the other authors.

4.1 The Stern-Gerlach force

An atom in a magnetic field of magnitude B experiences a magnetic dipole interaction energy of $U_B = -\mu_\zeta B$, where μ_ζ is the projection of the atom's magnetic moment onto the field direction. Provided that Majorana spin-flip transitions [147] are avoided (i.e. the rate of change of direction of the field is less than the Larmor frequency) the magnetic moment adiabatically follows the field.

The Stern-Gerlach force is $\mathbf{F}_{\mathrm{SG}} = -\nabla U_B = \nabla(\mu_\zeta B)$. The ensemble (of alkali metal atoms) can be optically pumped into either a strong-field-seeking state with $\mu_\zeta = \mu_{\mathrm{B}}$ (where μ_{B} is the Bohr magneton), or into a weak-field-seeking state with $\mu_\zeta = -\mu_{\mathrm{B}}$. In low field, where the quantum numbers F and m_F are good, these states are the stretched states $|F = I_{\mathrm{n}} + 1/2, m_F = \pm F\rangle$.

Atoms in these states have a magnetic moment which is independent of field, consequently the Stern-Gerlach force takes the simpler form $\mathbf{F}_{SG} = \pm\mu_B \nabla B$ — i.e. the focusing of the atoms is governed by the gradient of the magnetic field magnitude only. In Figure 4.1 the Breit-Rabi diagram for a ^{85}Rb atom shows the magnetic moment is independent of magnetic field in the stretched states for all fields, and all states for $B < 300$ G.

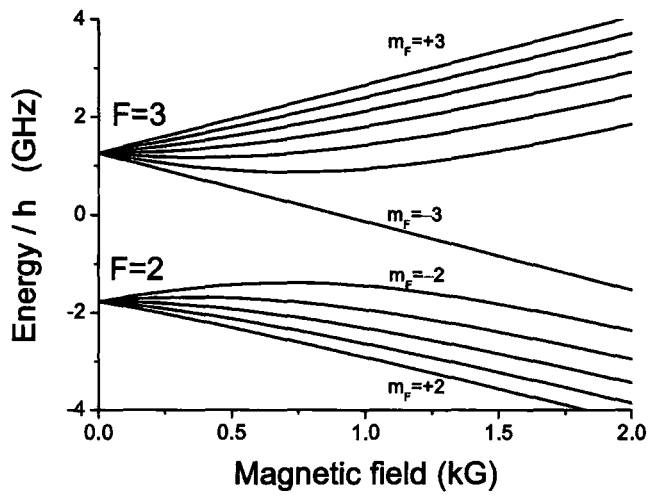

Figure 4.1: The energy shift is plotted against magnetic field for the ground-state hyperfine levels of a ^{85}Rb atom. The *Breit-Rabi formula* used to produce this plot can be found in most standard atomic physics text books (see for example ref. [128]).

The choice of whether atoms in weak or strong-field seeking states are launched depends on the particular application. For some applications, e.g. loading a remote dipole trap, or a secondary magneto-optical trap, it does not matter which atomic state is used. However, for loading into a magnetic trap, weak-field seeking states are required as a maximum of the magnetic field in free space is forbidden by Earnshaw's theorem [148, 149].

4.2 The principle of magnetic lenses

A purely harmonic magnetic field magnitude will result in an aberration-free lens. This chapter will consider current-carrying wires assembled to give two

different kinds of second order magnetic field magnitude:

$$B_{1D}(x,y,z) = B_0 + \frac{B_2}{2}\left(-x^2/2 - y^2/2 + (z-z_c)^2\right), \tag{4.1}$$

$$B_{3D}(x,y,z) = B_0 + B_1(z-z_c) + \frac{B_2}{2}\left(x^2 + y^2 + (z-z_c)^2\right). \tag{4.2}$$

B_0, B_1 and B_2 are the bias field, the axial gradient and the field curvature, respectively. In both cases these parameters are chosen to prevent the field magnitude exhibiting zeros in the region of interest, thus avoiding Majorana spin-flip transitions [147]. The point $\{0,0,z_c\}$ defines the centre of the lens. A lens of the form of B_{1D} can be used either to focus axially or radially. A lens of the form of B_{3D} is used to focus isotropically in 3D with a single lens pulse for atoms in weak-field-seeking states, as Earnshaw's theorem ensures $B_2 \geq 0$ in this case.

The accelerations associated with these magnetic fields for weak-field seeking atoms of mass m are:

$$\mathbf{a}_{1D} = -\omega^2\{-x/2, -y/2, (z-z_c)\}, \tag{4.3}$$

$$\mathbf{a}_{3D} = -\omega^2\{x, y, (z-z_c)\} + \mathbf{a}_0, \tag{4.4}$$

where $\omega^2 = \mu_B B_2/m$ is a useful measure of the power of the lens and $\mathbf{a}_0 = \{0, 0, \mu_B B_1/m\}$ is a constant acceleration arising from the axial magnetic gradient. To work with strong-field seeking atoms the sign of the acceleration is changed. The harmonic accelerations in both eqn. (4.3) and eqn. (4.4) are harmonic about $\{0,0,z_c\}$ and lead to three separable one-dimensional simple harmonic oscillator equations for the atomic motion.

Note that for the 1D case (eqn. (4.3)) the axial curvature is twice the magnitude of and opposite in sign to the radial curvature, ${\omega_z}^2 = -2{\omega_r}^2$. The acceleration of eqn. (4.3) results in a lens which is axially converging (diverging) and radially diverging (converging) if B_2 is positive (negative). In order to achieve a 3D focus with such lenses, an axially converging lens pulse must be followed by an appropriately timed axially diverging lens (or vice versa). This alternate-gradient focusing strategy is the subject of Section 4.6.

4.3 Magnetic fields from current bars and circular coils

This work considers straight current bars and circular coils for the formation of lenses. The Biot-Savart law yields magnetic fields that are analytic for both finite- and infinite-length current bars.

$$\mathbf{B}(x,y,z) = \frac{\mu_0 I'}{4\pi} \int \frac{d\mathbf{l} \times \hat{\mathbf{r}}}{r^2}. \tag{4.5}$$

Here I' is the current in the bar, $d\mathbf{l}$ is the differential length vector of the current element, and $\hat{\mathbf{r}} = \mathbf{r}/r$ is the unit vector in the direction of $\mathbf{r}$. For a current bar of finite-length L, aligned along the z-axis, the magnetic field is:

$$\mathbf{BZ}(x,y,z) = \frac{\mu_0 I'}{4\pi} \int_{-L/2}^{L/2} \frac{1}{(x^2+y^2+(z-l)^2)^{3/2}}\, dl\, \{-y, x, 0\}, \tag{4.6}$$

with similar expressions for bars along the x- and y-axis. The solution to the integral is:

$$\begin{aligned}\mathbf{BZ}(x,y,z) =& \frac{\mu_0 I'}{4\pi} \frac{\{-y,x,0\}}{x^2+y^2} \times \\ & \left(\frac{L-2z}{\sqrt{4(x^2+y^2)+(L-2z)^2}} + \frac{L+2z}{\sqrt{4(x^2+y^2)+(L+2z)^2}} \right).\end{aligned} \tag{4.7}$$

A much simpler result is produced when an infinitely long current bar is used:

$$\mathbf{BZ}(x,y,z) = \frac{\mu_0 I'}{4\pi} \frac{2\{-y,x,0\}}{x^2+y^2}. \tag{4.8}$$

For circular coils, with axes aligned along the z-axis, the magnetic field can be expressed in terms of elliptic integrals [150]. For a coil of radius a with N turns carrying a current of I Amps, the magnetic field in cylindrical polar co-ordinates, $\mathbf{B}(r,z) = \{B_r, B_z\}$, is given in SI units by:

$$\begin{aligned} B_r(r,z) &= \frac{\mu_0 N I}{2\pi} \frac{z}{r\left[(a+r)^2+z^2\right]^{1/2}} \left[-K(k^2) + \frac{a^2+r^2+z^2}{(a-r)^2+z^2} E(k^2) \right], \\ B_z(r,z) &= \frac{\mu_0 N I}{2\pi} \frac{1}{\left[(a+r)^2+z^2\right]^{1/2}} \left[K(k^2) + \frac{a^2-r^2-z^2}{(a-r)^2+z^2} E(k^2) \right], \end{aligned} \tag{4.9}$$

$$\text{where} \qquad k^2 = \frac{4ar}{(a+r)^2 + z^2}\,. \tag{4.10}$$

Here $K(k^2)$ and $E(k^2)$ are the complete elliptic integrals of the first and second kind respectively. When $k = 0$ these reduce to $K(0) = E(0) = \pi/2$. The magnetic field magnitude is given by $B = \sqrt{{B_r}^2 + {B_z}^2}$. In Figure 4.2 the magnetic field magnitude for a 5 cm coil with $NI = 10,000$ Amps is plotted. The positive (negative) curvature in the radial (axial) direction is evident.

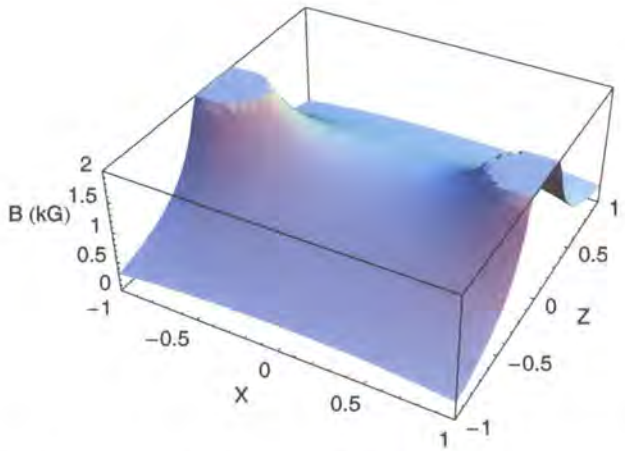

Figure 4.2: The magnetic field magnitude for a 5 cm coil ($NI = 10,000$ Amps) is plotted against the scaled distances $X = x/a$ and $Z = z/a$.

A discussion of the form of the contours of magnetic field magnitude for various magnetic trapping configurations has been provided by Bergeman *et al.* [151]. The fields are constrained by Maxwell's equations, which, in conjunction with symmetry arguments, allow the spatial dependence of the fields to be parameterised with a small number of terms. In particular, for a cylindrically symmetric magnetic coil configuration, the fourth-order on-axis 1D magnetic field, $B_z(r = 0, z) = \sum_{i=0}^{4} B_i\, z^i/i!$, gives the complete fourth-order 3D magnetic field:

$$\begin{aligned}\mathbf{B}(r,z) \;=\; & \left\{-\frac{B_1}{2}r - \frac{B_2}{2}rz,\, B_0 + B_1 z + \frac{B_2}{2}\left(z^2 - \frac{r^2}{2}\right)\right\} + \\ & B_3\left\{\frac{r^3}{16} - \frac{rz^2}{4},\, \frac{z^3}{6} - \frac{r^2 z}{4}\right\} + B_4\left\{\frac{r^3 z}{16} - \frac{rz^3}{12},\, \frac{z^4}{24} - \frac{r^2 z^2}{8} + \frac{r^4}{64}\right\},\end{aligned} \tag{4.11}$$

with third-order magnitude:

$$B(r,z) = B_0 + B_1 z + \frac{1}{2}B_2 z^2 + \frac{1}{2}\left(\frac{{B_1}^2}{4B_0} - \frac{B_2}{2}\right) r^2 + B_3\frac{z^3}{6} + r^2 z\left(-\frac{B_3}{4} + \frac{B_1 B_2}{4B_0} - \frac{{B_1}^3}{8{B_0}^2}\right). \tag{4.12}$$

If, in addition, the coil system is axially-symmetric the magnitude to fourth order is:

$$B(r,z) = B_0 + \frac{1}{2}B_2(z^2 - r^2/2) + B_4\left(\frac{z^4}{24} + \frac{r^4}{64}\right) + \frac{r^2 z^2}{8}\left(-B_4 + \frac{{B_2}^2}{B_0}\right). \tag{4.13}$$

Let us consider two coils of N turns with radius a, separation s, carrying currents I_1 and I_2. It is convenient to partition the currents in each coil as a current I_{H} with the same sense and a current I_{AH} in opposite senses, i.e. $2I_{\mathrm{H}} = I_1 + I_2$, $2I_{\mathrm{AH}} = I_1 - I_2$. If one defines $\eta = \mu_0 NI/2$, and uses the scaled separation $S = s/a$, the axial magnetic field is thus:

$$B(0,z) = \left(\frac{(\eta_{\mathrm{H}} + \eta_{\mathrm{AH}})}{a(1 + (z/a - S/2)^2)^{3/2}} + \frac{(\eta_{\mathrm{H}} - \eta_{\mathrm{AH}})}{a(1 + (z/a + S/2)^2)^{3/2}}\right), \tag{4.14}$$

yielding the axial Taylor expansion terms:

$$\begin{aligned}
B_0 &= \frac{2\eta_{\mathrm{H}}}{a\,(1 + S^2/4)^{\frac{3}{2}}},\\
B_1 &= \frac{3\eta_{\mathrm{AH}} S}{a^2\,(1 + S^2/4)^{\frac{5}{2}}},\\
B_2 &= \frac{6\eta_{\mathrm{H}}\,(S^2 - 1)}{a^3\,(1 + S^2/4)^{\frac{7}{2}}},\\
B_3 &= \frac{15\eta_{\mathrm{AH}} S\,(S^2 - 3)}{a^4\,(1 + S^2/4)^{\frac{9}{2}}},\\
B_4 &= \frac{45\eta_{\mathrm{H}}\,(S^4 - 6S^2 + 2)}{a^5\,(1 + S^2/4)^{\frac{11}{2}}}.
\end{aligned} \tag{4.15}$$

The expressions of eqn. (4.15) will be utilised in the next section where various configurations of coils and bars for realising magnetic lenses are considered.

4.4 Configurations for realising magnetic lenses

There are six distinct coil and current bar configurations used for focusing in this thesis. Figure 4.3 displays these six strategies, whilst Figure 4.4 shows the associated magnetic field information. Strategies I-III lead to the axial/radial focusing of eqn. (4.3), whereas strategies IV-VI lead to the isotropic 3D focusing of eqn. (4.4). Strategies I-V deal with cylindrically symmetric coil arrangements.

4.4.1 Strategy I: a single coil

Figure 4.3 I shows the geometry of this lens. The magnetic field magnitude at the centre of a single coil of radius a with NI_1 current turns is characterised by the coefficients in eqn. (4.15) with $S = 0$ and using $I_2 = 0$ when evaluating η_{H}. The curvature is:

$$\omega_z{}^2 = -2\omega_r{}^2 = \frac{\mu_{\mathrm{B}} B_2}{m} = -\frac{3\mu_0 \mu_{\mathrm{B}} N I_1}{2ma^3}. \tag{4.16}$$

The radial curvature is positive, thus, a single coil can be used to radially focus weak-field seeking atoms. However, this lens has an axial curvature that is negative and twice the magnitude, resulting in axial defocusing.

4.4.2 Strategies II and III: a pair of axially-displaced coils ($I_1 = I_2$)

Figure 4.3 II and III show the geometry of these lenses. For a pair of separated coaxial coils, where both coils have equal current with the same sense, an axially diverging (converging) lens is realised for separations less (greater) than the coil radius:

$$\omega_z{}^2 = -2\omega_r{}^2 = \frac{\mu_{\mathrm{B}} B_2}{m} = \frac{6\mu_{\mathrm{B}}\eta_{\mathrm{H}}\left(S^2 - 1\right)}{ma^3\left(1 + S^2/4\right)^{7/2}}. \tag{4.17}$$

The lens curvature is zero when the separation equals the coil radius (the Helmholtz condition for achieving uniform fields). The B_2 term in eqn. (4.15) is plotted in Figure 4.5.

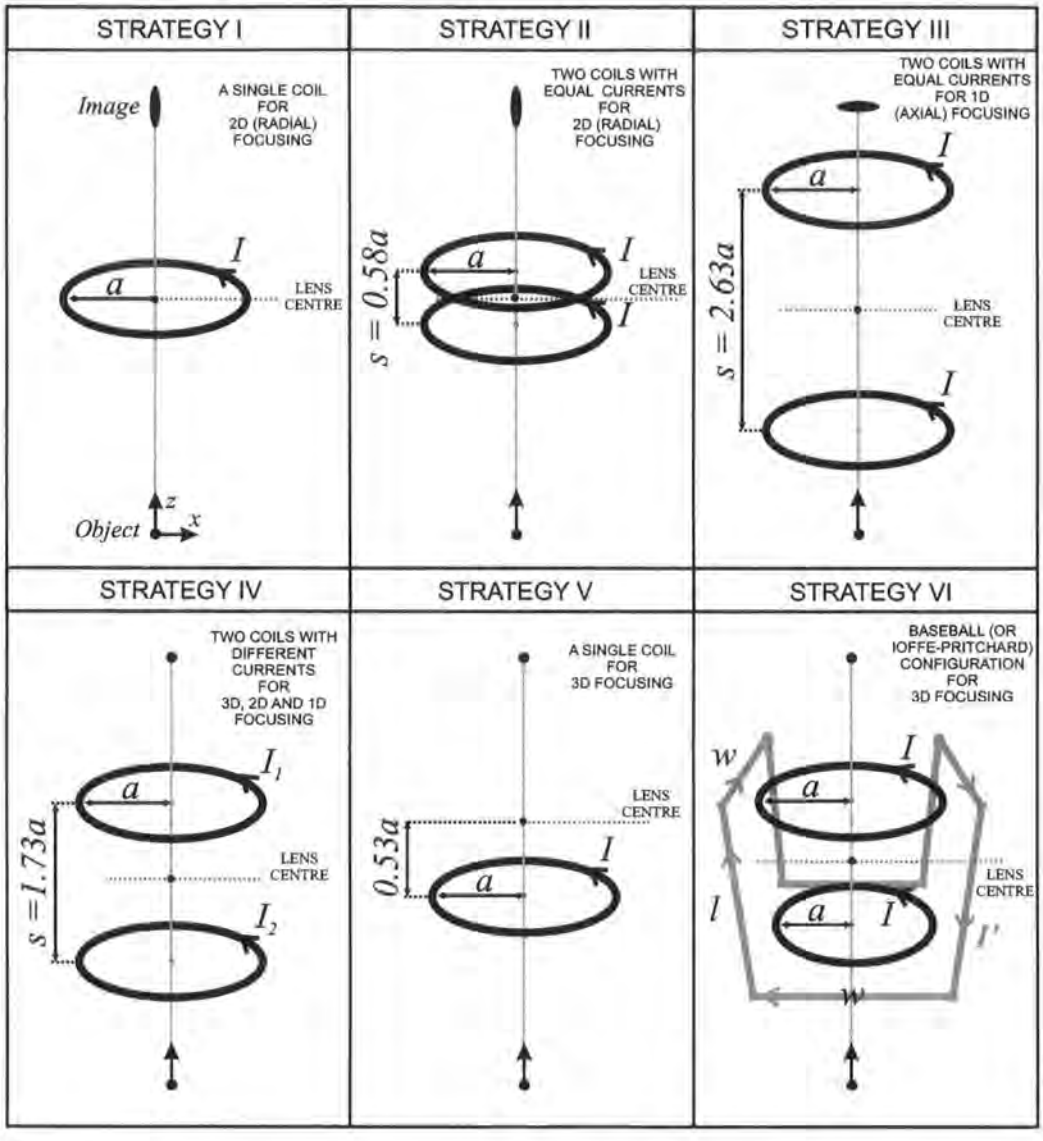

Figure 4.3: The six different lens strategies detailed in the text. Strategy I utilises the centre of a single coil; Strategies II and III use the geometric centre of a pair of coaxial coils (carrying equal currents in the same sense) with separations of S=0.58 and S=2.63 coil radii, respectively; Strategy IV uses the geometric centre of a pair of coaxial coils with unequal currents and a relative separation $S = \sqrt{3}$; Strategy V uses a single coil axially offset to $z/a = \pm\sqrt{2/7}$; Strategy VI uses the geometric centre of a Baseball coil with dimensions $w = l = 2a$ combined with a coaxial coil pair with $S = 1$. [Figure generated in collaboration with D. A. Smith.]

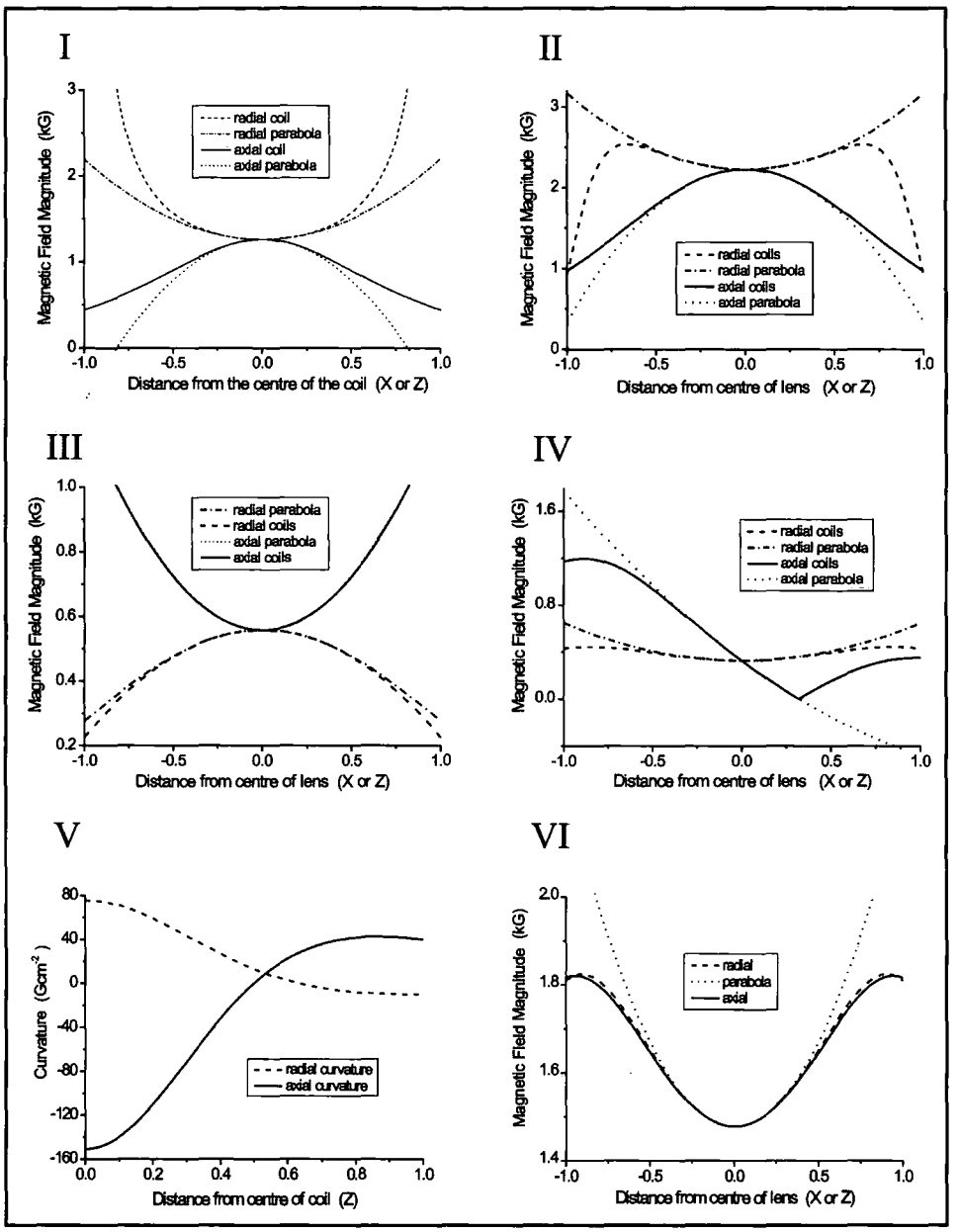

Figure 4.4: The respective axial and radial variation of the magnetic field magnitude associated with the six lens strategies I-VI of Figure 4.3 is plotted. $X = x/a$ and $Z = z/a$ are the scaled displacements from the centre of the lens. In Image IV the axial gradient in the magnetic field magnitude alters the centre-of-mass velocity of an atom cloud but does not lead to lensing. Parabolic approximations to the field magnitudes are also given. In Image V the field curvature rather than the magnitude is plotted, this indicates the point where the lens becomes isotropic. [Figure generated in collaboration with D. A. Smith.]

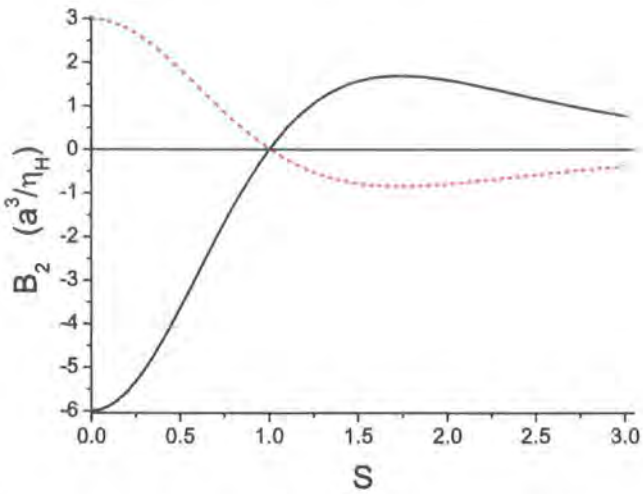

Figure 4.5: The second order Taylor expansion term, B_2, is plotted against the scaled separation S. The black line represents the axial curvature and the dotted red line is the radial curvature $(-B_2/2)$.

Since Strategies II and III are axially-symmetric configurations there are no third order terms. The third term in eqn. (4.13) is zero when $B_4 = 0$, which occurs if $S = \sqrt{3 \pm \sqrt{7}} = 0.595$ or 2.38. The fourth term in eqn. (4.13) is zero when $B_4 B_0 = {B_2}^2$, which occurs if $S = \sqrt{\frac{1}{3}(13 \pm \sqrt{145})} = 0.565$ or 2.89. The *harmonicity*[1] of a radial-focusing lens ($S < 1$ Strategy II) is thus optimised if the relative coil separation is $S = 0.58$, whereas the harmonicity of an axial-focusing lens ($S > 1$ Strategy III) is thus optimised if the relative coil separation is $S = 2.63$.

4.4.3 Strategy IV: a pair of axially-displaced coils ($I_1 \neq I_2$)

Figure 4.3 IV shows the geometry of an isotropic 3D lens formed from two coils carrying different currents. From eqn. (4.12) it can be seen that an isotropic 3D lens is formed when ${B_1}^2 = 6 B_2 B_0$, and this can be re-expressed using eqn. (4.15) as:

$$\eta_{\mathrm{AH}} = \pm \eta_{\mathrm{H}} \sqrt{8(1 - 1/S^2)}. \tag{4.18}$$

[1] A word describing how best the lens approximates that of a harmonic potential. It will be defined mathematically in Section 4.5.

From eqn. (4.12) and eqn. (4.15) it can be seen that some of the third-order terms in the magnetic field magnitude are removed by setting $S = \sqrt{3}$ and thus $B_3 = 0$. Therefore $\eta_{\mathrm{AH}} = \pm\frac{4}{\sqrt{3}}\eta_{\mathrm{H}}$ and the coils carry currents of $I_1/I_2 = -2.527$ or -0.396. The existence of the axial gradient B_1, corresponds to the addition of a constant acceleration along the z-axis during the magnetic pulse:

$$\mathbf{a}_0 = \left\{0, 0, \frac{\mu_B B_1}{m}\right\} = \left\{0, 0, \frac{3\mu_B \eta_{\mathrm{AH}} S}{ma^2\left(1 + S^2/4\right)^{5/2}}\right\}. \tag{4.19}$$

The direction in which the acceleration acts depends upon whether the current flow is greater in the higher or lower coil.

Special case: An axial-only lens

Note that the only way to remove all third-order terms is to have $S = \sqrt{3}$ and set ${B_1}^2 = 2B_2B_0$ (i.e. $\eta_{\mathrm{AH}} = \pm\eta_{\mathrm{H}}\sqrt{8/3(1 - 1/S^2)} = \pm\frac{4}{3}\eta_{\mathrm{H}}$,) which corresponds to $I_1/I_2 = -7$ or $-1/7$. Such a design is a purely axial lens and will not cause focusing in the radial direction. Purely radial lenses are achieved when $B_2 = 0$, (i.e. $S = 1$) for non-zero η_{AH} and η_{H}.

4.4.4 Strategy V: an axially offset single coil

At the centre of a single coil the radial and axial curvatures have opposite signs (Strategy I), however, the radial and axial curvatures have different $z-$dependence. At the two axial locations $z = \pm\sqrt{2/7}a$ the curvatures are equal in magnitude and both positive, see Figure 4.4 V. Therefore an impulse applied to a cloud whose centre-of-mass is at either of these positions will lead to isotropic 3D focusing.

4.4.5 Strategy VI: Ioffe-Pritchard configuration

Ioffe-Pritchard (IP) traps are used extensively for atom trapping and are similar to the Ioffe configuration utilised in plasma confinement [152, 153]. One of the simplest forms of this trap is with a pair of coaxial coils to generate both a bias field, B_0, and an axial curvature B_2. Four current bars run parallel to the

z-axis, with each bar running through the corner of a square (with side length $w = Wa$) centred on the axis. The magnitude of the current in each bar is equal, but neighbouring bars have the opposite current sense. This configuration is not strictly radially symmetric, although it is an excellent approximation for small displacements from the axis. The four current bars give rise to a transverse magnetic field of the form $\{B_x, B_y\} = B_1'\{x, -y\}$ close to the axis. The coefficient is given by:

$$B_1' = \frac{4\mu_0 I'}{\pi w^2}, \tag{4.20}$$

where I' is the magnitude of the current in a bar, and the prime distinguishes it from the axial gradient defined previously. The magnetic field due to the coils (eqn. (4.11)) and bars is to second-order:

$$\mathbf{B}(x,y,z) = B_0\{0,0,1\} + B_1'\{x,-y,0\} + \frac{B_2}{2}\{-xz,-yz,-\frac{1}{2}\left(x^2+y^2\right)+z^2\}, \tag{4.21}$$

which has second-order magnitude [154]:

$$B = B_0 + \frac{1}{2}\left(\frac{B_1'^2}{B_0} - \frac{B_2}{2}\right)\left(x^2+y^2\right) + \frac{B_2}{2}z^2. \tag{4.22}$$

For the purposes of magnetic focusing an isotropic IP trap is required, and this is achieved for the condition:

$$B_1'^2 = \frac{3}{2}B_0 B_2. \tag{4.23}$$

The shape of the magnetic field magnitude contours depend on the geometry of the trap and the ratio of the coil current to the bar current. Using eqn. (4.15) and eqn. (4.20), the above condition can be rearranged into a more practical form:

$$\frac{I'}{NI} = 3\pi W^2\sqrt{\frac{S^2-1}{(2+S^2/2)^5}}. \tag{4.24}$$

In BEC experiments, variants of the IP trap described above are used, since infinitely-long current bars are not realisable. An elegant winding pattern is the baseball geometry. A baseball coil has an axial curvature in addition to a radial gradient, and these quantities can no longer be independently varied. Figure 4.3 Strategy VI shows the cuboidal baseball geometry, where the sides

have lengths $w = Wa$, $w = Wa$ and $l = La$, (l is along the z-axis). It is impossible to realise a 3D isotropic lens solely by adjusting the aspect ratio of the coils w/l, and for this reason we add a coaxial pair of coils carrying equal currents in the same sense (if $\eta_{\mathrm{AH}} \neq 0$ then the equality of the x and y curvatures is broken). The magnetic field magnitude has a third-order Taylor expansion:

$$B = B_{\mathrm{f0}} + \left(\frac{B_1'^2}{2B_{\mathrm{f0}}} - \frac{B_{\mathrm{f2}}}{4}\right)(x^2+y^2) + \frac{B_{\mathrm{f2}}}{2}z^2 + \left(B_3' - \frac{B_{\mathrm{f2}}B_1'}{2B_{\mathrm{f0}}}\right)(y^2-x^2)z, \quad (4.25)$$

where dashed terms indicate contributions solely from the baseball coil, and the subscript f is used when one must add together the B_0, B_2 Taylor contributions from the circular coils (eqn. (4.15)) and B_0', B_2' from the following baseball coil Taylor terms:

$$\begin{aligned}
B_0' &= \frac{4\mu_0 I' W^2}{\pi a\,(L^2+W^2)\sqrt{L^2+2W^2}}, \\
B_1' &= \frac{4\mu_0 I'\,(L^5+3L^3W^2+4LW^4)}{\pi a^2 W^2 (L^2+W^2)^2\sqrt{L^2+2W^2}}, \\
B_2' &= \frac{16\mu_0 I'\,(6L^6W^2+18L^4W^4+11L^2W^6-5W^8)}{\pi a^3\,(L^2+W^2)^3\,(L^2+2W^2)^{\frac{5}{2}}}, \\
B_3' &= \frac{48\mu_0 I'\,(-5L^7W^2-10L^5W^4+11L^3W^6+24LW^8)}{\pi a^4 (L^2+W^2)^4 (L^2+2W^2)^{\frac{5}{2}}}.
\end{aligned} \quad (4.26)$$

The finite-length current bars lead to a non-trivial relationship among the parameters for realising an isotropic lens by adjusting the circular coil bias-field and curvature. From eqn. (4.25) the isotropic condition for a baseball coil is:

$$B_1'^2 = \frac{3}{2}B_{\mathrm{f0}}B_{\mathrm{f2}}\,. \quad (4.27)$$

The simplest isotropic lens to calculate is when circular Helmholtz coils are used – i.e. $S = 1$, $B_2 = 0$ and the only contribution of the circular coils in eqn. (4.25) is the axial constant field B_0, which is tuned to enable lens isotropy. For the purpose of these calculations the parameters $W = W = L = 2$ for a cubic baseball, with $S = 1$ and a relative circular coil current of $\frac{NI}{I'} = 0.154$ are used.

4.5 The harmonicity of the magnetic lenses

Aberrations are caused by departures of the actual potential from the ideal harmonic potential. The following expression is used to measure the degree of departure from harmonicity of a lens, as a function of the distance from the lens' centre:

$$\epsilon = \frac{|\mathbf{a}_F - \mathbf{a}_H|}{|\mathbf{a}_H - \mathbf{a}_0|}, \tag{4.28}$$

where $\mathbf{a}_0$ is the constant acceleration term (eqn. (4.19)) and $\mathbf{a}_H$ is the harmonic fit (eqn. (4.3) or (4.4)) to the full Biot-Savart lens acceleration $\mathbf{a}_F$. The departure from harmonicity is a function of position, and the cylindrical co-ordinates R and Z are used to plot $\epsilon(R, Z)$ for different coil systems. Note the scaled co-ordinates R and Z are normalised to measure length in units of the coil radius, $R = r/a$ and $Z = z/a$. Figures 4.6 I-VI show the spatial variation of the departure from harmonicity for the six different focusing strategies. The departure from harmonicity averaged over a sphere of radius $0.25\,a$ for the six lens strategies is 0.058, 0.007, 0.009, 0.385, 1.347 and 0.148 respectively. The radially converging lens of Strategy II, and the axially converging lens of Strategy III are almost an order of magnitude more harmonic than the single coil radially converging lens of Strategy I.

The isotropic 3D lens of Strategy IV rapidly becomes anharmonic as one moves axially away from the lens centre because of the axial magnetic field zero illustrated in Figure 4.4 IV. In both Strategy IV and V the lack of axial symmetry means that there are first-order terms in the field magnitude, resulting in a gradient which affects the centre-of-mass motion of the atomic cloud. The main problem with Strategy V is that although both the axial and radial curvatures are equal at the lens centre, they vary rapidly with position. The lens-centre curvatures are also 8.4 times weaker than the axial curvature at the centre of a single coil, leading to longer duration magnetic lensing impulses. The cloud of atoms therefore experiences the lens' axial anharmonicities for a greater period, again compromising the quality of the focus. The baseball lens of Strategy VI is significantly more harmonic than the two coil lens of Strategy IV, which is in turn considerably better than the axially offset single coil lens of Strategy V.

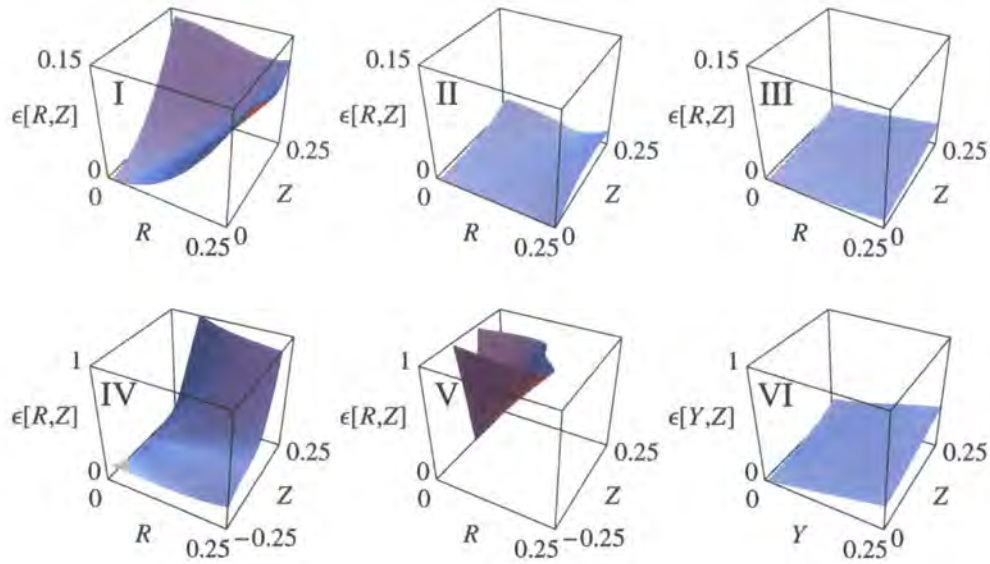

Figure 4.6: The departure from harmonicity $\epsilon(R, Z)$ of the six different lens strategies of Fig. 4.3 is considered for displacements of up to 0.25 coil radii. Averaged over a sphere of 0.25 times the coil radius, the departures from harmonicity for the six configurations are: 0.058, 0.007, 0.009, 0.385, 1.347 and 0.148 respectively. [Figure generated in collaboration with A. S. Arnold.]

4.6 Alternate-gradient focusing

In order to achieve a 3D focus with the lenses of eqn. (4.3), an axially converging lens pulse must be followed by an appropriately timed axially diverging lens (or vice versa). This is referred to as the "alternate-gradient" focusing method, and has the advantage of being able to focus both weak-field and strong-field seeking atoms. This method is used extensively in particle accelerators [155], for focusing polar molecules [27, 28], and is shown in Figure 4.7. The optimised lenses of Section 4.4.2 have been used. Strategy AR refers to an axial focus followed by a radial focus, the opposite is true for Strategy RA. Useful parameters for describing the evolution of a Gaussian atomic cloud are the axial (σ_z) and radial (σ_r) rms cloud radii (the standard deviations), as well as their aspect ratio $\xi = \sigma_z/\sigma_r$.

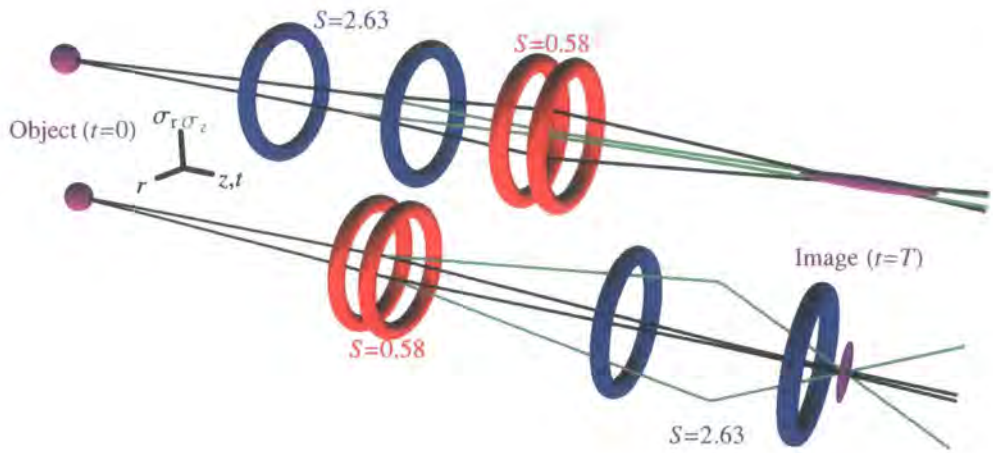

Figure 4.7: The principle of alternate-gradient focusing. The upper image, Strategy AR, shows the evolution of the axial (σ_z, green) and radial (σ_r, black) cloud radii when an axially converging (radially diverging) lens precedes an axially diverging (radially converging) lens and leads to a sausage-shaped cloud ($\xi > 1$). In the lower image, Strategy RA, the lens order is reversed, leading to a pancake-shaped cloud ($\xi < 1$). The effects of gravity (in the $-z$ direction along the coil axis) are not shown, but are included in simulations. Due to the time reversal symmetry of optics, the lens system also works backwards. [Figure generated in collaboration with A. S. Arnold.]

Chapter 4 summary

- The Stern-Gerlach force was introduced and it was shown that it can manipulate cold atoms. The principle of magnetic lenses was described along with six different lens designs. A measure of the degree of departure from harmonicity of a lens was presented.
- A radially (axially) focusing lens is optimised if the scaled separation is $S = 0.58$ ($S = 2.63$).
- An isotropic 3D focus can be made by using a single-impulse of a baseball lens. The condition for achieving isotropy is given in terms of physical parameters of the lens.
- The alternate-gradient approach to producing a 3D focus was outlined.

Chapter 5

Time sequences for pulsed magnetic focusing

"There is a time for everything, and a season for every activity under heaven." Ecclesiastes 3v1

This chapter will describe how the timing sequences are calculated for the magnetic lens pulses. The experimental model described in Section 3.2 is still used to give quantitative results. Initially the laser guide is not used, and magnetic lenses are used to refocus the ballistically expanded cloud. In simulating the lens performance, a maximum of $NI = 10,000$ Amps in the current coils were used. Work contained within this chapter led to the publication of refs. [141, 145, 146] and has been done in collaboration with the other authors.

5.1 $\mathcal{ABCD}$ matrices

The harmonic accelerations in eqn. (4.3) and eqn. (4.4) lead to three separable one-dimensional simple harmonic oscillator equations for the atomic motion. It is useful to employ the $\mathcal{ABCD}$-matrix formulation used widely in geometrical optics. The initial (subscript i) and final position and velocity of an atom along

a given Cartesian axis, say x, are related via the equation:

$$\begin{pmatrix} x \\ v_x \end{pmatrix} = \begin{pmatrix} \mathcal{A} & \mathcal{B} \\ \mathcal{C} & \mathcal{D} \end{pmatrix} \begin{pmatrix} x_\mathrm{i} \\ v_{x_\mathrm{i}} \end{pmatrix}. \tag{5.1}$$

To simplify the effects of gravity, the calculations are performed in a free-falling frame of reference. In this frame the free evolution of the cloud is an isotropic expansion, described by an $\mathcal{ABCD}$ matrix. The influence of a converging or diverging magnetic lens can also be described by $\mathcal{ABCD}$ matrices, as outlined in [52, 156]:

$$M_1(t) = \begin{pmatrix} 1 & t \\ 0 & 1 \end{pmatrix}, \tag{5.2}$$

$$M_2(\omega, \tau) = \begin{pmatrix} \cos\omega\tau & \frac{1}{\omega}\sin\omega\tau \\ -\omega\sin\omega\tau & \cos\omega\tau \end{pmatrix}, \tag{5.3}$$

$$M_3(\omega, \tau) = \begin{pmatrix} \cosh\omega\tau & \frac{1}{\omega}\sinh\omega\tau \\ \omega\sinh\omega\tau & \cosh\omega\tau \end{pmatrix}. \tag{5.4}$$

Matrix M_1 is the translation matrix for a duration t; M_2 is the matrix for a converging lens of strength ω applied for a duration τ; M_3 is the matrix for a diverging lens of strength ω applied for a duration τ. It is interesting to note that the sinusoidal (exponential) path taken by atoms inside a converging (diverging) magnetic lens is in stark contrast to the linear propagation of light rays in an optical lens.

By multiplying these matrices together, one arrives at the final $\mathcal{ABCD}$ system matrix. An image (i.e. a one-to-one map of position between the initial and final cloud) is formed if the condition $\mathcal{B} = 0$ is maintained. In this case the spatial magnification $\mathcal{A}$ is the inverse of the velocity magnification $\mathcal{D}$. This spatial compression and concomitant velocity spread is a manifestation of Liouville's theorem (see for example ref. [144]). The theorem states that phase-space density is conserved in a Hamiltonian system. Time-dependent Stern-Gerlach forces satisfy the criteria for Liouville's theorem to be valid [157]. The cloud extent along x in a given plane is given by:

$${\sigma_x}^2 = (\mathcal{A}\sigma_{x_i})^2 + (\mathcal{B}\sigma_{v_{x_i}})^2, \tag{5.5}$$

where σ_{x_i} is the initial position standard deviation and $\sigma_{v_{x_i}}$ is the initial velocity standard deviation. An *image* is formed for the condition $\mathcal{B} = 0$, but the *smallest cloud size* occurs when one minimises the product of the cloud extent for all 3 spatial dimensions (i.e. $\sigma_x\sigma_y\sigma_z$). For single- and double-impulse lens systems modelled using the full magnetic field expressions, the cloud size at the image plane and the minimum cloud size do not correspond exactly, but they are usually very similar. The rest of this thesis will consider the cloud size at the image plane ($\mathcal{B} = 0$), and thus $\mathcal{A}$ corresponds to the magnification.

5.1.1 Thick and thin lenses

The finite pulse time means the atom's position and velocity will be modified during the pulse and therefore the simple focusing formulae of 'thin lens' optics cannot be used. A mathematical transformation can be made from the lab frame of 'thick lenses' to 'thin lenses'. A thick converging lens M_2 is identical to a thin lens of strength $\mathcal{C}(\omega,\tau) = -\omega\sin(\omega\tau)$ (i.e. the original $\mathcal{C}$ entry of the M_2 $\mathcal{ABCD}$ matrix), pre- and post-multiplied by a translation matrix with duration $\tau'/2$:

$$M_2 = \begin{pmatrix} 1 & \tau'/2 \\ 0 & 1 \end{pmatrix}\begin{pmatrix} 1 & 0 \\ \mathcal{C} & 1 \end{pmatrix}\begin{pmatrix} 1 & \tau'/2 \\ 0 & 1 \end{pmatrix}. \tag{5.6}$$

The effective pulse width τ' is defined as:

$$\tau'(\omega,\tau) = \frac{2}{\omega}\tan\frac{\omega\tau}{2}, \tag{5.7}$$

and the notation of primes is used to denote times in the thin lens representation. This means many of the simplicities of thin lens optics can be used, even when dealing with the more accurate thick lensing behavior. The effective thin lens duration of the pulse τ' differs from the actual pulse duration τ, but otherwise the treatments are identical. In the limit of a short, strong pulse $\omega\tau \to 0$, one finds that $\tau' \to \tau$. If one wishes to consider the diverging lens M_3, merely make the transformation $\omega \to i\omega$ in eqn. (5.6) – i.e. $\mathcal{C} = \omega\sinh(\omega\tau)$ and $\tau' = \frac{2}{\omega}\tanh\frac{\omega\tau}{2}$.

5.2 Single-impulse focusing

A single lens system can be modelled by having a translation of $M_1(t_1')$, where $t_1' = t_1 + \tau'/2$, followed by a thin lens of strength $\mathcal{C}$, followed by a translation of $M_1(t_2')$, where $t_2' = t_2 + \tau'/2$. The $\mathcal{ABCD}$ matrix sequence is:

$$\begin{pmatrix} \mathcal{A} & \mathcal{B} \\ \mathcal{C} & \mathcal{D} \end{pmatrix} = \begin{pmatrix} 1 & t_2' \\ 0 & 1 \end{pmatrix} \begin{pmatrix} 1 & 0 \\ \mathcal{C} & 1 \end{pmatrix} \begin{pmatrix} 1 & t_1' \\ 0 & 1 \end{pmatrix}, \tag{5.8}$$

The physical duration of the focusing is $T = t_1 + t_2 + \tau$, however the thin lens system has a total time $T' = t_1 + t_2 + \tau' = T - \tau + \tau'$, see Figure 5.1.

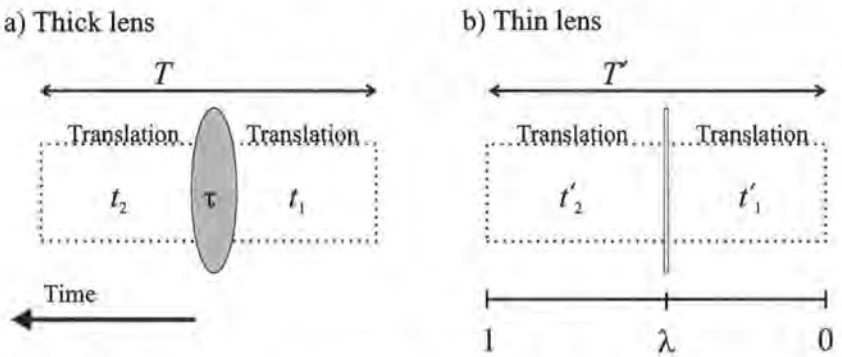

Figure 5.1: A diagram showing the single-impulse timing sequence for the two frames of reference: (a) shows the thick lens or lab frame with the time durations for each stage and (b) shows the mathematically equivalent thin lens representation that is used in the calculations. Note that the direction of time runs right to left so that it visually mirrors the system matrix layout in eqn. (5.8). The dimensionless timing parameter λ is also shown in (b).

For a single lens system, the condition $\mathcal{B} = 0$ is met for the system $\mathcal{ABCD}$ matrix if:

$$\mathcal{C}T' = \frac{1}{\lambda(\lambda - 1)}, \tag{5.9}$$

where a dimensionless parameter to represent the timing of the lens pulse has been defined[1]:

$$\lambda = \frac{t_1'}{T'}. \tag{5.10}$$

This formalism provides a useful way of designing a lens system and investigating its focusing properties.

[1]In hindsight the use of λ is confusing when dealing with wavelengths, however to be consistent with previous work the notation is continued.

The magnification of such a system is given by:

$$M_{\mathrm{ag}} = \frac{(\lambda - 1)}{\lambda}. \tag{5.11}$$

The density increase from a single-impulse isotropic 3D harmonic lens is given by: $-{M_{\mathrm{ag}}}^{-3} = \lambda^3/(1-\lambda)^3$. For a converging lens, eqn. (5.9) becomes:

$$\omega T' \sin \omega\tau = \frac{1}{\lambda(1-\lambda)}. \tag{5.12}$$

Considering an experimental situation where the total time ($T = 212\,\mathrm{ms}$) and the maximum coil current ($NI = 10{,}000$ Amps) are fixed. The geometry of the lens then fixes the maximum strength of the lens. For the specific case of a 4 cm radius Strategy I lens (radial curvature $\omega_r = 98.4\,\mathrm{rad\,s^{-1}}$ from eqn. (4.16)) the analytic result for $\lambda(\omega, \tau)$ is illustrated in Figure 5.2.

The $\lambda(\omega, \tau)$ parameter is maximised (and the magnification M_{ag} is minimised) when:

$$1 - \omega(T - \tau)\cot\omega\tau = 0, \tag{5.13}$$

which has the solution $\lambda = 0.95$ at $\tau = 15.4\,\mathrm{ms}$. This corresponds to a reduction in the radial atomic cloud size by a factor of 19. This is achieved when the pulse duration τ is from time $t = T - \tau$ to $t = T$, i.e. the lens pulse ends at the time of focus. Such focusing in three dimensions would increase the cloud density by more than 3 orders of magnitude. For a lens placed later in time, the magnetic pulse would not have finished at the predicted focal time T, resulting in an increase in cloud size at time T.

The above analysis would seem to suggest that the optimum strategy for achieving the smallest cloud size would be to construct a lens with a short, strong pulse $\omega\tau \to 0$, and use the latest possible pulse time $\lambda \to 1$. However, experimental constraints and lens aberrations alter the above conclusion.

5.2.1 Lenses with a constant $\mathbf{a_0}$ term

In Chaper 4 Strategy IV and V lenses had a constant acceleration, $\mathbf{a}_0$, due to the axial asymmetry. For realistic lens parameters the constant acceleration's magnitude is on the order of 100 m s^{-2} (eqn. (4.19)). Typically the acceleration

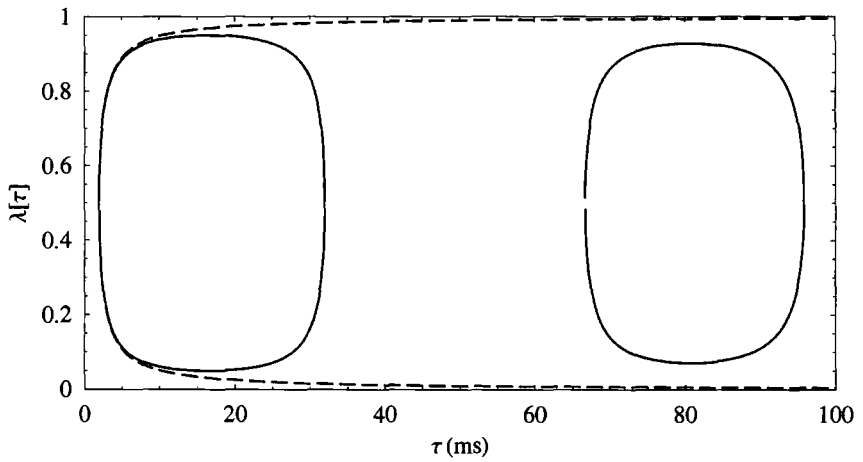

Figure 5.2: By fixing the strength of a Strategy I radially converging lens, ω_r = 98.4 rad s^{-1}, and total experimental focusing time T = 212 ms, one can vary the lens pulse width, τ, and find the focusing parameter $\lambda(\tau)$ via eqn. (5.12). The impulse τ has a minimum of 2.0 ms at $\lambda = 0.5$, and λ is symmetric about this point. Also shown (dashed) is the result obtained if one makes the strong, short pulse approximation $\omega\tau \to 0$, leading to the simplification $\sin\omega\tau \approx \omega\tau$ in eqn. (5.12) - resulting unsurprisingly in a divergence for large pulse durations.

changes the cloud's vertical velocity by about 1 m s^{-1}. Depending on the lens' orientation this can either slow or accelerate the atomic cloud's flight, see Figure 5.3. The initial launch velocity has to be modified to take this change into account so that the cloud apex remains at the required height. As an aside, it should be noted that the ability to accelerate or decelerate a cloud could have uses in a horizontal transport scheme as a means to modify the centre of mass motion.

Based upon a simple trajectory model that incorporates three stages of acceleration ($-g$ when $\{0 < t < t_1\}$ and $\{t_1 + \tau < t < T\}$; $\mathbf{a}_0 - g$ when $\{t_1 < t < t_1 + \tau\}$), and ensuring that the centre of mass comes to rest at a height h, the required launch velocity is:

$$v_{z_i} = \mathbf{a}_0\tau + \sqrt{g(2h + \mathbf{a}_0(t_1 + \tau)(t_1 - \tau))}\,, \tag{5.14}$$

and the apex time of such a flight path is:

$$T = \frac{v_{z_i} - \mathbf{a}_0\tau}{g}\,. \tag{5.15}$$

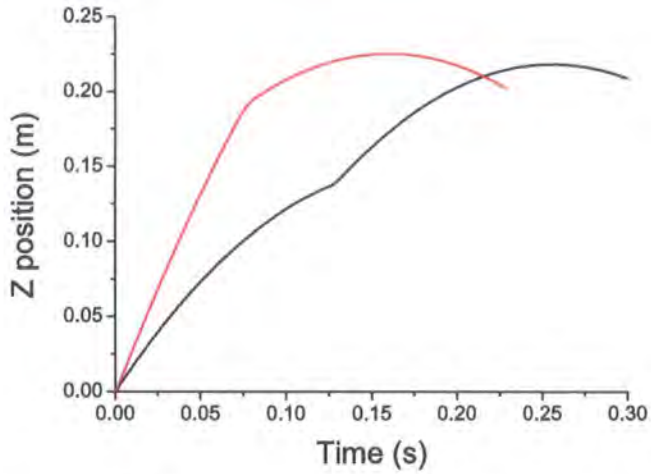

Figure 5.3: The atomic cloud centre of mass' vertical position is plotted against time for a decelerating (red line) and an accelerating (black line) axial-only lens (Strategy IV). The magnetic pulse occurs at $\lambda = 0.5$ and the initial velocity was set so that the apex occurs at $h = 0.22$ m. The decelerating (accelerating) lens requires a faster (slower) launch velocity and the flight time is shorter (longer).

As expected when $\mathbf{a}_0 = 0$ these return to the free-flight launch velocity $v_{z_i} = \sqrt{2gh}$ and apex time $T = \sqrt{2h/g}$. Ensuring that the focus occurs at the same time as the cloud's apex is non-trivial. The pulse length is calculated based upon knowledge of the required focus time, see eqn. (5.12). But the focus time depends upon the location, duration and strength of the magnetic pulse. Solving the problem requires iteration.

A further complication arises in the case of a decelerating lens due to the fact that the vertical launch velocity, v_{z_i}, can become complex for some t_1 and τ values. The physical situation that corresponds to this case is where the desired apex height has been reached before the pulse has finished. One finds that this limits the maximum λ that can be used. The situation is worse for larger radius lenses as these require longer pulse durations to achieve focusing. The accelerating lens does not suffer from this kind of upper bound on λ.

5.3 Double-impulse focusing

A double lens system, see Figure 5.4, comprising of lenses of strength and duration ω_1, τ_1 (starting after a time t_1) and ω_2, τ_2 (starting a time t_2 after the first lens) is modelled by using the following $\mathcal{ABCD}$ matrix sequence:

$$\begin{pmatrix} \mathcal{A} & \mathcal{B} \\ \mathcal{C} & \mathcal{D} \end{pmatrix} = \begin{pmatrix} 1 & t'_3 \\ 0 & 1 \end{pmatrix} \begin{pmatrix} 1 & 0 \\ \mathcal{C}_2 & 1 \end{pmatrix} \begin{pmatrix} 1 & t'_2 \\ 0 & 1 \end{pmatrix} \begin{pmatrix} 1 & 0 \\ \mathcal{C}_1 & 1 \end{pmatrix} \begin{pmatrix} 1 & t'_1 \\ 0 & 1 \end{pmatrix}, \quad (5.16)$$

i.e. a $t'_1 = t_1 + \frac{1}{2}\tau'_1$ translation, then a strength $\mathcal{C}_1$ thin lens, a $t'_2 = \frac{1}{2}\tau'_1 + t_2 + \frac{1}{2}\tau'_2$ translation, then a strength $\mathcal{C}_2$ thin lens followed by a $t'_3 = T' - t'_1 - t'_2$ translation, where $\mathcal{C}_j = -\omega_j \sin(\omega_j \tau_j)$ and $\tau'_j = \frac{2}{\omega_j} \tan(\frac{\omega_j \tau_j}{2})$ for $j \in \{1, 2\}$. The total physical duration of the focusing, T, is fixed, and the effective total time of the double lens system is $T' = T - \tau_1 - \tau_2 + \tau'_1 + \tau'_2$.

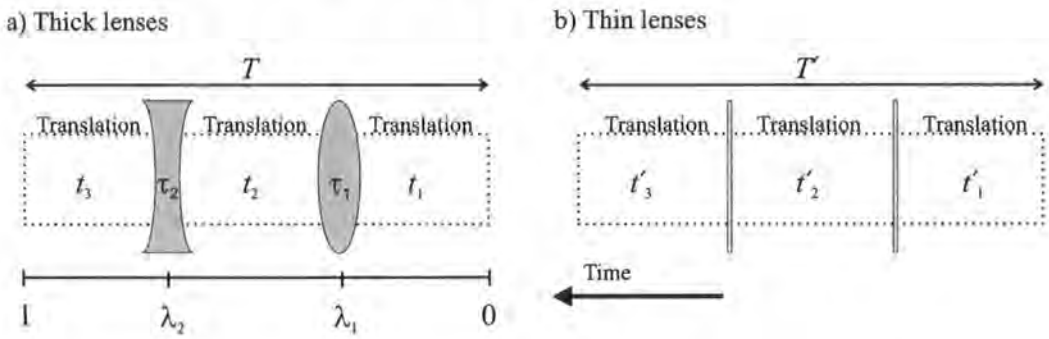

Figure 5.4: A diagram showing the double-impulse timing sequence for the two frames of reference: (a) shows the thick lens or lab frame with the time durations for each stage and (b) shows the mathematically equivalent thin lens representation that is used in the calculations. Note that the direction of time runs right to left so that it visually mirrors the system matrix layout in eqn. (5.16). The dimensionless timing parameters λ_1 and λ_2 are also shown in (a).

The important entries of the system matrix in eqn. (5.16) are $\mathcal{A}$ and $\mathcal{B}$:

$$\mathcal{A} = 1 + (\mathcal{C}_1 + \mathcal{C}_2)(T' - t'_1) + \mathcal{C}_2(-1 + \mathcal{C}_1(T' - t'_1))t'_2 - \mathcal{C}_1\mathcal{C}_2 t'^2_2, \quad (5.17)$$

$$\mathcal{B} = T' + \mathcal{C}_2(T' - t'_1 - t'_2)(t'_1 + t'_2) + \mathcal{C}_1 t'_1 (T' + \mathcal{C}_2(T' - t'_2)t'_2 - t'_1(1 + \mathcal{C}_2 t'_2)), \quad (5.18)$$

which are both second order in t'_1 and t'_2 (and hence also second order in t_1 and t_2).

To obtain an atom cloud which is focused in all 3 dimensions requires that the first lens is axially converging (radially diverging) and the second lens is axially diverging (radially converging), or vice versa. Moreover, the radial (subscript r) and axial (subscript z) spatial dimensions have different $\mathcal{A}$ and $\mathcal{B}$ coefficients. If the two axial lens strengths are ω_{1z} and ω_{2z}, then eqn. (4.17) yields $\omega_{1r} = \mathrm{i}\omega_{1z}/\sqrt{2}$ and $\omega_{2r} = \mathrm{i}\omega_{2z}/\sqrt{2}$. A 3D image is formed when eqn. (5.18) is set equal to zero for both the radial and axial directions.

In Section 5.2 the density increase from a single-impulse isotropic 3D harmonic lens, $\lambda^3/(1-\lambda)^3$, could be characterised by λ, the equivalent time of the thin lens, t_1', relative to the total equivalent focus time T'. Note that for the anisotropic lenses in this section the *equivalent* (i.e. thin lens) timing of a lens in the radial and axial direction is different.

For this reason alternate-gradient lensing is characterised with the parameters:

$$\{\lambda_1, \lambda_2\} = \left\{ \frac{t_1 + \tau_1/2}{T}, \frac{t_1 + \tau_1 + t_2 + \tau_2/2}{T} \right\}, \tag{5.19}$$

corresponding to the mean times of the first and second magnetic impulses relative to the total experimental lensing time T. This labelling is used if ω_{1r} is real (the first lens is radially converging), and the definitions in eqn. (5.19) are swapped if ω_{1r} is imaginary (the first lens is radially diverging). Therefore λ_1 (λ_2) represents the timing of the radially (axially) converging lens.

As before, the coils are assumed to have a 4 cm radius with $NI = 10,000$ Amps in each coil. The two lens combinations in Figure 4.7 are shown in the table below with the resulting angular frequencies.

Strategy	1st lens	ω_{1r}	S_1	2nd lens	ω_{2r}	S_2	ξ
AR	Axial focus	$58\mathrm{i}\,\mathrm{rad\ s^{-1}}$	2.63	Radial focus	$98\,\mathrm{rad\ s^{-1}}$	0.58	> 1
RA	Radial focus	$98\,\mathrm{rad\ s^{-1}}$	0.58	Axial focus	$58\mathrm{i}\,\mathrm{rad\ s^{-1}}$	2.63	< 1

Table 5.1: The two different alternate-gradient strategies modelled. The ω's are the lens strengths of the 4 cm radii coils, S's are the coil separations and $\xi = \sigma_z/\sigma_r$ is the cloud aspect ratio.

For a range of values of τ_1, and τ_2, the radial and axial simultaneous eqns. (5.18) (i.e. $\mathcal{B}_r = 0, \mathcal{B}_z = 0$) are solved to determine t_1 and t_2. Although both $\mathcal{B}_z$ and $\mathcal{B}_r$ are quadratic in t_1 and t_2, substitution for either of these variables leads to a final sextic polynomial equation. This must therefore be solved numerically and leads

to six solution pairs (t_1, t_2). Only solution pairs with real times $0 \leq t_1, t_2 \leq T$ satisfying the condition $t_1 + \tau_1 + t_2 + \tau_2 \leq T$ are considered. The number of (t_1, t_2) solution pairs as a function of τ_1 and τ_2 is shown in Figure 5.5 (a). These (t_1, t_2) solution pairs can then be used to calculate the relative increase in atomic density of a cold atom cloud. From eqn. (5.5) the relative density increase of the image is thus:

$$\rho_{3D} = \frac{{\sigma_R}^3}{((\mathcal{A}_r\sigma_R)^2 + (\mathcal{B}_r\sigma_V)^2)\sqrt{(\mathcal{A}_z\sigma_R)^2 + (\mathcal{B}_z\sigma_V)^2}} \rightarrow \frac{1}{{\mathcal{A}_r}^2\mathcal{A}_z}, \tag{5.20}$$

where σ_R and σ_V are 1D standard deviations of the isotropic cold atom cloud's initial spatial and velocity distributions, and the arrow indicates the limit $\mathcal{B} = 0$. The dimensionless relative density increases obtained for both strategies are shown in Figures 5.5 (b) and (c). These plots are then effectively combined in Figure 5.5 (d) by inverting τ_1, τ_2 to find the relative density increase as a function of the parameters λ_1, λ_2 which are the mean relative times of the radially converging and diverging lens.

Chapter 5 summary

- The $\mathcal{ABCD}$ formalism was introduced to describe lens systems.
- A transformation was used to convert 'thick' parabolic lenses into mathematically equivalent 'thin' lenses.
- An equation to obtain the required pulse length for single-impulse focusing was presented. This was then used to show that there exists a theoretical limit on how small a focus that can be produced.
- A simple model to account for lenses that have a constant acceleration term was explained.
- The method to obtain the correct pulse sequence for focusing using the alternate-gradient scheme was outlined.

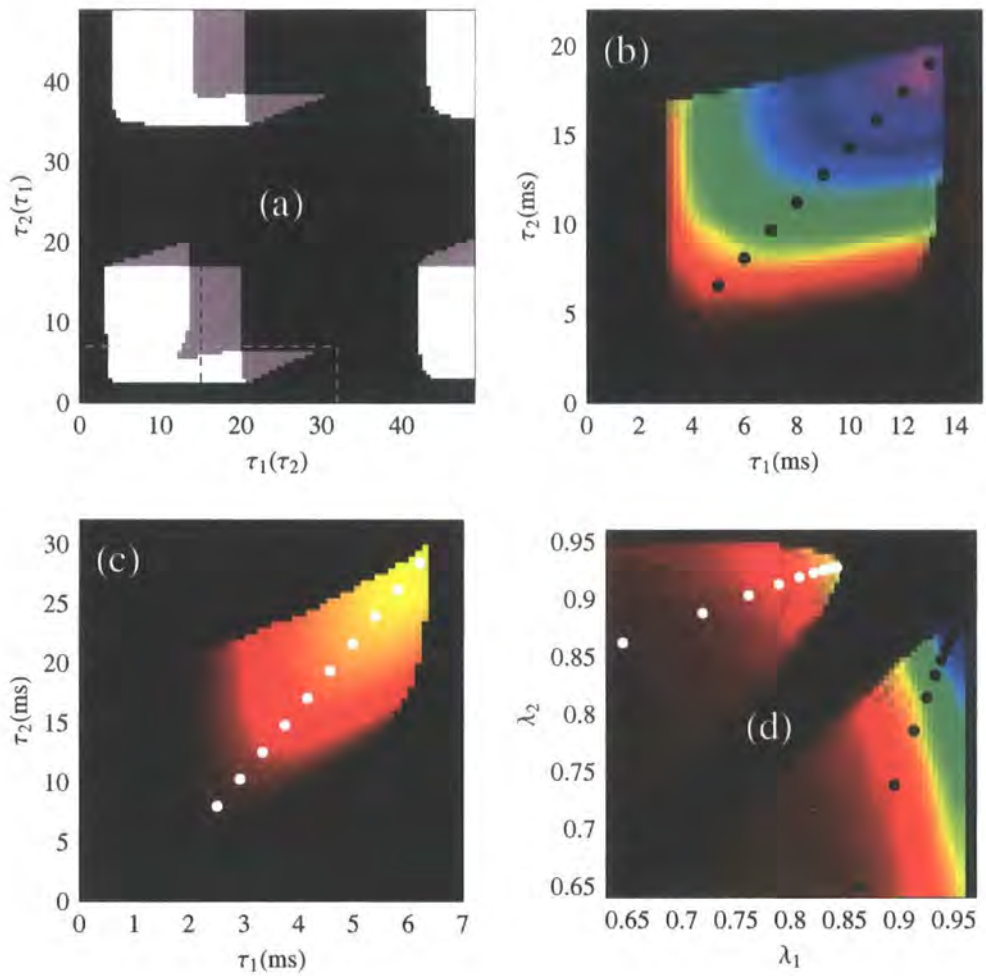

Figure 5.5: Image (a) shows the number of solution pairs (black=0, grey=1, white=2) for (t_1, t_2) as a function of τ_1 and τ_2 (τ_2 and τ_1) in ms for Strategy AR (Strategy RA). The two dashed regions of the 'solution island' lead to the highest relative density increases, shown in (b) for Strategy AR and (c) for Strategy RA. The relative density increase (eqn. (5.20)) if one images a cloud of atoms using: (b) Strategy AR, (c) Strategy RA. The maximum relative density increases are 1100 (320), for a $\xi = \sigma_z/\sigma_r = 17$ sausage ($\xi = 0.094$ pancake) shaped cloud, for images (b) and (c) respectively. The results of (b) and (c) are combined in (d), the relative density increase in terms of λ_1 and λ_2 (the mean times of the radially converging and radially diverging impulses relative to T). The points in images (b)-(d) are used in the next chapter as a sample in simulations. [Figure generated in collaboration with A. S. Arnold.]

Chapter 6

Results: Pulsed magnetic focusing

"You cannot depend on your eyes when your imagination is out of focus."
Mark Twain

The $\mathcal{ABCD}$ matrix formalism outlined in the previous chapter is a useful starting point for studying pulsed magnetic focusing. However, this formalism ignores magnetic aberrations arising due to the departure of the real potential from an ideal parabolic spatial dependence (see Figure 4.6). The attributes of parabolic lenses are unimportant, unless it can be shown that experimentally realistic lenses are sufficiently parabolic for such an approximation to be appropriate. For a non-parabolic potential the change in position and velocity which occur during lensing must be calculated numerically. In this chapter the 'perfect' atomic lens approximations are tested by performing numerical focusing simulations. Work contained within this chapter has led to the publication of refs. [141, 145, 146] and has been done in collaboration with the other authors.

6.1 Methodology

The approach adopted was a numerical simulation, in which the trajectories of typically 5,000 atoms are followed. The cloud and its motion are treated classically, and for the atomic densities encountered in the expanding cloud,

the collision rate is negligible. The atoms travel on ballistic trajectories, except when a magnetic impulse is applied, in which case the full Stern-Gerlach force is included in the numerical integration. The effects of gravity were included, but these effects on the quality of focus were found to be negligible for the parameters used in these simulations.

As in previous chapters, a specific experimental setup described in Section 3.2 is modelled. Initially the focusing is studied without the presence of a laser guide however, and for those simulations a slightly larger MOT size is used ($\sigma_R = 0.4$ mm). In all the simulations the maximum current value in any coil was limited to $NI = 10,000$ Amps. Two measures of the focused cloud size are used and these are outlined below.

6.1.1 Root mean square cloud radius

Useful statistical parameters for describing the evolution of a Gaussian atomic cloud are the time-dependent axial (σ_z) and radial (σ_z) rms cloud radii (the standard deviations), as well as their aspect ratio $\xi = \sigma_z/\sigma_r$. A measure of the harmonicity of a lens can be given by comparing the expected harmonic focus size to the rms radii of the simulated atom cloud at the time of the harmonic focus. The important drawback of this rms approach is that the final location of atoms after a magnetic lens is highly nonlinear with respect to initial conditions. An atom with a velocity in the wings of the initial Gaussian distribution will experience highly anharmonic lensing, as it will be far from the centre of the lens during the magnetic impulse. Thus a few atoms can completely alter the rms width of the cloud.

6.1.2 Atoms in the harmonic region

Another method to quantify the focus is to monitor the fraction of the atoms entering the focus region of a purely harmonic lens. The initial radial and axial cloud standard deviations are σ_R, so the final standard deviations for a harmonic lens are $\sigma_r = \mathcal{A}_r\sigma_R$ and $\sigma_z = \mathcal{A}_z\sigma_R$. By renormalising the dimensions so that the radial and axial dimensions are measured in terms of these final

focus standard deviations, then a sphere with radius $R_0 = 1.53817$ defined by:

$$\frac{\int_0^{R_0} r^2 e^{-\frac{r^2}{2}} dr}{\int_0^{\infty} r^2 e^{-\frac{r^2}{2}} dr} = \frac{1}{2}, \tag{6.1}$$

will contain half of the atoms of the focused Gaussian distribution. This renormalisation process is illustrated in Figure 6.1.

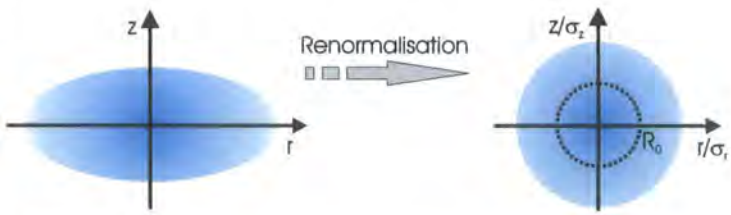

Figure 6.1: The diagram shows how a atomic cloud's dimensions are renormalised by dividing the distances by the final harmonic lens standard deviations. For a harmonic lens the dotted region contains half the atoms.

For numerical simulations the fraction of atoms entering this harmonic focus is measured, and multiplied by twice the relative density increase of a purely harmonic lens (i.e. $2\mathcal{A}_r{}^{-2}\mathcal{A}_z{}^{-1}$) to get a measure of the relative density increase afforded by a real lens. Note that the centre of the harmonic focus region is the final position of an atom initially in the centre of the Gaussian position and velocity distributions. This will lead to a slight underestimation in the density increase (it has been assumed the mean cloud position follows the initial centre-of-mass).

6.2 Single-impulse magnetic focusing

6.2.1 Strategy I: axial defocusing/radial focusing

The simplest implementation of pulsed magnetic focusing is using a single current carrying coil (Strategy I). The trajectories of atoms subject to such a lens are shown in Figure 6.2. The radial direction is focused whereas the axial direction is defocused due to the opposite sign of the magnetic field curvature. Although the lens system is symmetrical, the atom trajectories in the focused radial direction are asymmetrical, which is evidence of lens aberrations.

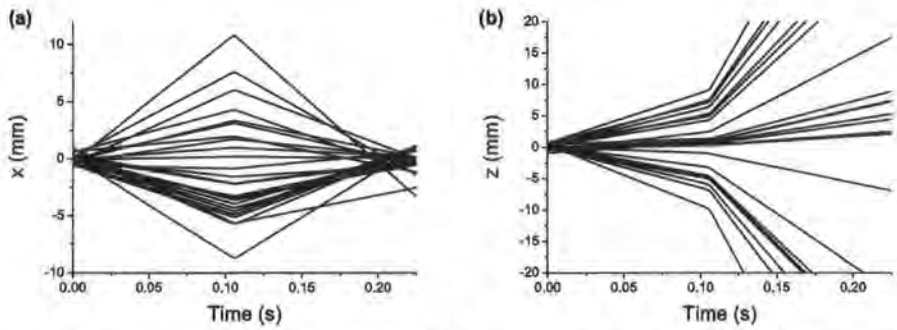

Figure 6.2: The trajectories of 25 atoms subject to a 5 cm Strategy I lens being pulsed on at $\lambda = 0.5$. Plot (a) shows radial distance and (b) shows the axial distance plotted against time.

Figure 6.3 (a) shows the evolution of σ_x for a launched cloud of 500 atoms subject to a radially converging lens constructed from a single coil. The impulse is applied half-way in time, and the length of the impulse is chosen to reverse the transverse velocity, as can be seen from the change in sign of the gradient after $t = 106\,\text{ms}$. For this case, the $\mathcal{ABCD}$ matrix predicts a radial focus with magnification -1, which is in excellent agreement with the numerical simulation using a parabolic lens (using the strength of eqn. (4.16)). The vertical line at $t = 212\,\text{ms}$ corresponds to the imaging time. For real coils, it is seen that the focused cloud image is significantly larger than the initial cloud. The aberration worsens as the coil radius decreases.

Figure 6.3 (b) contains an analysis of the cloud in terms of shells of different radii measured from the centre of the coil; atoms further from the centre are not focused as tightly, and also focus earlier in time. As the ratio between cloud

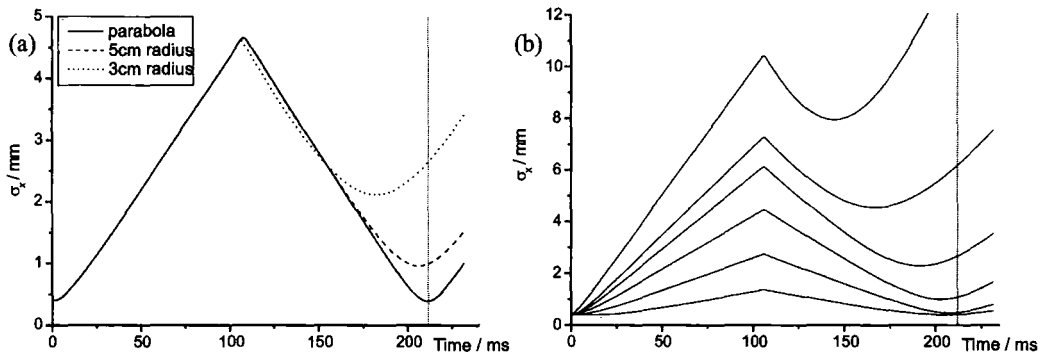

Figure 6.3: (a) Simulation of 500 atoms going through a Strategy I lens ($NI = 10,000$ Amps). The solid, dashed and dotted lines correspond to a parabolic approximation lens, a 5 cm radius lens, and a 3 cm radius lens respectively. The duration and timing of the impulse is chosen using the $\mathcal{ABCD}$ matrix formalism, bringing the atoms to a focus 22 cm above their launch height. (b) A shell plot of 1,000 simulated atoms passing through a 3 cm radius Strategy I lens. The distances from the coil centre are 0-10% of the coil radius, 10-20%, through to 50-60%. Atoms further from the centre are not focused as well, and the focusing occurs at earlier times. Both of these factors degrade the image quality and size.

extent and coil radius decreases, the departure of the field from the parabolic approximation becomes less significant. Therefore one method to reduce the aberrations experienced by the atoms is to increase the coil radius, or decrease the atomic cloud temperature.

Figure 6.4 (a) plots the change in radial cloud size at the predicted focus, σ_x/σ_{x_i}, against coil radius. The optimum coil radius for a Strategy I lens carrying $NI = 10,000$ Amps is 8 cm. The coil radius cannot be increased indefinitely, as even though the lens' harmonicity at the centre will be improved, the pulse duration will also increase; see Figure 6.4 (b). There is both an experimental and theoretical limit to how long the pulse duration can be. The experimental limit is due to long pulse durations causing potentially catastrophic heating in the coil circuit. The theoretical limit is due to the atoms experiencing more of the off-centre lens aberrations, including time-varying lens frequencies, as they move through the lens. The longer the pulse duration, the larger these effects will be.

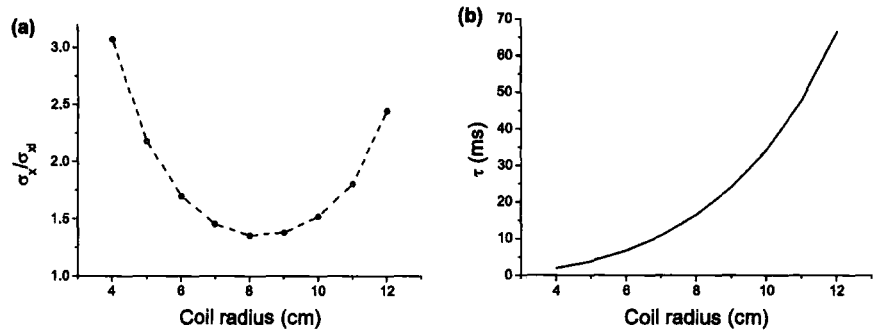

Figure 6.4: (a) The change in radial cloud size, σ_x/σ_{x_i}, at the predicted focus ($T = 212$ ms) is plotted against coil radius for a Strategy I lens ($NI = 10,000$ Amps). (b) The pulse duration, τ, is plotted against coil radius.

6.2.2 Strategies II-III: axial/radial focusing

Another method to reduce performance limiting aberrations is to use an optimised double-coil lens (Strategies II and III). Attention is turned to obtaining the minimum cloud size by investigating the effect of varying the λ parameter, and in the process it will be shown that double-coil lenses out perform their single-coil counterparts. As discussed in Section 5.2, a thin parabolic lens produces the smallest cloud size when $\lambda \rightarrow 1$, i.e. the pulse is applied as late in time as possible. This is a manifestation of Liouville's theorem - a more compact spatial extent can be generated at the expense of a larger velocity spread.

Figure 6.5 shows simulations of radial focusing. The radial cloud expansion factor, σ_x/σ_{x_i}, is plotted as a function of the imaging parameter λ. It can be seen that the smallest cloud size for a parabolic lens (solid line) occurs when one waits as long as possible before focusing, i.e. λ is as close as possible to 1 (limited by the maximum value given by eqn. (5.13)).

The figure also shows how well Strategy I and II lens approximate a parabolic lens. When $\lambda > 0.3$ a 5 cm single-coil lens diverges from the parabolic case and a double-coil starts to diverge when $\lambda > 0.5$. The plot clearly shows that the double-coil produces a lens that better approximates the ideal case. For experimentally-realistic parameters it is seen that it is possible to achieve a final radial cloud size that is smaller than the initial size. At $\lambda = 0.6$ the radial extent of the final cloud is 0.8 times the original radial extent of the cloud.

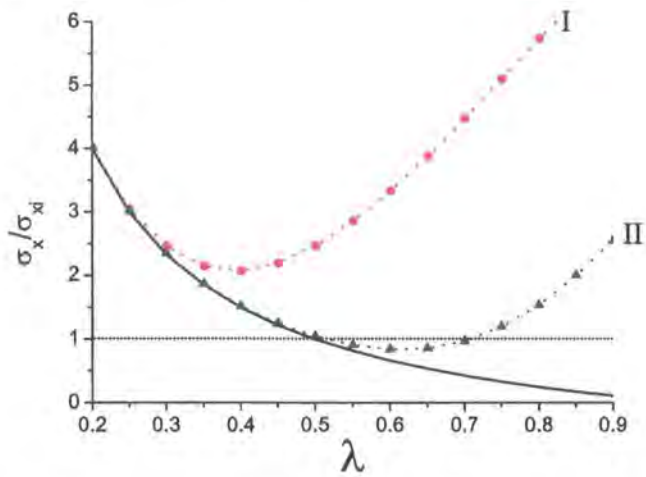

Figure 6.5: The radial expansion factor, at $T = 212\,\text{ms}$, for 5 cm radially converging lenses is plotted against λ. The solid line without symbols shows the parabolic lens solution and the dotted lines with red circles (blue triangles) show the result of atoms passing through a Strategy I (II) lens.

Like its double-coil partner, Strategy III produces an axially converging/radially diverging lens with a high level of harmonicity comparable to that of Strategy II.

Compared to the $\mathcal{ABCD}$ matrix result there is a marked difference in the behaviour of the minimum radially-focused cloud-size for fields from real coils – the value of λ at which the $\mathcal{ABCD}$ minimum is obtained is dominated by aberrations in the magnetic field. The $\mathcal{ABCD}$ matrix approach does not provide an adequate description of pulsed magnetic focusing when one considers the entire atomic cloud.

The easiest way to reduce aberrations further appears to be the use of a very large coil radius. Unfortunately the curvature of the field decreases with the cube of the coil radius (eqn. (4.17)), which necessitates longer pulse durations for larger radius coils. This increase in pulse duration reduces the maximum value of λ that can be used and therefore also limits the minimum cloud size. The aberrations can only be further reduced by increasing the current-turns, something which has experimental limitations.

6.2.3 Strategies IV-VI: isotropic 3D focusing

Isotropic 3D focusing can be achieved using two coils with differing currents (Strategy IV). For realistic experimental parameters, the numerical simulations showed that the aberrations in the lens smeared out any focusing. However, for unrealistically large lens radii and large currents (e.g. 15 cm and 200,000 Amp-turns) it is possible to achieve 3D focusing.

As discussed in Section 4.4.4, a single coil can be made to have isotropic curvature (Strategy V). At $z = \pm\sqrt{2/7}a$, the axial and radial curvatures are equal, and the gradient of the field is non-zero. A numerical simulation was performed for a launched cloud, with an impulse applied when the cloud's centre of mass reached a distance $z = +\sqrt{2/7}a$ from the centre of a single coil. Due to the large departure from harmonicity for the experimentally realistic parameters used, aberrations dominated and focusing was not observed.

The baseball lens (Strategy VI) yields the best isotropic 3D lens. Figure 6.6 shows the temporal evolution of the volume expansion factor, $(\sigma_x\sigma_y\sigma_z/\sigma_{x_i}\sigma_{y_i}\sigma_{z_i})$, for a launched cloud subject to a focusing pulse from a baseball lens. Five different values of λ are depicted, from 0.3 to 0.7 in steps of 0.1. The bias coils have radii of $a = 4\,\text{cm}$, separation $S = 1$, and current $NI = 1,541\,\text{A}$; the baseball has sides of length $W = L = 2$ and current $I' = 10,000\,\text{A}$. These values lead to an angular frequency $\omega = 63\,\text{rad/s}$ in all directions. The minimum cloud size is obtained when $\lambda = 0.3$. At the focal time, $T = 212\,\text{ms}$, the volume has increased by a factor of 50. This is to be contrasted with the 13,000 increase in cloud volume if no magnetic lens was used.

In Figure 6.7 the relative density increase after the baseball lens is plotted in terms of the timing parameter λ. The red dots correspond to the relative density increase using rms widths for the volume. The blue dots show the relative density increase as the fraction of atoms in the harmonic focus zone times twice the harmonic density increase, see Section 6.1.2. It is clear that very different conclusions are reached based on whether the rms radius of the focused atomic cloud, or the fraction of atoms which reach the harmonic focus are considered.

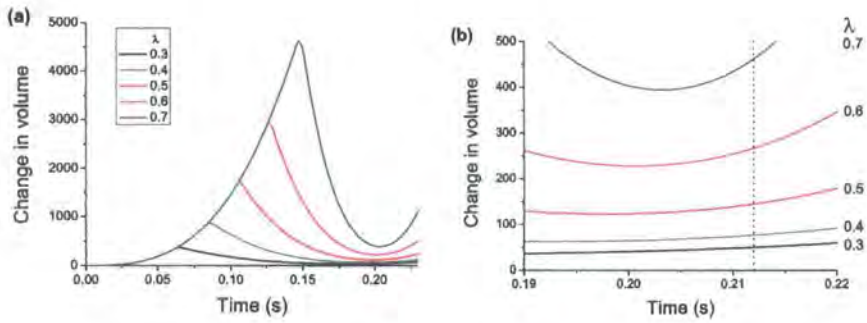

Figure 6.6: (a) A simulation of 1,000 atoms sent through a 4 cm isotropic baseball coil lens (Strategy VI). The ratio of the cloud volume to the initial volume ($\sigma_x\sigma_y\sigma_z/\sigma_{x_i}\sigma_{y_i}\sigma_{z_i}$) is plotted as a function of time for values of λ ranging from 0.3 to 0.7. (b) A close-up of the simulations near the $t = T$ imaging time (vertical line).

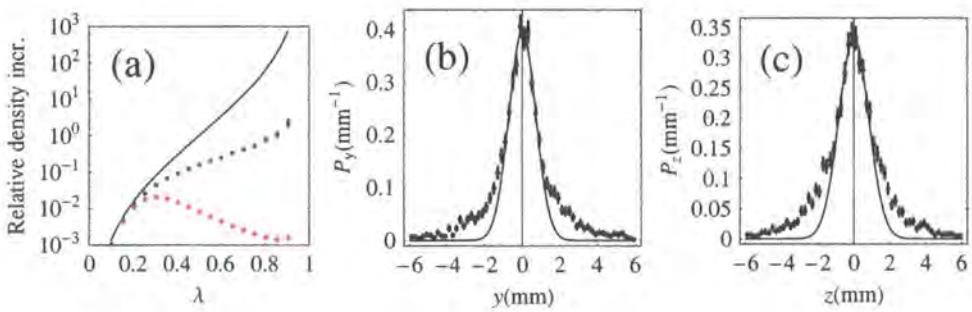

Figure 6.7: Image (a) shows the relative density increase (with error bars, for a 5,000 atom simulation) based on: a purely harmonic lens (black curve), the fraction of atoms in a real lens arriving at the harmonic focus region (blue dots), the ratio of rms cloud volume before and after a real lens (red dots). Images (b) and (c) show the spatial probability distributions at the focus (black dots) in the y and z directions, respectively, where the non-Gaussian wings of the distribution can be clearly seen. These two distributions are taken from the $\lambda = 0.5$ lens simulation, in which case 16% of the atoms are in the harmonic focus region. The Gaussian fits in (b) and (c) (as well as the x distribution) have an area of $\approx 70\%$. [Figure generated in collaboration with A. S. Arnold.]

By only looking at rms widths the optimum lens position occurs at $\lambda = 0.3$, corresponding to a factor of 50 decrease in density. However considering the fraction of atoms in the harmonic focus zone times the harmonic density increase, the optimum position is now $\lambda = 0.9$. The relative density increase is 2.3, which corresponds to 0.3% of the cloud focused to a density 729 times greater than it was originally. The source of this discrepancy between methods can be seen in Figure 6.7 (b-c) where the non-Gaussian wings produce an

over estimate of the rms cloud width. The y and z standard deviations for the Gaussian fits (black curves) are 730 μm and 820 μm respectively; an almost isotropic distribution.

It is interesting to note that for the parameters simulated, the results of a 'pure' Ioffe-Pritchard lens ($W = 2$, $L \rightarrow \infty$ and $S = 2$) are almost identical to the baseball coil. Surprisingly the baseball lens performs better, and produces smaller cloud sizes at the focus. Within the last year, an experiment using the baseball lens described above has been used to isotropically focus Rb atoms; see refs. [158, 159] for more details.

6.3 Magnetic focusing and laser guiding

This section will investigate the axial focusing of an atomic cloud being guided within a 19 W laser beam with a beam waist of 250 μm. Four different lens designs presented in Chapter 4 will be investigated: the special case of Strategy IV that only has axial curvature ($\pm\mathbf{a}_0$); a Strategy II lens that can axially focus strong-field seeking (SFS) atoms; a Strategy III lens that can axially focus weak-field seeking (WFS) atoms. The properties of a 5 cm radius lens are tabulated in Table 6.1 for the four different designs studied. It is interesting to contrast the radial angular frequency of the lens with that of the laser guide. From eqn. (3.5) and the laser parameters above, the laser angular frequency is $\omega_{r_L} = 435$ rad/s. Therefore in the radial direction the laser will dominate over the magnetic field's influence.

	S	NI_1 (A)	NI_2 (A)	a_0 (m/s^2)	ω_r (rad/s)	ω_z (rad/s)	τ (ms)
Axial-only	$\sqrt{3}$	-1,429	10,000	+121	0	49	11.6
lenses	$\sqrt{3}$	10,000	-1,429	-121	0	49	6.6
Strategy II lens	0.58	10,000	10,000	0	70i	100	1.9
Strategy III lens	2.63	10,000	10,000	0	42i	59	5.5

Table 6.1: The focusing properties are tabulated for the 5 cm magnetic lenses used in conjunction with the laser guide. The pulse duration has been calculated for a pulse occurring at $\lambda = 0.5$. The accelerating and decelerating axial-only lenses from Section 4.4.3 are shown in rows 1 and 2. The Strategy II (SFS) and Strategy III (WFS) lenses from Section 4.4.2 are shown in rows 3 and 4. A complex angular frequency corresponds to negative curvature and hence defocusing.

6.3.1 Strategy IV: axial-only focusing

The use of a lens that does not perturb the radial motion would seem an ideal candidate for combining with a laser guide. In Figure 6.8 the combined laser and the full magnetic field potential using elliptic integrals has been plotted. The constant B_1 term, arising from the lens' axial asymmetry, has been subtracted to emphasise the axial curvature and lack of radial curvature.

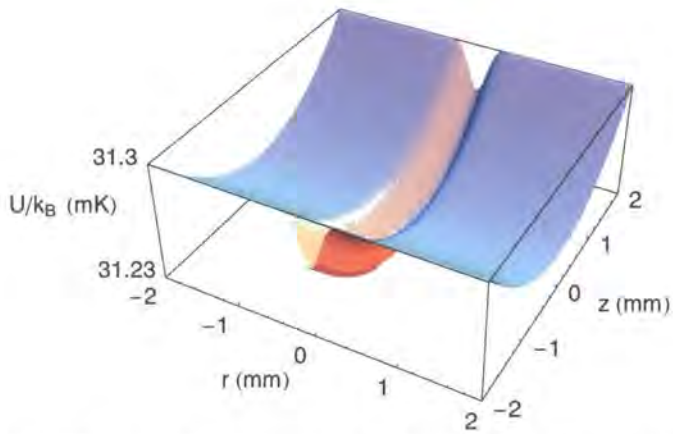

Figure 6.8: The potential energy surface of the combined laser and axial-only magnetic lens. The lens has a radius of 5 cm and carries a maximum current of $NI = 10,000$ Amps. The B_1 term has been subtracted to show the focusing properties of the lens.

The quality of the focus was investigated, and Figure 6.9 plots the change in axial standard deviation, σ_z/σ_{z_i}, against time for different values of λ. There is no $\lambda = 0.7$ line for the decelerating lens due to the reason explained in Section 5.2.1. The lens timings and launch velocity were chosen so that the cloud's apex had a height of 22 cm. Neither lens causes atoms to be lost from the laser guide as a result of the magnetic pulse. For both decelerating and accelerating 5 cm lenses the minimum cloud size is achieved for $\lambda = 0.5$, resulting in a change in axial standard deviation of 1.18 and 1.64 respectively. If the lenses were free of aberrations, one would expect to see no change in axial size at the focus (i.e. $\sigma_z/\sigma_{z_i} = 1$). An unfocused cloud's axial size would have increased by a factor of 34 and 59 respectively. The aberrations of the axial-only lens inhibit achieving a compressed image and also cause the focusing to occur ~ 10 ms after the predicted focal times. The focusing performance in contrast with the 1D focusing of Section 6.2.2 is significantly worse.

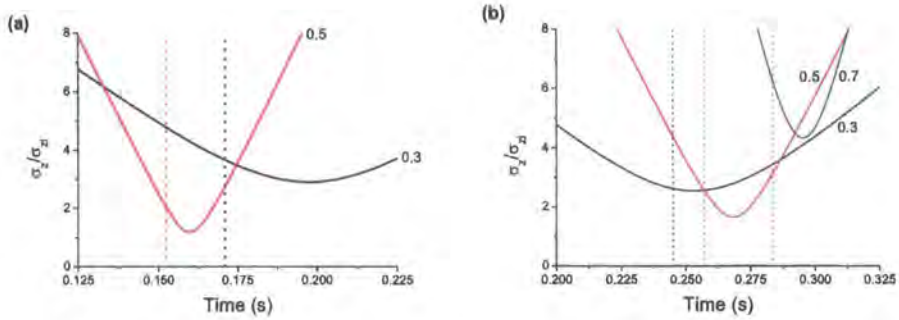

Figure 6.9: The change in axial cloud standard deviation, σ_z/σ_{z_i}, is plotted against time for (a) a decelerating and (b) an accelerating 5 cm radius axial-only lens. Three lens positions are plotted: $\lambda = 0.3$ (black line), 0.5 (red line) and 0.7 (blue). The radial confinement was provided by a 19 W laser guide with a beam waist of 250 μm. The vertical lines indicate the predicted focus times - the colours matching the corresponding line.

6.3.2 Strategies II-III: axial/radial focusing

The effect of significant aberrations and the complication of the constant acceleration for axial-only lenses are undesired. These can be avoided by using either the Strategy II or Strategy III lenses described in Section 4.4.2. The drawback with such lenses is that the radial direction is now also perturbed. The choice of which lens to use depends on whether the atoms are strong-field or weak-field seeking, namely Strategy II and III respectively. The combined potential resulting from the magnetic and laser fields is shown in Figure 6.10 (a) for a Strategy III lens. At the centre, the optical dipole potential dominates and there is positive curvature causing focusing in all three spatial directions. However, away from the z-axis the magnetic potential becomes significant and the radial curvature turns negative. This turn over is shown more clearly in the $z = 0$ cross section in Figure 6.10 (b). The trap depth has been reduced, which means some atoms will have become energetically unbound during the lens pulse, see eqn. (3.6).

In Figure 6.11 the trajectories of 25 atoms are plotted in the centre of mass frame for (a) the radial direction and (b) the axial direction. In this example a 5 cm Strategy III lens was positioned at $\lambda = 0.5$ and was pulsed on for 5.5 ms to bring the cloud to a focus at the fountain apex. In this simulation two atoms were lost as a result of the magnetic lens pulse. Before investigating the quality of the focused cloud, attention is turned to characterising these pulse losses.

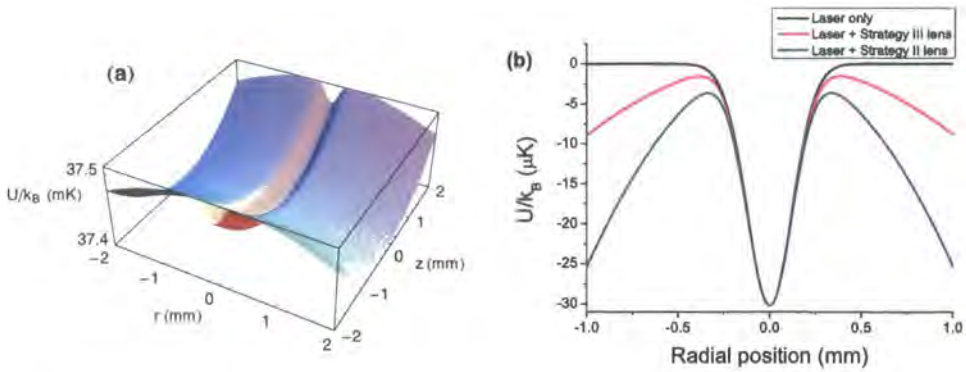

Figure 6.10: Plot (a): The potential energy surface of the combined laser and magnetic fields for a Strategy III lens is plotted against radial and axial position. The 19 W laser has a beam waist of 250 μm. The lens has a radius of 5 cm and has $NI = 10,000$ Amps in the coils. In (b) the cross section along the $z = 0$ line is plotted. The black line is the laser only potential, the blue line is the combined laser and magnetic potential for a Strategy II lens and the red line is the combined potential for a Strategy III lens. For a Strategy II (Strategy III) lens the trap depth is 88% (95%) of the laser depth. Note: the combined potentials have offsets added so that the three minima coincide.

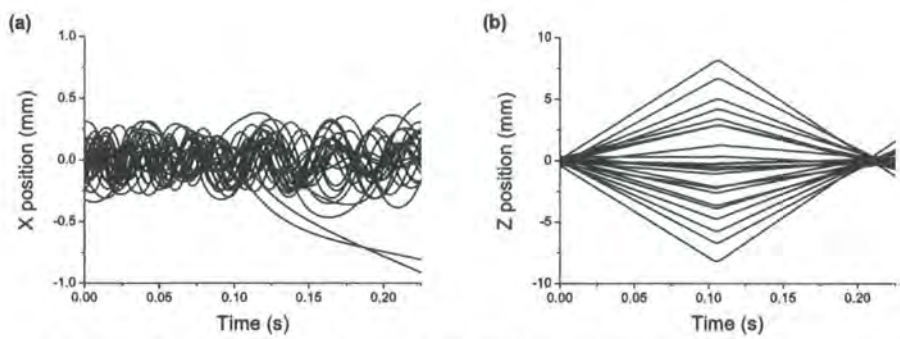

Figure 6.11: The trajectories of 25 WFS atoms are simulated passing through the laser guide and being focused by a 5 cm radius Strategy III lens. The pulse occurs at $\lambda = 0.5$ and has a duration of 5.5 ms. Plot (a) shows the x-axis position and plot (b) the z-axis position relative to the cloud's centre of mass.

If an atom's velocity was not modified, the 'window of opportunity' to escape only lasts as long as the pulse time, which is usually of the order of a few milliseconds. This escape time is short compared to the radial oscillation period within the laser guide. The period is obtained from eqn. (3.5): $T_{\rm osc} = 2\pi/\omega_{r_{\rm L}}$. For a 19 W laser with $1/e^2$ radius of 250 μm this corresponds to a period of 14 ms. Therefore an individual atom will only perform $\sim 1/10^{\rm th}$ of an oscillation and is unlikely to escape. One would expect the loss due to this mechanism to scale with the pulse duration τ.

However, the magnetic pulse modifies the velocity of the atoms. For some atoms this can result in them becoming energetically unbound both during and after the pulse. Over time these unbound atoms will escape from the guide. The immediate change in bound fraction and its subsequent effect on the guided atoms are illustrated in Figures 6.12 (a) and (b) respectively. The initial overshoot in the bound fraction demonstrates the losses due to a lowered potential described above. The momentum kick an atom receives for a given λ is independent of the lens design. Therefore one would expect to find that the lens design has a negligible effect on the loss due to the pulse; this is verified by comparing the red and blue lines in Figure 6.12. The loss due to the magnetic pulse is $\sim$ 2%, and is tiny compared with the loss associated with the initial loading of the laser guide.

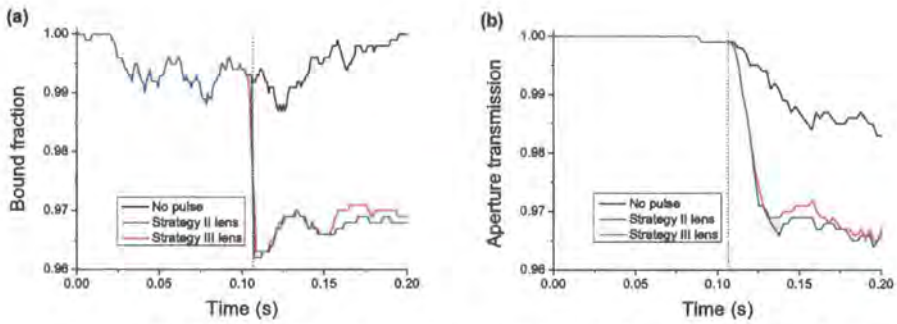

Figure 6.12: Plot (a) shows the evolution of the ratio of bound atoms to the initial number of bound atoms. Three cases are plotted: no magnetic pulse (black line), a Strategy II lens for SFS atoms (blue line) and a Strategy III lens for WFS atoms (red line). The lens pulse occurs at $\lambda = 0.5$. Plot (b) is identical to (a) except for the y-axis now represents the atom transmission through a 0.5 mm radius aperture. Only atoms that were initially bound were considered when calculating the transmission. Both Strategy II and Strategy III lines trace each other remarkably well which is an indication that pulse loss is independent of the lens design. The simulation was performed with 5,000 atoms.

Attention is now returned to studying the focusing properties of the magnetic lenses. For small radius lenses, aberrations tend to dominate resulting in a poor focus and unpredictable focus time. When the lens radius is increased above 7 cm for a Strategy II lens and above 5 cm for a Strategy III lens, no further improvements are observed. The Strategy II lens suffers from worse aberrations as the atoms experience more of the anharmonic B-field due to their closer proximity to the coils.

In Figure 6.13 the change in axial standard deviation, σ_z/σ_{z_i}, for a 5 cm Strategy III lens is plotted against time for different values of λ. The effect of aberrations is significantly less for this design compared with an axial-only lens (Figure 6.9). The minima occur within ~ 3 ms of the predicted focal time and are only slightly worse than values achievable with an aberration-free lens. For the case of $\lambda = 0.7$ the cloud is compressed along the axial direction to half of its initial size. Unlike Section 6.2.2 where aberrations dominate a similar plot at high λ, one finds that for laser guided atoms this is not the case. This is due to the strong radial confinement provided by the laser guide.

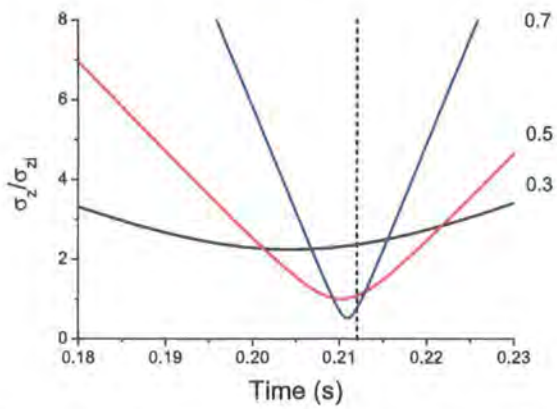

Figure 6.13: The change in the cloud's axial standard deviation, σ_z/σ_{z_i}, is plotted against time for a Strategy III lens. Three lens positions are plotted: $\lambda = 0.3$ (black line), 0.5 (red line) and 0.7 (blue), the minimum change is 2.2, 1.0 and 0.5 respectively. The expected minima based upon the magnification $(\lambda - 1)/\lambda$ are 2.33, 1.00 and 0.43 respectively. The dashed vertical line indicates the predicted focal time of 212 ms.

6.3.3 Transported cloud properties

Numerical simulations were performed to compare the four hybrid transportation schemes. The position and velocity standard deviations of the atomic cloud were computed after tracing the trajectories of individual atoms. The results are presented in Table 6.2. For ease of comparison the equivalent temperature, $\mathcal{T}$, corresponding to a given velocity and the cloud aspect ratio, $\xi = \sigma_z/\sigma_r$, are also tabulated. It should be noted that when the cloud is trapped in the upper chamber, the temperature will rethermalise via collisions. The trap geometry will determine the rethermalised temperature.

	MOT	Bound atoms	Apex	$-a_0$ axial only lens	$+a_0$ axial only lens	Strategy II lens	Strategy III lens
σ_x (mm)	0.20	0.11	0.19	0.19	0.19	0.22	0.21
σ_z (mm)	0.20	0.20	9.4	0.37	0.66	0.22	0.21
$\xi = \sigma_z/\sigma_r$	1.00	1.81	50	1.96	3.57	1.03	0.99
σ_{vx} (cm/s)	4.42	2.53	1.67	1.63	1.68	1.71	1.71
σ_{vz} (cm/s)	4.42	4.41	4.40	3.93	4.03	4.42	4.47
$\mathcal{T}_x$ (μK)	20	7	3	3	3	3	3
$\mathcal{T}_z$ (μK)	20	20	20	16	17	20	20

Table 6.2: The table records the change in the atomic cloud's properties (position standard deviation σ, aspect ratio ξ, velocity standard deviation σ_v and temperature $\mathcal{T}$) for different transportation schemes. The columns are as follows: the initial cloud properties generated in the MOT; the cloud loaded from the MOT into a 250 μm beam waist laser guide; a cloud that has been transported within the laser guide to the 22 cm apex; a guided cloud that has been focused by a decelerating axial-only lens; a guided cloud that has been focused by an accelerating axial-only lens; a guided cloud that has been axially focused by a Strategy II lens; a guided cloud that has been axially focused by a Strategy III lens. Each lens has a radius of 5 cm, a maximum current of $NI = 10,000$ Amps and is pulsed on at $\lambda = 0.5$, see Table 6.1.

The first column of the table shows the properties of the initial MOT. The second gives the properties of atoms that are loaded into the guide. As expected these have a smaller radial extent, and as only the least energetic are loaded, a lower radial temperature. For the launched atoms with only laser guiding (third column) there is a slight increase in the radial size as a consequence of the laser beam diffracting, and the axial size grows by more than an order of magnitude. The cloud has a very elongated sausage shape ($\xi >> 1$). Focusing the laser guided cloud with either a decelerating or an accelerating axial-only lens (columns four and five respectively) produces a radial extent similar to an unfocused laser guided cloud, however the axial extent is significantly smaller than with no magnetic lens, but not as compact as the original launched cloud. This is a consequence of the aberrations associated with this lens design. The last two columns characterise the performance of optimised Strategy II and Strategy III lenses. Although there is a slight atom loss during the impulse associated with the negative radial curvature, the performance of these lenses is far superior, yielding moderately larger radial clouds, and one-to-one axial imaging. In all cases the slight increase of the radial extent is accompanied by a concomitant reduction of the radial temperature, a manifestation of Liouville's theorem.

Whilst initially it appears as if axial-only lenses would complement the radial laser guiding, the results of the simulations shows that the best strategy would be to use optimised harmonic lenses. The axial-only lens is harder to realise experimentally, and, as a consequence of the broken axial symmetry, has more significant aberrations. However, it can be used without further atom loss during the magnetic impulse. By contrast the optimised harmonic lenses do suffer a slight atom loss during the pulse. However this is insignificant compared to the initial loading loss. The axial-focusing of these two lenses is superior, and the simulations show that for realistic experimental parameters better than one-to-one axial focusing can be achieved when $\lambda > 0.5$.

There is a slight broadening of the cloud radially, arising from the laser beam's increased width. It might be possible to circumvent this by 'zooming' a lens such that the centre of mass of the atom cloud is always confined by the tightest focus of the beam. This would keep the initial cloud confined to the same final radial width. However this would be at the expense of significant experimental complexity.

6.4 Double-impulse magnetic focusing

This section compares the alternate-gradient numerical simulations with the purely harmonic lens calculations in Section 5.3. The (τ_1, τ_2) sample co-ordinates illustrated in Figures 5.5 (b) and (c) are used, in order to run numerical simulations for the relative density increases illustrated in Figure 6.14. The simulation has not (cf. Figure 6.7) used the rms volume of the cloud to represent the relative density increases as these result in extremely low relative density increases (typically 10^{-5} in (a) and 10^{-3} in (b)) that would reduce the figure's contrast.

For both strategies the numerical simulations trace the shape of the analytical relative density increase although aberrations result in reduced increases. The maximum relative density increases in (a) and (b) are 186 and 50 respectively. This is a marked improvement on the single-impulse focusing, however the cloud distribution is no longer isotropic. The harmonic focus aspect ratio has a range $12 \leq \xi \leq 17$ in (a) and $0.074 \leq \xi \leq 0.095$ in (b).

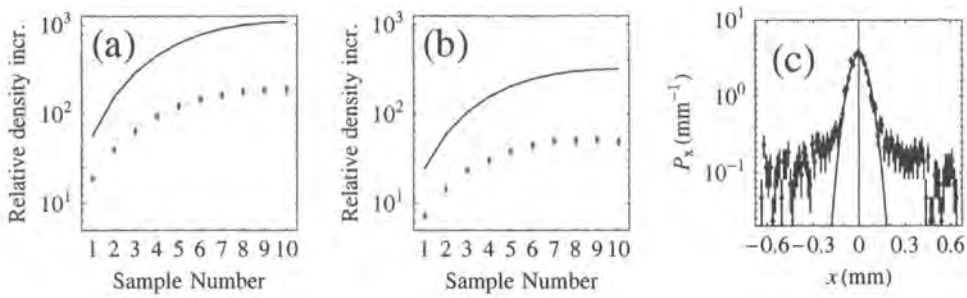

Figure 6.14: Images (a) and (b) use the (τ_1, τ_2) co-ordinates illustrated in Figure 5.5 (b) and (c) to show the relative density increase for alternate-gradient lensing Strategies AR and RA, respectively. There were 1,000 atoms in the simulation and relative density increases are shown for a pure harmonic lens (black curve), as well as the relative density increase for the fraction of atoms in a realistic lens arriving at the harmonic focus region (blue dots with error bars). In image (c) the strong spatial bimodal nature of the x focus for the leftmost point in (a) is clearly seen on a log scale. The Gaussian fit (with $\sigma_x = 56\,\mu$m) contains 49% of the 3,000 simulated atoms used in (c). [Figure generated in collaboration with A. S. Arnold.]

In certain applications, for example microtrap loading and lithography, the sausage-shaped distribution ($\xi > 1$) with its reduced radial spread could be beneficial. Figure 6.14 (c) plots the distribution of a cloud focused via Strategy AR. The standard deviations for the Gaussian fits to the core of the x, y, and z distributions are $56\,\mu$m, $56\,\mu$m and $850\,\mu$m; an order of magnitude reduction in the radial direction compared with single-impulse focusing.

6.4.1 Transported cloud properties

For many experiments it is also important to consider changes to the velocity distribution and hence the collision rate and phase-space density. Unless the collision rate of a gas is sufficiently high, then Bose-Einstein condensation via sustainable evaporative cooling is impossible. Changes in the collision rate and phase-space density of the focused cloud are complicated by the fact that alternate-gradient lensing automatically leads to an anisotropic focused distribution both in space *and* in velocity.

At the $\mathcal{B}_{r,z} = 0$ focus of the cloud the $\mathcal{ABCD}_{r,z}$ matrix has radial and axial spatial widths $\sigma_r = \mathcal{A}_r\sigma_R$ and $\sigma_z = \mathcal{A}_z\sigma_R$ respectively. The radial and axial velocity widths are given by:

$$\sigma_{v_{r,z}} = \sqrt{k_B\mathcal{T}_{r,z}/m} = \sqrt{\mathcal{C}_{r,z}{}^2\sigma_R{}^2 + \sigma_V{}^2/\mathcal{A}_{r,z}{}^2}\,, \tag{6.2}$$

where $\mathcal{T}_{r,z}$ is the atomic cloud temperature. In the limit $\mathcal{C}_{r,z}\sigma_R \ll \sigma_V/\mathcal{A}_{r,z}$, the velocity width of the focused cloud is inversely proportional to its spatial width and $\sigma_{v_{r,z}} = \sigma_V/\mathcal{A}_{r,z}$. In Figure 6.15 phase-space plots of the AR and RA strategies from the rightmost points of Figures 6.14 (a) and (b) were generated with a 30,000 atom simulation. The effect of aberration is clearly seen when comparing the purely harmonic lenses (subscript H) and the Monte Carlo simulation with the full magnetic fields from realistic coils (subscript MC). The plots also demonstrate the inversely proportional relationship between spatial and velocity widths. Furthermore, in the Monte Carlo simulations there is much stronger correlation between position and velocity.

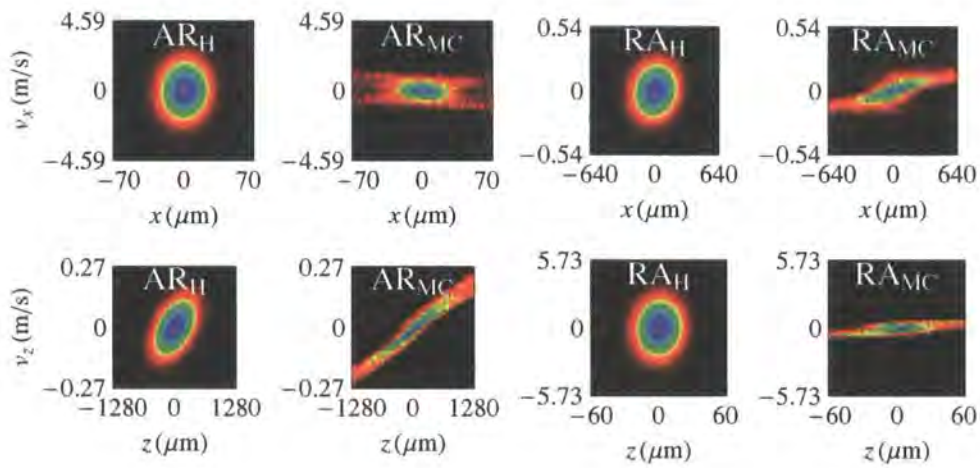

Figure 6.15: Phase-space plots of the AR and RA strategies from the rightmost points of Figures 6.14 (a) and (b) respectively. Both a harmonic lens calculation (subscript H) and a Monte Carlo simulation with the full magnetic fields from realistic coils (subscript MC) are plotted. In the $\mathrm{AR_{MC}}$ plot there are 45% $(x - v_x)$ and 42% $(z - v_z)$ of the initial 30,000 atoms present. In the $\mathrm{RA_{MC}}$ plot there are 61% $(x - v_x)$ and 24% $(z - v_z)$ of the atoms present. The effects of aberration are clearly seen when comparing the harmonic and realistic magnetic coils. [Figure generated in collaboration with A. S. Arnold.]

The anisotropic temperature in the focused cloud means that captured atoms in a cylindrically symmetric harmonic trap with radial and axial angular frequencies ω_r' and ω_z', will rethermalise to an isotropic temperature via elastic collisions. The prime is used to distinguish the trap frequencies from that of the lens. The total (potential+kinetic) energy of the focused cloud is equated with that of a 3D harmonic oscillator at equilibrium temperature $\mathcal{T}$ (i.e. $\frac{1}{2}k_B\mathcal{T}$ average energy per atom for each space and velocity dimension). The equilibrium temperature of the focused cloud after thermalisation is thus:

$$\mathcal{T} = \frac{m}{6k_B}\left(2\omega_r'^2\sigma_r^2 + \omega_z'^2\sigma_z^2 + 2\sigma_{v_r}^2 + \sigma_{v_z}^2\right). \tag{6.3}$$

In many experiments other physical properties of the atomic cloud are of interest: the atomic density $n \propto 1/(\sigma_r^2\sigma_z)$, collision rate $\Gamma_{\rm el} \propto n\sqrt{\mathcal{T}}$ and phase-space density PSD $\propto n/(\mathcal{T}_r\mathcal{T}_z^{1/2})$. In order to minimise the loss of phase-space density during thermalisation of the focused cloud, it can be shown that it is best to choose ω_r' and ω_z' such that the potential energy is equal in all spatial dimensions and the total potential energy is equal to the total kinetic energy of the cloud [154]. The physical properties of the focused atomic clouds of Figure 6.15 are displayed in Table 6.3. The relative values for the density n, collision rate $\Gamma_{\rm el}$ and phase-space density can be converted into absolute values using typical initial experimental values: $\langle n\rangle = 10^{10}\,{\rm cm}^{-3}$ (an atom number $N = 3\times10^7$ in the unfocused cloud), $\Gamma_{\rm el} = 3\,{\rm s}^{-1}$ (see Appendix E) and phase-space density PSD=2×10^{-6}.

Note that the Monte Carlo relative density increases in Table 6.3 are lower than those in Figure 6.14 by a factor of ≈ 2, but the fraction of atoms in the focus are higher by a factor of ≈ 2. In Figure 6.14 the density is estimated by measuring the fraction of atoms arriving at the harmonic focus. Here, a 6-dimensional Gaussian phase-space fit to the narrow central peak of the bimodal focus was made to explicitly obtain σ_r, σ_z, $\mathcal{T}_r$ and $\mathcal{T}_z$. The fraction of atoms in this Gaussian focus was used for $\mathcal{F}$ here.

An interesting result of Table 6.3 is that the aberrations of 'real' lenses work to one's advantage, to some extent, in that the atoms can be loaded into a trap with a shallower depth than atoms focused by a purely harmonic lens, and phase-space density loss is reduced during rethermalisation. This is due to the

	t	$\mathcal{F}$	$\sigma_{r,z}(\mu\text{m})$	$\mathcal{T}_{r,z}(\mu\text{K})$	$\omega'_{r,z}/2\pi$ (Hz)	n	Γ_{el}	PSD
AR_{H}	0	1	400, 400	20, 20	*17.4, 17.4*	1	1	1
	T	1	15.2, 257	13900, 60.9	*12000, 47.3*	1080	23200	0.892
	T_R	1	15.2, 257	9260, 9260	9850, 584	1080	23200	0.108
AR_{MC}	0	1.000	400, 400	20, 20	*17.4, 17.4*	1	1	1
	T	0.308	23, 500	2720, 57	*3530, 23.5*	74.5	713	0.325
	T_R	0.308	23, 500	1830, 1830	2900, 133	74.5	713	0.085
RA_{H}	0	1	400, 400	20, 20	*17.4, 17.4*	1	1	1
	T	1	128, 12.2	197, 21600	*170, 18700*	319	6110	0.988
	T_R	1	128, 12.2	7320, 7320	1040, 10900	319	6110	0.046
RA_{MC}	0	1.000	400, 400	20, 20	*17.4, 17.4*	1	1	1
	T	0.305	200, 20	105, 1670	*79.7, 3180*	24.4	137	0.509
	T_R	0.305	200, 20	627, 627	195, 1950	24.4	137	0.139

Table 6.3: Physical properties of the two different alternate-gradient strategies modelled, AR and RA from the rightmost points in Figs. 6.14 (a) and (b) respectively. Subscripts H and MC respectively denote a simulation with purely harmonic lenses and a Monte Carlo simulation with the full magnetic fields from realistic lens coils. The measured parameters are: fraction of atoms in the Gaussian focus $\mathcal{F}$ (see text), radial/axial cloud radius $\sigma_{r,z}$, radial/axial temperature $\mathcal{T}_{r,z}$, radial/axial trap frequency $\omega'_{r,z}$, relative density n, relative collision rate Γ_{el} and relative phase space density PSD. The effective trap frequencies for the initial ($t = 0$) and focused ($t = T$) cloud (italicised) are equilibrium values based on $\omega' = \frac{1}{\sigma}\sqrt{k_B T/m} = \sigma_v/\sigma$. The actual frequencies of the trap the atoms are loaded into at $t = T$ are denoted in the $t = T_R$ lines (the cloud properties after T plus the thermalisation time).

reduced anisotropy of the spatial and velocity distributions at the focus. The focused atoms have a relatively high temperature and one needs a trap depth of $\approx 10\,\text{mK}$ to trap the focused atoms.

If the trap that is being loaded is harmonic, with a large capture volume, then the rms size of the cloud will be linked to the equilibrium temperature after elastic collisions rethermalise the initially bimodal image distribution. In order to keep the high density core of the atomic cloud, the high energy atoms must be removed on a time scale that is rapid compared to rethermalisation - this could be achieved with strong RF evaporative cooling or by shining resonant dark SPOT beams [160] at the focal region. A trap with a small capture volume, e.g. an atom chip [110, 111] or a focused optical dipole beam trap [87], is ideal as only the high density core of atoms will be captured in the trap.

Chapter 6 summary

- A Strategy I lens can be used to focus an atomic cloud in the radial direction. Aberrations are reduced by increasing the size of lens. There is a marked difference in performance when comparing real coils with their parabolic approximations and the predictions made using $\mathcal{ABCD}$-matrices.
- The optimised double coil lenses (Strategies II and III) out perform the single coil lens.
- The only viable strategy for producing single-impulse isotropic 3D focusing is the baseball lens (Strategy VI).
- The combination of a laser guide and magnetic lenses makes a good transport scheme. The lack of losses from the axial-only lens (Strategy IV) is outweighed by the convenience and better harmonicity of the axial focusing/radial defocusing lenses (Strategies II and III). Pulse losses from the latter are 2% for the lenses simulated.
- The alternate-gradient method to focus an atomic cloud produces a highly focused core making it an ideal method for loading microtraps. The rethermalisation temperature and phase space density changes for harmonic trap loading were calculated.

Chapter 7

Optical lattices and experiment design

"Every contrivance of man, every tool, every instrument, every utensil, every article designed for use, of each and every kind, evolved from a very simple beginning." Robert Collier

Having studied magnetic manipulation, attention is returned to optical manipulation and the second aim of the thesis. The goal of which is to load cold atoms into a 3D optical lattice for use in quantum information processing (QIP) experiments. An optical lattice is a periodic array of potential minima created by the interference of laser beams. Cold atoms can be loaded into these minima, and what results is a periodic array of sites containing a miniature cold atom cloud. Manipulation of single-sites has been experimentally demonstrated in a 1D CO_2 laser lattice [93, 94]. To achieve QIP requires high oscillation frequencies in all directions to avoid decoherence; a strong motivation to move to three dimensions.

This chapter introduces optical lattices and describes the creation of a face-centred cubic lattice made from CO_2 laser beams. From this, design criteria for an experiment are outlined. In the proceeding chapters the construction, operation and optimisation of the cold atom experiment is described. Work presented in these chapters has been done in collaboration with C. S. Adams and K. J. Weatherill.

7.1 Optical lattices

It is imperative to take the light's polarisation into account when calculating the dipole force introduced in Chapter 2. The first reason is that the individual laser beam's electric fields must be added as vectors. The resulting total electric field vector can then be used to calculate the intensity, $I(\mathbf{r}) = \epsilon_0 c|\mathbf{E}|^2/2$; a scalar quantity. The second reason is the polarisation affects the allowed atomic transitions. For example, in Chapter 2 the Q-matrix was given for an electric field aligned along the quantisation axis. The calculation of the excited state polarisability is more complicated for multiple laser beams.

Although linked, it is possible to construct lattices that have just a spatial variation of either the polarisation or intensity. A simple example of the former is the interference pattern resulting from two counter-propagating laser beams that have orthogonal linear polarisation (lin$\perp$lin). For a thorough discussion of this scheme and its use in sub-Doppler cooling see refs. [105, 127].

This thesis will concentrate on lattices created by the spatial variation of intensity. The simplest example is two counter-propagating laser beams that have parallel linear polarisation (lin$||$ lin). Figure 7.1 shows the standing wave interference pattern of two focused CO_2 laser beams. Each lattice site is separated by half the wavelength of the laser light. This illustrates a major advantage of using a CO_2 laser as the large wavelength ($\lambda_T = 10.6$ μm) makes it possible to resolve optically individual lattice sites.

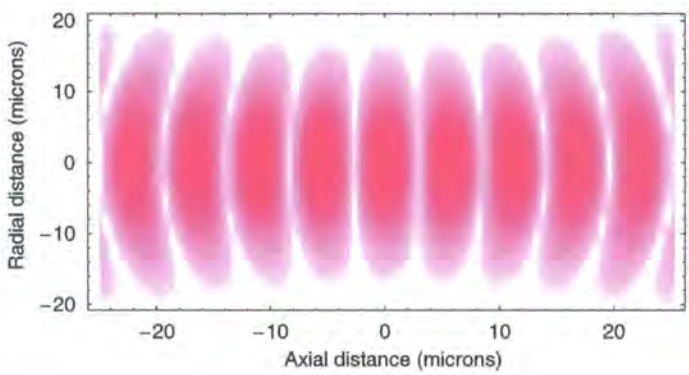

Figure 7.1: The contour plot shows the potential minima generated from the interefernce of two counter-propagating laser beams that have parallel linear polarisation. The 10 μm beam waist used in the simulation highlights diffraction's influence.

The standing wave can be turned into an optical conveyor belt. If there is a small frequency difference, δ, between the two laser beams, the position of the potential wells will move in time (with velocity $v = \delta/k$, where k is the wavevector of the laser). In practise this could be implemented with an acousto-optical modulator (AOM). A second method is to vary the phase of one of the beams, which could be implemented using technology based upon a liquid crystal device (LCD).

Lattices more exotic than the 1D standing wave can be created by the interference of multiple laser beams, see [161] for the crystallography of optical lattices. A N-dimensional lattice requires a minimum of $N + 1$ laser beams. One problem with the topography of lattices is that they can be changed by fluctuations in the phase of the individual laser beams. Certain geometries with exactly $N + 1$ beams have phase independent topography, as outlined in [161], whereby any phase change just results in a translation of the lattice sites. Adams *et al.* showed how to create a face-centred cubic lattice that is phase independent [162]. It is this design that we plan to use to trap Rb atoms. Figure 7.2 shows a diagram of the laser geometry.

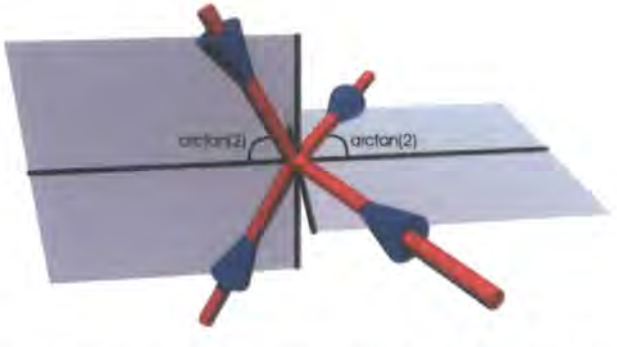

Figure 7.2: A face-centred cubic lattice is created if the laser beams are at an angle of arctan(2) degrees from the common plane axis, and the polarisations are linear and in the plane. The six MOT beams are the thin black lines.

A pair of laser beams propagate in a plane, and a further two lasers are counter-propagating with respect to the first pair in a plane orthogonal to the first. All beams are at angle of arctan(2) $\approx 63.43°$ to the common plane axis. The foci of all four beams overlap at the centre of the co-ordinate system. Furthermore, all beams are linearly polarised in the plane of propagation. The arrangement outlined has the added advantage that it fits in well with MOT cooling beams along the Cartesian axes.

Calculations of the resulting dipole potential have been performed based on CO_2 laser beams being focused to a beam waist of 50 μm. The dipole potential has been scaled in units of the potential well depth of a single Gaussian beam (For 65 W of laser power: $U_{\mathrm{Dip}}(0)/k_{\mathrm{B}} = 1.2$ mK). Figure 7.3 shows a 1D slice through the lattice. The interference pattern is evident in the overall Gaussian profile of the laser beam. The trap depth is 12.8 times greater than that of a single focused Gaussian beam. The lattice constant is: $\lambda_{\mathrm{T}}/\sin(\arctan(2)) = \lambda_{\mathrm{T}}\sqrt{5}/2 = 11.85$ μm. Figure 7.4 shows the interference pattern in the $z = 0$ plane of the lattice. The face-centred cubic structure is evident. It is expected that it will be possible to create ~ 1000 lattice sites loaded with cold atoms.

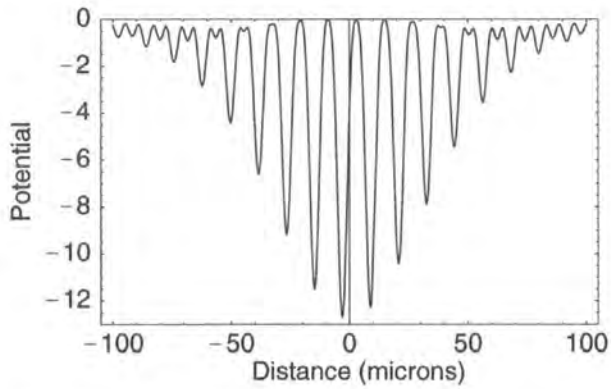

Figure 7.3: A 1D slice through the centre of the four beam interference pattern. The dipole potential has been scaled in units of the potential well depth of a single Gaussian beam. In this simulation the beam waist of the lasers is 50 μm.

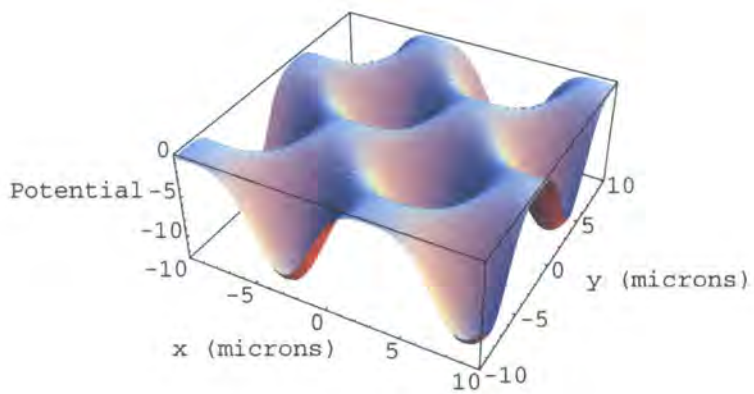

Figure 7.4: The potential energy surface along the z=0 plane of the four beam interference pattern. The face-centred cubic structure is evident. The dipole potential has been scaled in units of the potential well depth of a single Gaussian beam. In this simulation the beam waist of the lasers is 50 μm.

7.1.1 Single-site addressability

Once the atoms have been loaded into the periodic array, a technique is needed to address individual lattice sites. A single laser beam can be used to probe a line of atoms held in a 3D lattice. To probe just one site requires two crossed laser beams, centred on the site of interest, see Figure 7.5. This has the added advantage that the lasers can be used to perform two-photon stimulated Raman transitions. The transfer of atoms in just one lattice site to a different hyperfine ground state has the effect of "marking" them for subsequent operations.

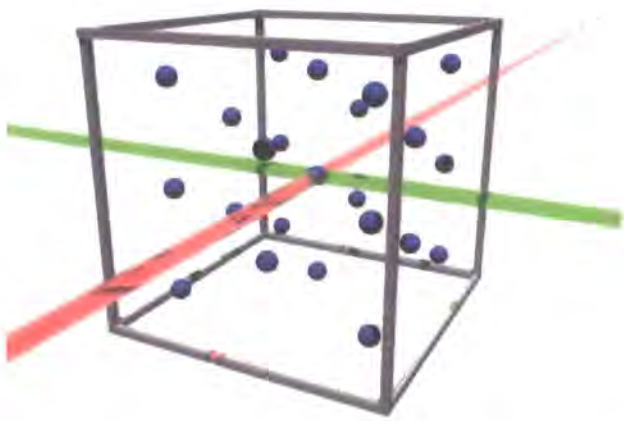

Figure 7.5: The principle of using two laser beams to select a single site in a 3D optical lattice is illustrated.

In theory it is possible to construct state-selective optical tweezers to move the contents of the marked site. An optical tweezer can be constructed from a highly focused laser beam, which acts as a moveable dipole trap. It is made to be state-selective by ensuring that the light shifts of the unmarked sites exactly cancel. A more controlled method of transport would be to use an optical conveyor belt to move one qubit state without disturbing the other state.

7.2 Experiment: design criteria

To construct a 3D lattice experiment requires the vacuum chamber to have three main features:

- Extremely low background pressure to reduce collisions with background gas that result in decoherence.
- Good optical access. The CO_2 laser needs to enter and exit the chamber 8 times, and a further 6 windows are needed for the cooling beams. Extra ports will be needed for probing and imaging the cold atoms. An added complication is the CO_2 laser requires the use of window material that will not be shattered by the high powers. ZnSe is a material that meets this requirement.
- A method to align the CO_2 laser safely and accurately to the required angles. Ideally the laser should be incident normally to the window, to avoid dangerous off-axis reflections.

With these criteria in mind, a differentially pumped two chamber vacuum system was constructed. The first chamber operates at a higher pressure and cools the Rubidium atoms. These atoms are then moved to the second lower pressure chamber. The custom designed chamber has 22 viewports which are machined at the required angles to make the optical lattice. By aligning the CO_2 laser to the window centres simplifies what could be a difficult setup. The next chapter describes in detail the construction of the experiment.

Chapter 7 summary

- Optical lattices were introduced and the importance of including polarisation was explained. The 4 beam geometry for constructing a face-centred cubic lattice was presented along with slices through the potential surface. Techniques for addressing single-sites in the lattice were outlined.
- Design criteria for building a 3D lattice experiment were given.

Chapter 8

Experiment construction

"The shortest distance between two points is under construction."
Noelie Altito

This chapter will describe the construction of a 3D quasi-electrostatic lattice for ^{85}Rb. The main steps involved in completing the experimental aim are:

1. Produce cold atoms in a pyramid magneto optical trap (P-MOT).
2. Transfer atoms to a second chamber.
3. Hold the atoms in a Ultra High Vacuum science MOT (S-MOT).
4. Load atoms into an optical lattice.
5. Image the individual sites in the lattice.

At the time of submitting this thesis, the first three steps have been accomplished. A power supply failure within the CO_2 laser system at the start of 2006 has hindered achieving a dipole trap.

The experiment, under the supervision of Charles Adams, has been built by myself and Kevin Weatherill. This chapter aims to give a overview of the construction, and is broken down into three main sections: the vacuum chamber and magnetic fields; laser systems; imaging and computer control.

8.1 Vacuum chamber and magnetic fields

As explained in the previous chapter, we have opted to use a differentially pumped dual-chamber vacuum system. The first chamber houses a pyramid magneto optical trap (P-MOT) and operates at a pressure of $\sim 10^{-9}$ Torr. Section 8.1.1 describes the operation of the P-MOT. The cold atoms are moved down to the 'science' chamber which contains a second MOT (S-MOT) and has a much lower pressure ($< 10^{-10}$ Torr). The reduced background collisions allows much longer trap lifetimes. The second chamber has sufficient optical access with the right geometry to create a 3D lattice. Section 8.1.2 describes the operation of the S-MOT. Figures 8.1 and 8.2 are annotated photos of the combined vacuum system shortly after it had been assembled. Full details of the vacuum design and assembly process can be found in ref. [163].

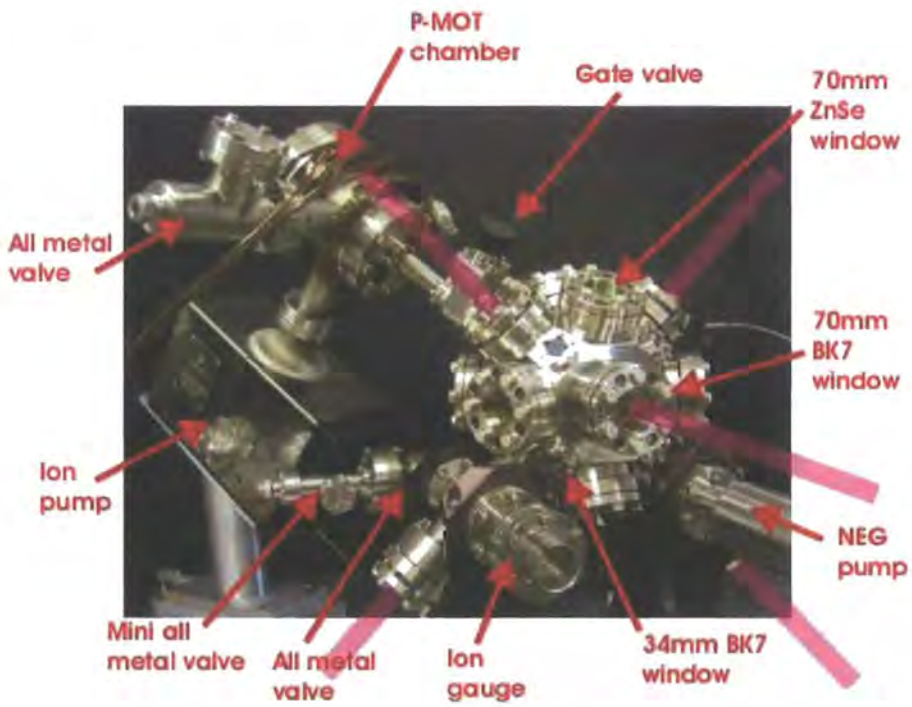

Figure 8.1: Photograph of the assembled vacuum chamber (side view). The orientation of the S-MOT cooling beams are shown in purple.

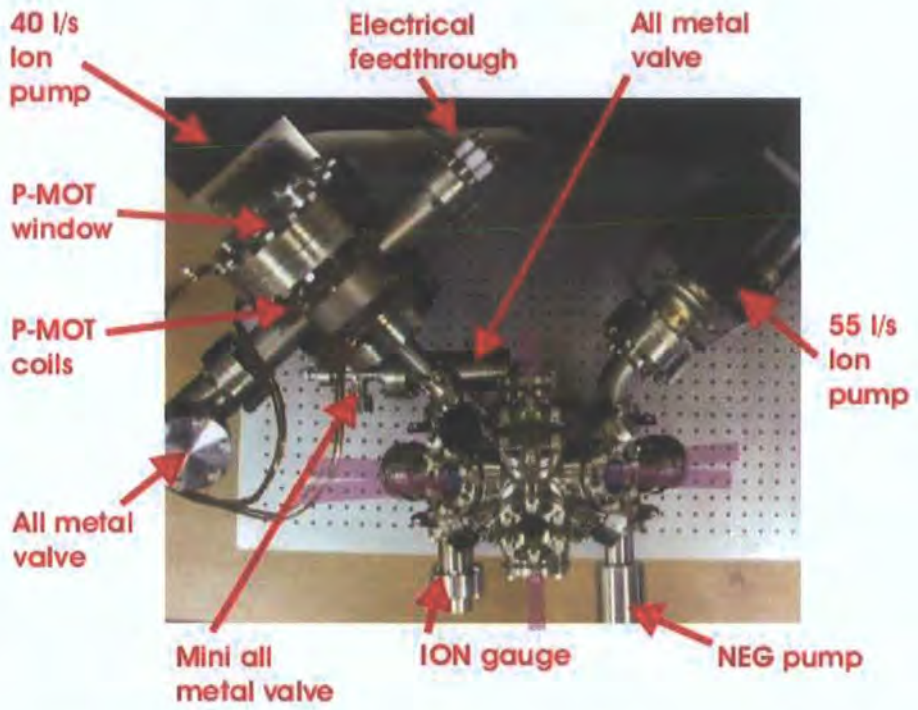

Figure 8.2: Photograph of the assembled vacuum chamber (top view). The orientation of the S-MOT cooling beams are shown in purple.

8.1.1 The pyramid MOT

The pyramid magneto optical trap [164, 165] operates on the same physical principles as a standard MOT described in Section 2.2.1. The optics are aligned in the shape of an inverted pyramid, which produces light traveling in all three Cartesian directions required for laser cooling from a single expanded beam with circular polarisation. See Figure 8.3 for a diagram that illustrates the principle. In practise the pyramid is made from two flat mirrors and two prisms. A 2 mm square hole at the pyramid's apex means that there is no laser beam counter-balancing the downwards beam. Therefore the cold atoms are pushed down through the hole into the second chamber below. Figure 8.4 shows the chamber, surrounding optics and wiring of the P-MOT.

The frequency stabilised cooling and repumping light is sent to the P-MOT through a polarisation preserving fibre optic cable (Oz Optics). No collimating lens is used on the fibre output, and the beam is allowed to expand before being collimated by a 2", $f = 250$ mm lens. A $\lambda/4$ waveplate (CVI Technical Optics)

is used to convert the linearly polarised light into circular polarisation. The procedure for setting the correct waveplate angle and ensuring the fibre optic preserves the linear polarisation angle is explained in Appendix G.

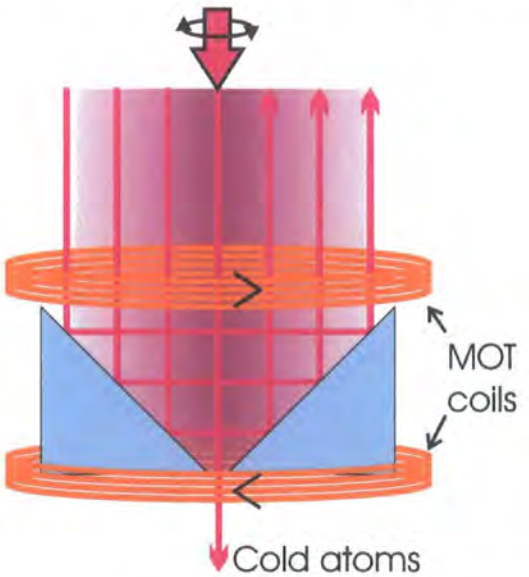

Figure 8.3: The pyramid MOT consists of optics in the shape of an inverted pyramid. The rays indicated in the diagram demonstrate how the required laser beams in all six directions are achieved.

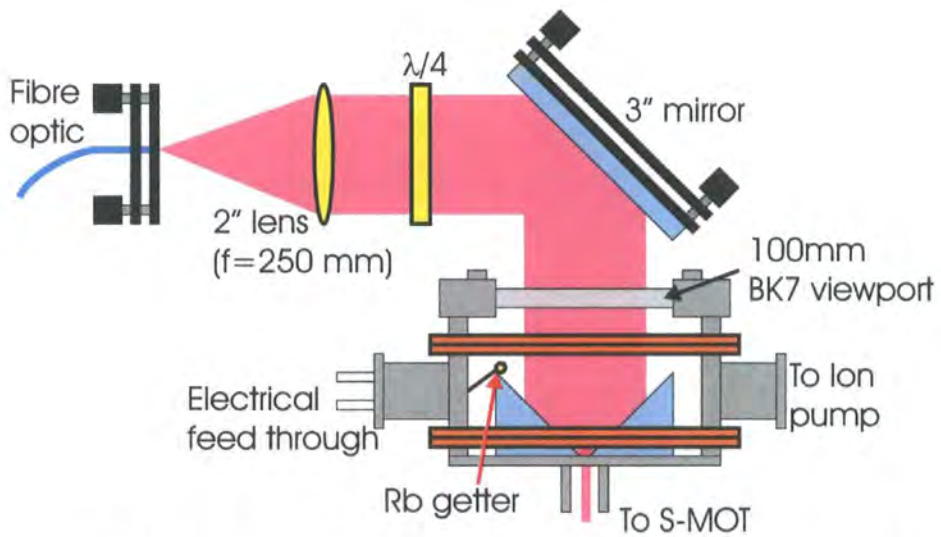

Figure 8.4: The pyramid MOT chamber, surrounding optics and wiring is illustrated. Note, for clarity, the shim coils are not shown.

The Rb atoms are captured and cooled from an atomic vapour created by running current through getter-dispensers (SAES). When heated a chemical reaction between rubidium chromate and a reducing agent releases Rb atoms. Typical currents required to Ohmically heat the dispensers are in the 2.5-4 Amp range.

The quadrupole magnetic field required for the MOT is generated by an anti-Helmholtz coil pair. Each individual coil consists of 20 turns of a hollow Kapton coated copper wire which has a square cross-section with 3.5 mm wide sides. The hollow nature allows the wire to be water cooled. The winding pattern is illustrated in Figure 8.5. The winding was achieved by clamping the unassembled chamber in a lathe, then turning the chamber by hand, the copper wire was wound around the chamber. The insulating Kapton is easily scratched, so great care must be taken that no sharp or rough edges are in contact with the coils. Once wound the coils were further protected by the addition of extra Kapton tape.

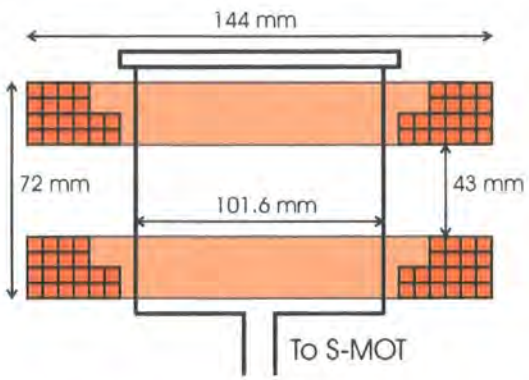

Figure 8.5: The wiring pattern of the anti-Helmholtz coils on the P-MOT vacuum chamber.

The P-MOT typically has 10 Amps of current flowing in the coils, and the Ohmic heating is sufficiently low that water cooling is not required. A model of the magnetic field gives a gradient of 0.52 G A^{-1} cm^{-1}. The current is supplied by a EA-PS 3016-20B power supply (16 V, 20 A) which has the capability of being switched by a TTL signal. The switching on time was measured to be 4 ms with a 1 ms lag, and switching off time of 2 ms with no lag.

In addition to the anti-Helmholtz coils, the chamber also has three shim coils with their axes along each of the Cartesian directions. These are used to move

the position of the magnetic field zero. This is especially useful when dealing with the P-MOT as it allows the cold atom cloud to be positioned above the hole in the pyramid. Each shim coil has a radius of 165 mm, has $\sim$ 50 turns of 1 mm diameter Kapton coated copper wire and typically carries up to 5 Amps. The wire was wound around perspex formers. The currents are supplied by either a TTi EX1810R (18 V, 10 A) or Manson EP-613 (30 V, 2.5 A) DC power supply. A basic field effect transistor (FET) switching circuit was built to allow the shims to be switched on and off by a TTL signal, see Figure 8.6. The switching time, measured by monitoring the the voltage across the source and drain pins, is 0.1 μs.

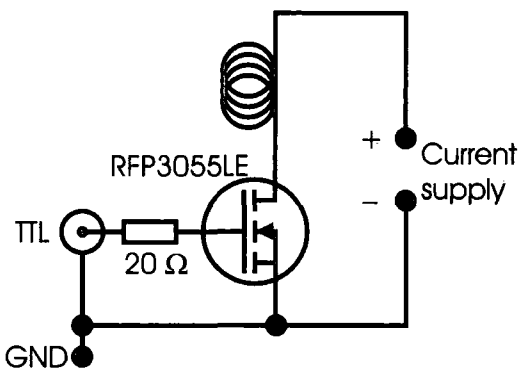

Figure 8.6: The circuit used to switch the individual shim coils on and off using a TTL signal.

The vacuum is maintained by a 40 l/s Ion pump (Varian VacIon Plus Starcell) and this is controlled by a Varian Multivac 929-4000. The controller gives a readout of the pressure within the chamber, and is a useful tool when operating the Rb getters so as not to flood the chamber with Rb. Due to the permanent magnet contained within the Ion pump, a custom 2 mm thick Mu-metal shield was manufactured by Magnetic Shields Limited to completely surround the pump. Mu-metal is a nickel-iron alloy (77% nickel, 15% iron, plus copper and molybdenum) and has a high magnetic permeability which strongly attracts magnetic fields.

8.1.2 The science chamber

The stainless steel (316 LN) chamber is based around an irregular tetra-decahedral shape with twenty two Conflat window ports: fourteen 70 mm outer diameter flanges, and eight 34 mm outer diameter flanges. The chamber was custom engineered by Robert Wiley at the University of Strathclyde. The chamber design is shown in Figure 8.7. Eight ZnSe ports are used for the CO_2 beams, six BK7 ports for the S-MOT beams, one port for the pyramid MOT connection, and seven ports used for imaging, photodiodes and optical manipulation. The fourteen larger ports (CO_2 and S-MOT) have custom made windows based upon solder seal technology [166]. Specific modifications to the design for this experiment are presented in ref. [163]. The smaller viewports all use commercially available BK7 windows that have been anti-reflection coated. After the initial vacuum has been created, see Section 8.1.3, it is maintained by a 55 l/s Ion pump (Varian VacIon Plus Starcell) controlled by a Varian MiniVac 929-0290. A Mu-metal shield surrounds the Ion pump to prevent a large magnetic field gradient being created across the MOT region.

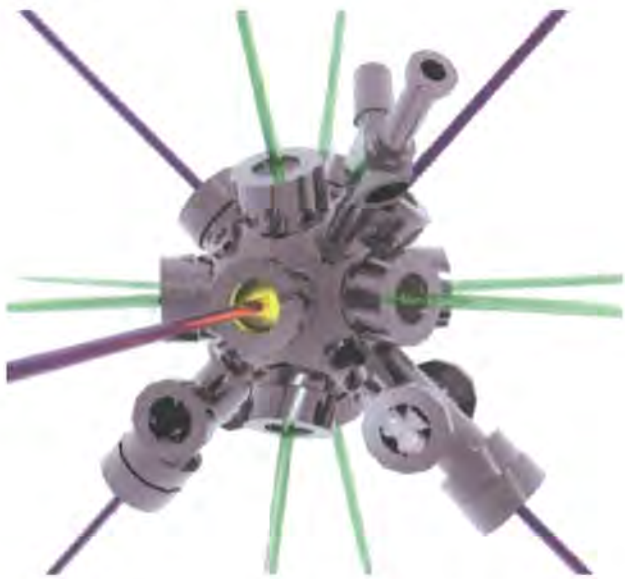

Figure 8.7: A computer generated image of what the completed 3D chamber looks like. The CO_2 beams are the lighter green beams in the diagram and the darker purple beams are the MOT beams. The pyramid MOT is connected to the arm protruding from the top right of the chamber. [Original AutoCad object created by K. J. Weatherill.]

The quadrupole magnetic field is generated by a pair of anti-Helmholtz coils that fit around the two horizontal MOT windows. Made from the same material as the P-MOT coils, these now have 36 turns (4×9), an inside (outside) radius of 38 mm (55 mm) and their centres are separated by 200 mm. They were measured producing a magnetic gradient of 0.11 G A^{-1} cm^{-1}, a value that agrees to within 2% of a theoretical model. Typically they carry 100 Amps of current provided by a Hewlett Packard 6671A/J03 (14 V, 150 A) power supply. The high currents in the coils cause Ohmic heating which requires water cooling provided by a refrigerated 5 Bar, 15° C water supply.

The high currents also require a dedicated switching system to quickly and safely turn the current on and off. Figure 8.8 shows the circuit used. The three MOSFETs (Motorola TE215N10E) sit on a water cooled brass block. The Schottky diode (International Rectifier 203CNQ100R) was initially used to prevent oscillations in the coil when the current is switched off rapidly. With the diode in place the switch off time was 10 ms. However removing the diode gives a switch off time 125 μs when operating at 90 Amps. There was no sign of oscillations, and so the experiment is operated with the diode removed. Although the switching off is fast, the turn on is slow, in fact the current overshoots before taking 0.5 s to decay to the preset level. The above values were obtained by measuring the current indirectly using a Honeywell SNR161 probe.

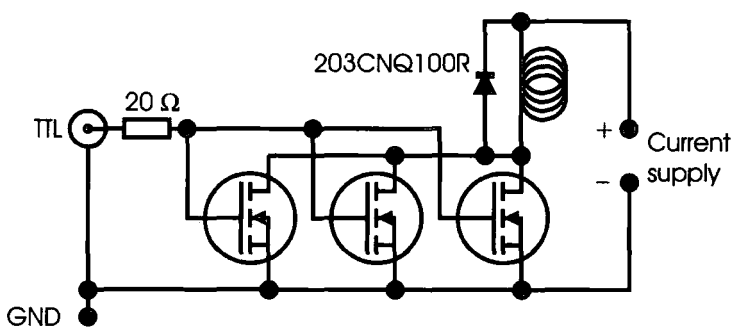

Figure 8.8: Circuit used to switch the S-MOT coils on and off.

To cancel the residual laboratory magnetic field, and allow a zero magnetic field at the optical centre of the MOT, cancelation coils were installed. Square Helmholtz coil pairs produce a uniform magnetic field over a greater volume than circular coils [167, 168]. A rectangular frame ($38 \times 64 \times 80$ cm) was built around the chamber, and used to create three independent Helmholtz coil pairs.

8.1.3 Construction, pumping and testing

The vacuum chamber construction process is fully described in ref. [163], below is a brief sketch of the steps involved. The P-MOT chamber was assembled and tested separately from the science chamber. The chambers are linked by a 75 mm long bellows of inner diameter 16 mm, a gate valve (PM Enterprises) and 40 mm straight. All the vacuum seals are made by Conflat knife-edges and annealed oxygen free, high conductivity (OFHC) copper gaskets.

It is imperative that all vacuum components are cleaned before assembly. Once assembled, apart from small amounts of hydrogen and helium permeating through the chamber walls and windows, the main source of contamination is chamber wall out-gassing. The out-gassing increases with temperature, therefore a UHV chamber is slowly baked during the initial pump down to remove as much contaminants as possible. A custom built oven was used to provide uniform heating (up to 250° C) to the chamber for the 1-2 week baking period.

Ion pumps cannot be operated above a pressure of $\sim 10^{-5}$ Torr. A 56 l/s Pfeiffer (PM033 759-T) turbomolecular pump backed up by a 2.5 m^3/s Pfeiffer (DUO 2.5 A) rotary pump were used to provide this initial vacuum. A Stanford Instruments residual gas analyser (RGA) was used to perform helium leak tests on the vacuum seals. Once a sufficiently low vacuum had been achieved in the chambers, the all metal valves were used to seal them off from the roughing pumps and RGA.

In the case of the science chamber a non-evaporative getter (NEG) pump was also activated during the baking process. The pump operates by gas molecules impinging on the surface of the getter material, then sorption takes places via a chemical reaction thus removing them from circulation. The NEG pump is ideally suited to removing H_2 and H_2O molecules.

8.2 Diode lasers and optics for cooling

8.2.1 External cavity diode lasers

In Section 2.2.2 it was shown that the frequency of laser light required to cool atoms has to be controlled at the MHz scale; which corresponds to an accuracy of 1 part in 10^9. Diode lasers are used in the majority of laser cooling experiments around the world, due to their small size, price, and 'easy' maintenance. One scheme to reduce the linewidth of the diode laser by two orders of magnitude to $\sim$ 1 MHz and that allows for frequency tuning is to make an artificial extended cavity [169, 170, 171].

In the Littrow configuration, see Figure 8.9, a diffraction grating is used to diffract the -1 order back into the laser cavity. The result is that the laser outputs a single-mode of frequency that matches the fed back light's frequency. The zeroth order light is used in the experiment.

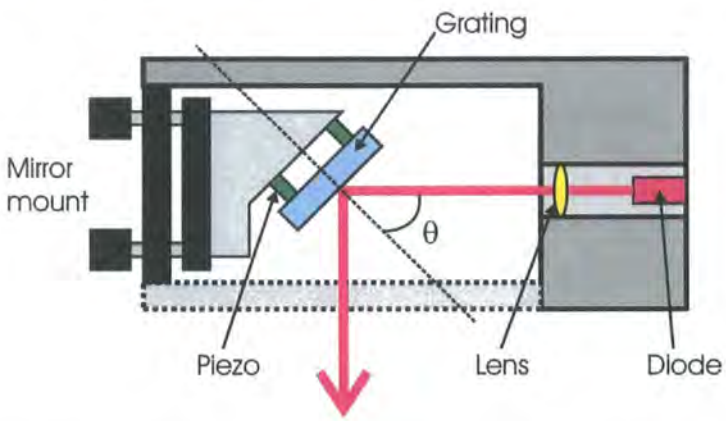

Figure 8.9: A diagram of how the External Cavity Diode Laser works.

By varying the angle of the grating, the wavelength can be tuned:

$$\lambda_C = \frac{2d \sin\theta}{n}, \tag{8.1}$$

where n is the diffraction order, d is the grating line spacing and θ is the angle between either beam and the normal to the grating. The mode selection and the increased cavity length both contribute to reducing the laser line width. The gold coated holographic diffraction gratings (Richardson Grating Laboratory)

used have 1,800 lines/mm, ($d = 0.556$ μm) resulting in a grating angle of $\theta = 44.6°$ for laser cooling Rb. This is a convenient angle as it means the beam exits the ECDL almost perpendicular to the original beam direction.

The piezo-electric actuators (Thorlabs AE0203D04) mounted on the back of the diffraction grating allow the angle and cavity length to be changed. This is a useful feature, as it allows the laser frequency to be changed over a 3 GHz range.

There are three main factors that affect the stability of the laser operation:

1. **Laser Current** - a change in the current applied to the laser diode will dramatically alter the laser light frequency. A stable current supply (Thorlabs LD1255) is used. Typically the current used is in the range 50-90 mA.

2. **Mechanical vibration** - vibration can change the grating angle and cavity length. Steps have to be taken to minimise or isolate nearby sources of vibration. A damped and air floated optics table is beneficial for isolation purposes. Sealing the laser in a box helps prevent air currents from disturbing the laser.

3. **Temperature** - the frequency of a bare laser diode is dependent upon the operating temperature ($\sim$ 150 MHz mK^{-1}). By injecting the diode using the diffraction grating the frequency is controlled by eqn. (8.1). A further temperature dependence on the frequency occurs because the cavity can now change via expansion/contraction. Operating in an air conditioned lab (19° C) and hermetically sealing the laser in a box helps reduce temperature fluctuations. A feedback circuit has been implemented using a temperature controller (Wavelength MPT-2500) so that any change in temperature, measured by a 100 kΩ thermistor underneath the laser diode, is counteracted by a Thermo Electric cooler (TEC). The temperature controller is specified to be stable to 8 mK over a 24 hour period. The lasers have been set to operate at 19.5° C.

The laser design used within the research group has evolved over the past six years, a photo of the latest design is shown in Figure 8.10. Most of the components are contained within a block of aluminium to help temperature stabilisa-

tion and maintain mechanical rigidity. The whole assembly is clamped down to the optics table which acts as a heat sink for the TEC.

The laser diodes used are manufactured by SHARP (GH0781JA2C). They are specified to operate in the 780-787 nm range, and output a maximum power of 120 mW. The diode is mounted in a lens tube assembly with collimating lens (Thorlabs LT230P-B). The 0.5" mirror mount (Thorlabs KS05) is screwed in place opposite the diode.

Although great care has been taken to keep the laser frequency stable, an identical drift of 12 MHz per hour was simultaneously measured in two separate lasers passing through the same frequency measurement optics. Thus indicating that external environmental factors are mainly responsible for the frequency drift. The drift is sufficiently large to make the lasers unsuitable for laser cooling, unless a scheme can be used to further stabilise the frequency.

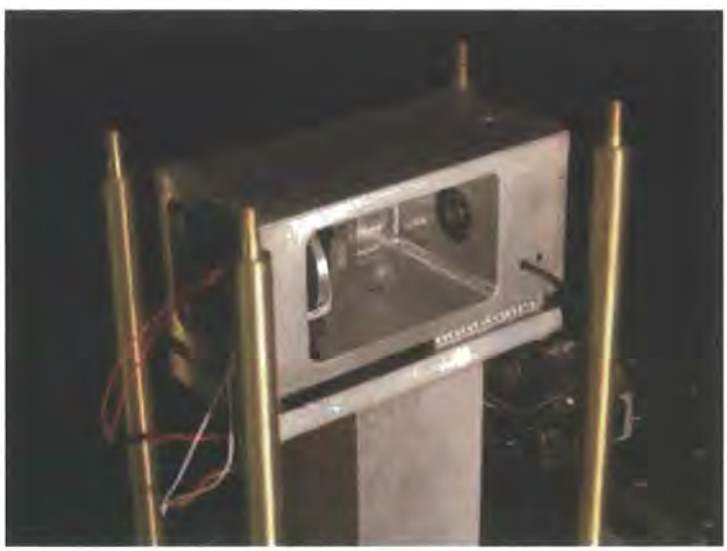

Figure 8.10: A photo of the latest External Cavity Diode Laser (Penelope) designed, built and operated at Durham. Note, cover not shown.

8.2.2 Laser spectroscopy and frequency locking

The ability to stabilise the frequency or "lock" a laser requires two things [172]. Firstly, a method to measure the change in frequency. This will be accomplished using laser spectroscopy and measuring a change in the laser intensity with a photodiode. The ideal "error signal" has a steep gradient and passes through 0 V at the required lock frequency. Secondly, a way of changing the frequency in a controlled way. This can be achieved either by varying the current or the grating position (the temperature response is too slow). The piezos mounted on the back of the diffraction grating change their length rapidly in response to an applied voltage and so will be used for locking.

A feedback circuit integrates the error signal to increase the gain and sends a correcting voltage to the piezos. An error signal of 0 V will not change the laser frequency, however non-zero voltages will cause the piezo length to change and thus bring the frequency back to the set point. The feedback circuit used, see Figure 8.11, is based upon a designs by Rovera *et al.* [173] and D. T. Smith (Oxford University). From left to right the major components are: a stable ±10 V power supply for the piezo DC bias voltage; the photodiode and an optional offset voltage are added together; an optional voltage sign flip; integrator; adding the integrated error signal to DC bias voltage.

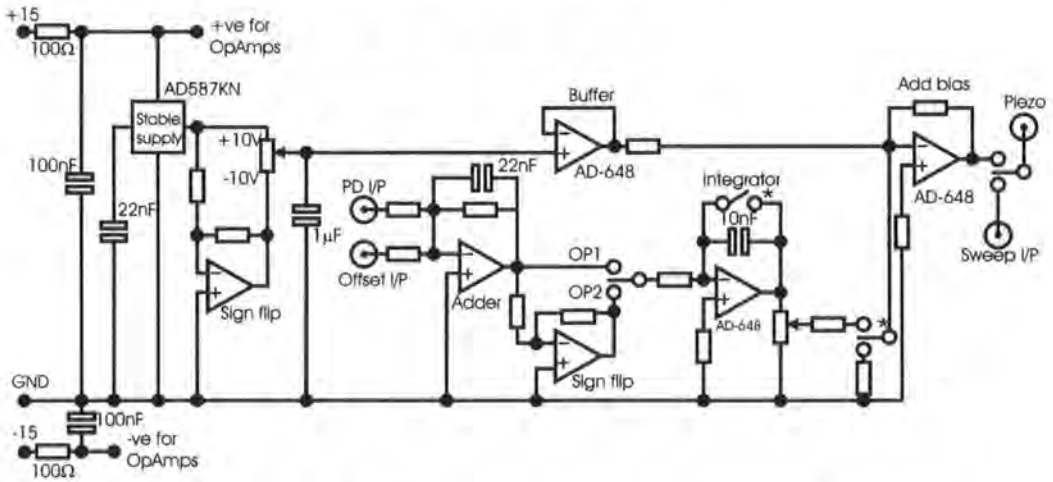

Figure 8.11: The feedback circuit used to lock the diode lasers. Unless stated all resistances are 10 kΩ and the op-amps are TL082's. Switches marked by an asterisk are linked together.

Laser Spectroscopy

The simplest example of a spectroscopic technique is absorption spectroscopy. This involves sending a laser beam through a sample of atoms. The experiment uses Rb vapour cells (Newport Corp.) that have lengths between 5 and 8 cm. If the laser frequency corresponds to an atomic transition, the light is absorbed and this results in a reduced light intensity measured by a photo diode (Siemens BPX-65). The grating piezos are used to scan the laser frequency and produce an absorption spectrum.

One would expect to see six transitions on the ^{85}Rb D2 line ($F = 2 \rightarrow F' = 1, 2, 3$ and $F = 3 \rightarrow F' = 2, 3, 4$); see Figure 2.5. However, for a room temperature sample, Doppler broadening (~ 0.5 GHz) is much larger than the excited state hyperfine splittings (~ 100 MHz). The ground state hyperfine splitting is 3 GHz and so this results in only two observable absorption features instead of six ($F = 2 \rightarrow F'$ and $F = 3 \rightarrow F'$). The shape of each feature is the combination of three closely spaced Gaussian profiles with different heights.

One method to resolve the excited state hyperfine structure is pump-probe saturated absorption spectroscopy, described in [174] and explored further in a recent publication [175]. The experimental setup is shown in Figure 8.12 (a). The laser beam is split into two parts: a weak probe beam and a stronger counter-propagating pump beam. A simpler experimental realisation, that has the advantage of a zero crossing angle but the disadvantage of sacrificing independent power control, is shown in Figure 8.12 (b).

The condition for the two counter-propagating lasers to be resonant with the same transition is that the atom is stationary. The stronger pump laser saturates the atomic sample, and therefore the probe laser experiences fewer atoms in the ground state, resulting in diminished absorption. One final feature that occurs is *cross-over peaks*. These occur because it is possible for a moving atom to have two different transitions resonant with the laser light since the Doppler shift changes the frequency. The pump and probe lasers now operate on different transitions. As before the stronger pump beam excites most of the atoms from the ground state to one excited state, which leaves a small ground state population for the probe laser to excite to a second excited level. The spectrum for both the ^{85}Rb and ^{87}Rb isotopes is shown in Figure 8.13.

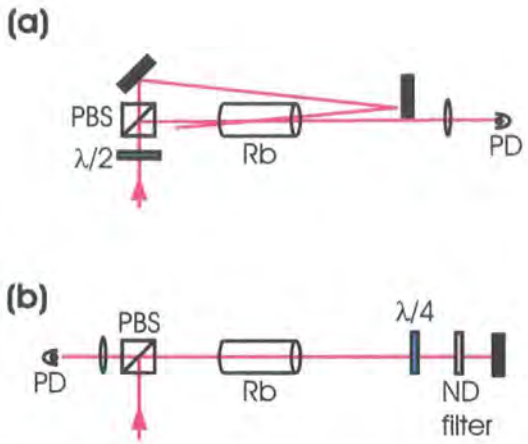

Figure 8.12: Optical setups used for pump-probe saturated absorption spectroscopy. Setup (a) is more flexible and setup (b) is a simpler experimental realisation. The abbreviations used are: ND = neutral density; PBS = polarising beam splitter; PD = photodiode; $\lambda/4$ = quarter waveplate; $\lambda/2$ = half waveplate.

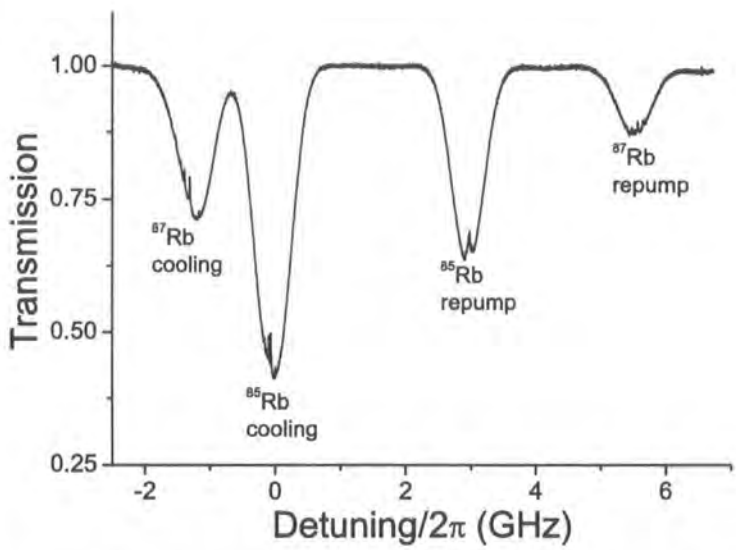

Figure 8.13: A pump-probe saturated absorption spectrum for the D2 line transitions in both the ^{85}Rb and ^{87}Rb isotopes.

A close-up of the ^{85}Rb $F = 3 \rightarrow F'$ transitions is shown in Figure 8.14 (a). In this figure the Doppler broadened background has been subtracted leaving just the hyperfine structure. This was done by sending a second probe beam through the vapour cell that does not overlap with a counter-propagating pump beam and so only measures the Doppler background. By taking a difference of the two photodiode signals, the Doppler background is removed.

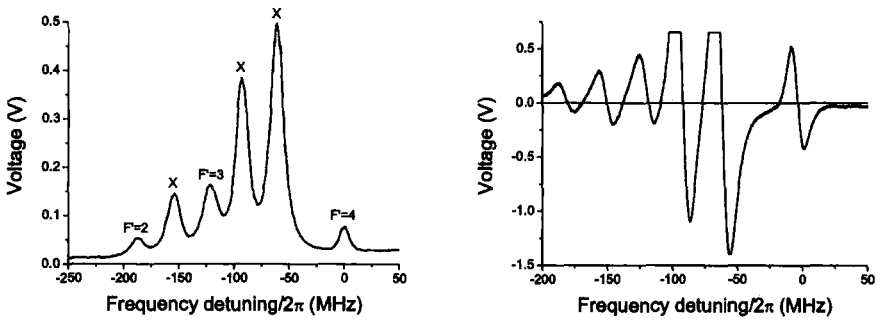

Figure 8.14: Plot (a): A pump-probe saturated absorption spectrum for the D2 line transition $F = 3 \rightarrow F'$ in ^{85}Rb. The Doppler broadened background has been subtracted and X denotes a cross-over peak. Plot (b): The time averaged error signal from the lock-in amplifier for the D2 line transition $F = 3 \rightarrow F'$ in ^{85}Rb. Zero crossings are found at the peaks of the spectra. The photodiode saturates above 0.6 V.

Dither or peak locking

Having obtained the frequency spectrum, one way to produce the required error signal is to take a derivative, in doing so the peaks of each transition will become zeroes as required. An approximation to taking a derivative is to perform a *dither lock*. In this case the laser frequency is modulated by adding a small AC current to the diode current. A lock-in amplifier multiplies the photodiode output with the modulation, and outputs a derivative signal, which is proportional to the time average of the product. The spectrum of Figure 8.14 (a) was modulated with a 40 kHz sine wave on the diode current, and the output of the lock-in amplifier is shown in Figure 8.14 (b). The lock has a capture range of 10 MHz, and the lock gradient is -0.13 V MHz^{-1} on the cooling transition. When the laser is locked to the cooling transition the error signal from the lock-in amplifier has a standard deviation of 0.011 V.

The main disadvantage is that by artificially adding a modulation to the laser current it will increase the linewidth of the laser, one of the properties that laser locking should be reducing. One method to circumvent this is to apply a frequency dither through the use of acousto-optical modulators on a split off part of the laser beam, leaving the remainder of the beam unaffected. A further disadvantage with dither locking is that it is the most technically/electronically demanding of the methods presented in this thesis. Each extra electronic component adds additional cost to the experimental setup.

Polarisation spectroscopy locking

A laser lock can be achieved via polarisation spectroscopy. The optical setup described here was developed in Durham and is discussed thoroughly in refs. [176, 177, 178]. A weak probe beam measures the induced birefringence in a vapour cell caused by sending a counter-propagating circularly polarised pump beam through the medium, see Figure 8.15 (a).

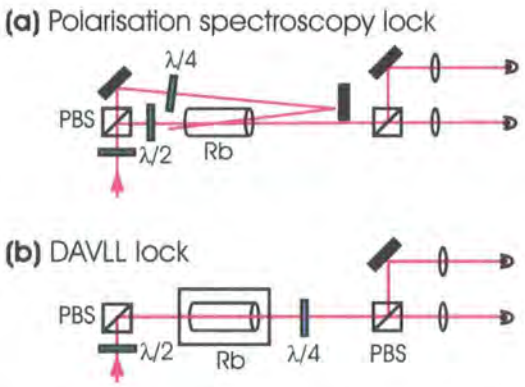

Figure 8.15: Optics setups for (a) polarisation and (b) DAVLL locking. In the DAVLL setup the Rb vapour cell is placed in a solenoid created from permanent magnets.

The second polarising beam splitting (PBS) cube and photodiodes analyse the two orthogonal linear polarisations. The difference in signals is a measure of the change in refractive index:

$$\Delta n(\delta') = \frac{\Delta\alpha_0}{k}\frac{\delta'}{1+\delta'^2}, \tag{8.2}$$

where δ' is the laser detuning from resonance in units of the power broadened transition linewidth, k is the laser wavevector, and $\Delta\alpha_o$ is the maximum difference in absorption at line centre. If there was no decay term, $1/(1+\delta'^2)$, it can be seen that the change in refractive index is proportional to the detuning. In Figure 8.16 (a) the horizontal and vertical polarisations were measured for the D2 line transition $F = 3 \rightarrow F'$ in ^{85}Rb. The error signal for the cooling transition can be seen in Figure 8.16 (b), where the difference in photodiode signals is plotted. The lock has a linear capture range of 10 MHz, and the lock gradient is -0.013 V MHz^{-1}.

A disadvantage is there is an inherent ambiguity over the exact frequency that

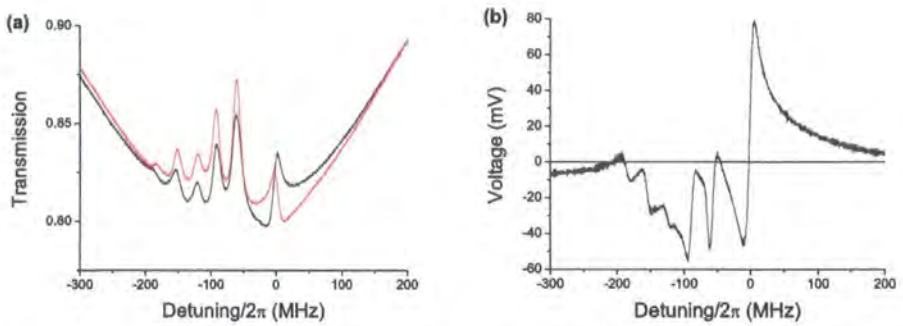

Figure 8.16: Plot (a): The horizonal and vertical polarisation signals from the experimental setup shown in Figure 8.15 (a) are plotted. Plot (b): The difference of the two polarisation signals. The zero crossing close to 0 MHz has a steep gradient making it a good error signal to lock the laser to.

the laser is locking to, in Figure 8.16 (b) the lock point is detuned from the cooling transition by 2.4 MHz. Furthermore, the setup is very susceptible to magnetic fields, as can be seen by placing a magnet next to the vapour cell. This can be advantageous as the field, if correctly aligned, can be used to boost the lock signal by a factor of 5.

Dichroic Atomic Vapour Laser Lock (DAVLL)

In this method of locking a laser, the vapour cell is placed into a weak magnetic field ($\sim$ 150 G) created from permanent magnets [179, 180]. See Figure 8.15 (b) for a diagram of the experimental setup. The magnetic field splits the Zeeman components of the Doppler broadened absorption spectrum. Linearly polarised light can be thought of as a superposition of right- and left-handed circular polarisation. The two different circular polarisations have their central absorption frequency shifted in opposite directions due to the Zeeman shift. The quarter wave plate and PBS cube change the two orthogonal circular polarisation components into two linear polarisation components. The difference in the two photodiode signals produces a suitable error signal. Figure 8.17 gives experimental results for Rubidium.

As in the case of polarisation spectroscopy, there is an inherent ambiguity in the lock frequency, this is especially pronounced in the DAVLL. The large capture range does allow the flexibility to add an offset voltage to the error signal. In combination with a saturated absorption spectrum, as a frequency reference,

it is possible to linearly tune the laser frequency over $\sim$ 300 MHz. Experience with the DAVLL has shown that the low lock gradient of 0.003 V MHz^{-1} does not supply a tight lock. However, the large capture range makes the DAVLL ideal for locking the repumping laser as the exact frequency is not critical.

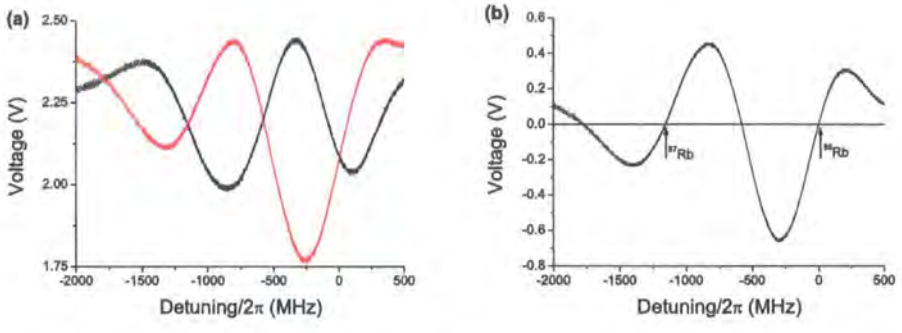

Figure 8.17: Plot (a): The horizonal and vertical polarisation signals from the experimental setup shown in Figure 8.15 (b) are plotted. Plot (b): The difference of the two signals above. The zero crossing at the cooling transition is evident for both the ^{85}Rb and ^{87}Rb isotopes.

Heterodyning or "beating" lasers

Attention is now turned to exploring the locked laser's linewidth. A crude (and incorrect, see ref. [169]) assessment is based upon measuring the error signal within the electronic feedback loop. A better method is to heterodyne or 'beat' two lasers [181, 182]. When two laser beams are co-propagating and are incident on a photodiode, a temporal interference pattern is established, see Figure 8.18. The beat frequency is equal to the frequency difference of the two lasers. From this two different measurements can be made:

1. **Relative frequency drift** - Measuring the frequency shift of the beat note gives the relative frequency drift of the two lasers. To get an absolute measure of the frequency drift requires beating all the pair combinations of three laser beams. Another measure of the frequency drift is to see how the raw beat signal behaves when it is time-averaged. This results in an envelope surrounding the beat note as shown in Figure 8.18. The larger the envelope, the more stable the laser is.

2. **Linewidth** - The Fourier transform of the raw beat signal gives a Lorentzian peak centred on the beat frequency. The full width half maximum of the peak is a measure of the convolution of the two lasers' linewidths. In Figure 8.19 the linear Fourier transform of two lasers locked by (a) dither lock and (b) polarisation lock are shown. It can be seen that the linewidth of the dither lock (2.0 MHz) is five times greater than the polarisation lock (0.4 MHz). This is possibly a manifestation of the artificially created laser linewidth caused by the current modulation. The linewidth was obtained by taking half the full width half maximum.

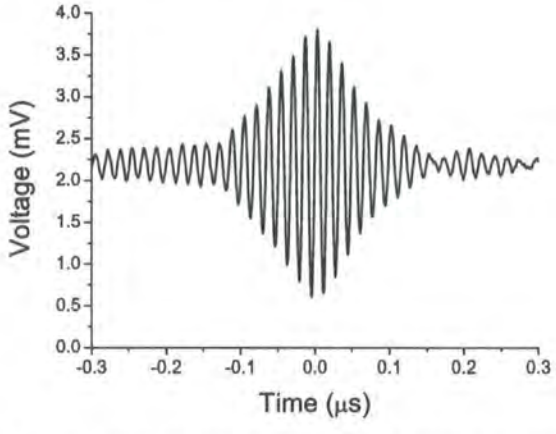

Figure 8.18: A time average of 8 readings for the raw beat note signal. The envelope surrounding the beat note is a measure of how stable the laser is.

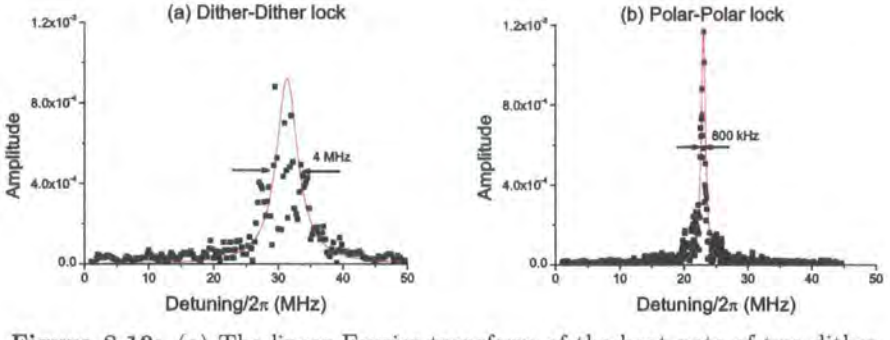

Figure 8.19: (a) The linear Fourier transform of the beat note of two dither locked lasers. (b) The Fourier transform of the beat note of two polarisation spectroscopy locked lasers. The same two lasers were used in making the two plots. The lines of best fit are Lorentzian curves.

8.2.3 Implementing laser cooling

In principle laser cooling is straight forward, all that is required is two lasers with sufficient power and operating at the correct frequency. However, most experiments require the flexibility to modify the light's frequency and extinguish the light on a microsecond timescale. Add to that the complications of beam shaping and avoiding light feeding back to the laser, and the optics setup starts to resemble a spiders web. In Figure 8.20 the optics layout before the fibre optics is shown. The table has been divided into three zones.

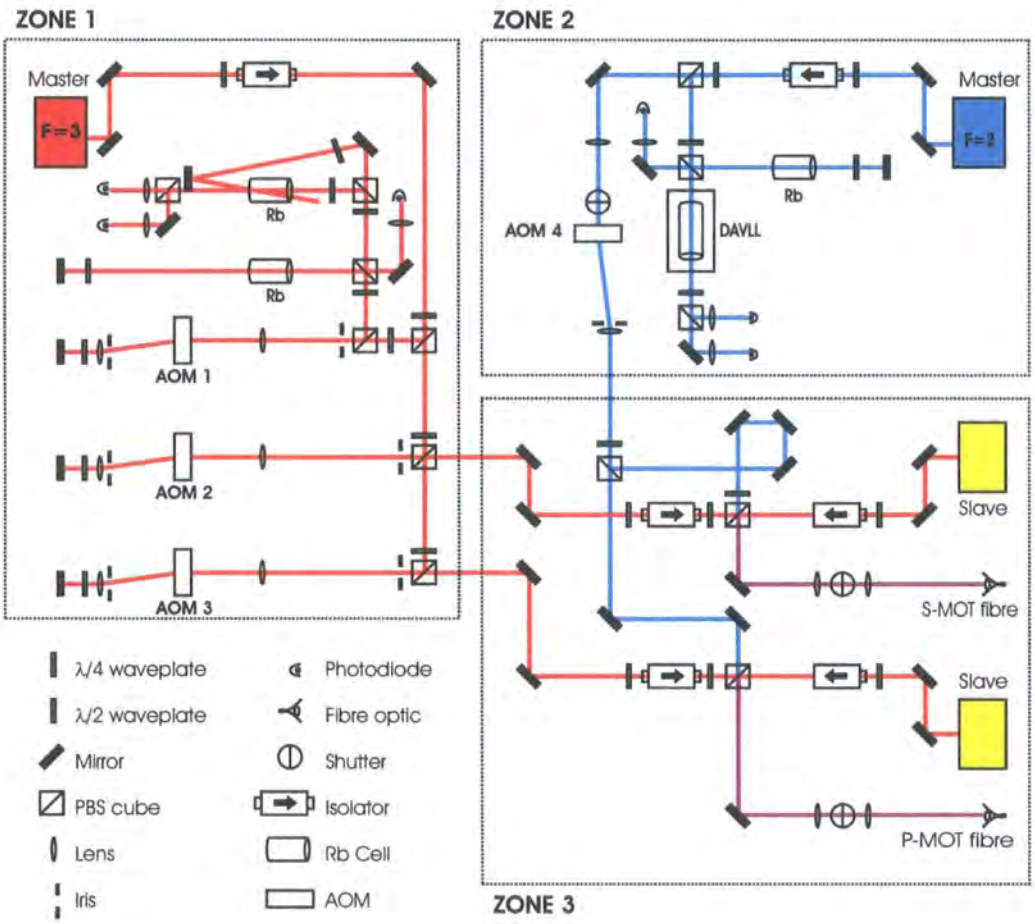

Figure 8.20: The layout of the optics table before the fibre optics taking the light to the vacuum chamber. The beam's are coloured as follows: red for cooling light; blue for repumping light; purple for co-propagating cooling and repumping light. All optics are in a horizontal plane 10 cm above the optics table. For clarity purposes the diagram is not drawn to scale.

The purpose of **Zone 1** is to generate the cooling light. The -40 dB optical isolator (Gsänger/Linos) acts as an optical diode to stop light being fed back into the laser cavity. The main change from the setup given in the previous section is the introduction of acousto-optical modulators (AOM) which can be used to change the light frequency. Within the AOM a rf-signal causes a piezo-electric transducer to vibrate, which creates sound waves in a neighboring piece of quartz. Incoming light scatters off the moving sound wave and interference results in a phenomenon similar to Bragg diffraction. The light frequency is changed in the process: $\omega_L \rightarrow \omega_L + n\omega$, where n is the diffraction order and ω is the angular frequency of the AOM's rf-signal. The experiment uses Isle Optics AOMs. The rf-signal is created by the following sequence: voltage controlled oscillator (MiniCircuits ZOS 100) $\rightarrow$ variable voltage attenuator (MiniCircuits ZX73-2500)$\rightarrow$ amplifier (MiniCircuits ZHL-3A). The input voltages to the oscillator and attenuator are controlled via a level box which allows four preset analogue voltages to be switched using TTL signals.

The distribution of the laser power after the isolator in Figure 8.20 is: 10% to AOM1; 45% to AOM2; 45% to AOM3. For each beam passing through an AOM, the -1 order is selected using an iris. Therefore the AOM changes the light frequency by $-\omega_i$, where the index i is the AOM number. The beams then pass through a $\lambda/4$ waveplate before being retro-reflected through the waveplate again. If the waveplate angle is correctly set, this will cause the beam's polarisation to be rotated by 90°, allowing the beams to be redirected by polarising beam splitting (PBS) cubes later. The beams continue through the AOMs for a second time. Again the -1 order is selected, and this light's angular frequency has now been changed by $-2\omega_i$.

The beam from AOM1 is sent into the spectroscopy region where the frequency is locked to the centre of the cooling transition ($5^2S_{1/2}, F = 3 \rightarrow 5^2P_{3/2}, F' = 4$) using polarisation spectroscopy. An additional saturated absorption spectroscopy arm is used to monitor the frequency that is being locked to. The changes in frequency are illustrated in Figure 8.21, where light on resonance with the cooling transition has been defined as having zero detuning. The beam from AOM2 is sent across to **Zone 3** with a detuning given by $2(\omega_1 - \omega_2)$. If $\omega_1 < \omega_2$ the light has a negative detuning from resonance as required for laser cooling. As the AOM frequencies are set electronically, this gives a lot of flexi-

bility in controlling the detuning. An identical process occurs for light passing through AOM3.

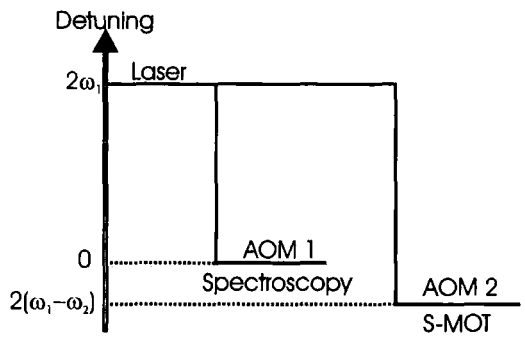

Figure 8.21: A small frequency detuning is created between light entering the spectroscopy arm and light sent to the vacuum chamber.

The physics of generating the repumping light in **Zone 2** is much simpler. In this case the light frequency is not modified by an AOM before entering the spectroscopy/locking region. A DAVLL and reference absorption spectroscopy arm are used to set the repump laser frequency ($5^2S_{1/2}, F = 2 \rightarrow 5^2P_{3/2}, F' = 3$). In practise the frequency detuning is fine tuned, using an offset voltage on the DAVLL error signal, to optimise the MOT fluorescence. The main addition is the use of a shutter and a single pass AOM before the light enters **Zone 3**. Both are used to extinguish the repumping light. The AOM can attenuate the light in a few microseconds, however this does not result in full extinction. The shutter, see Section 8.2.4, is slower but results in full extinction of the light.

By the time the cooling light has reached **Zone 3** the power has been greatly diminished by losses on the optical elements. *Slave lasers* are used to boost the laser power. The slave lasers have no external cavity, instead light is fed into them from the *master lasers* causing them to adopt the new frequency. The slave lasers have a high power output, and the beam path to the fibre optic only has minimal optical elements at which power loss can occur. The four optical isolators are used to stop back reflections into either the slave lasers or the spectroscopy/locking arms. The two slave isolators have their back face (rotatable PBS cube) removed to allow the correctly polarised master light to enter the slave laser. The slave outputs and the repumping light is combined on the PBS cubes and steered into the fibre optics, the alignment of which is described in Appendix G. On route to the fibres they pass through shutters

that can completely extinguish the light going to the vacuum chambers.

Each fibre outputs 30 mW of cooling light and 5 mW of repumping light which are sent to the MOTs. The P-MOT optics have already been discussed (Figure 8.4) and so now the S-MOT optics are described, see Figure 8.22. The beam leaving the fibre optic is allowed to expand before being collimated by a $f = 8$ cm lens. A knife edge measurement, see Appendix H, gives a $1/e^2$ radius of 7.5 mm. Three PBS cubes are used to produce three beams of equal power (peak intensity of 7.1 mW/cm^2) which enter the vacuum chamber before being retro-reflected.

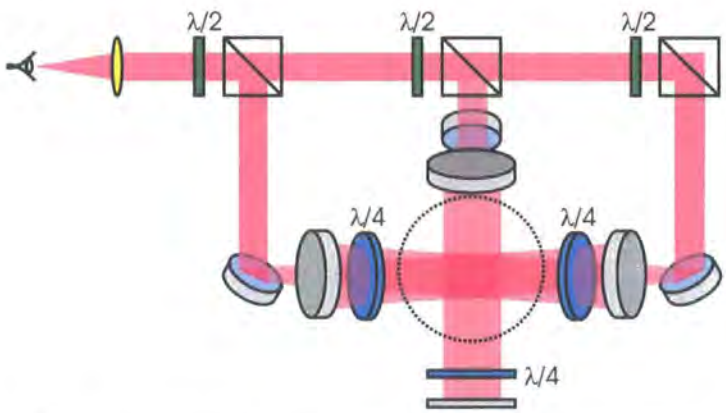

Figure 8.22: Optics to produce a second MOT. The left and right arms are sent diagonally up through the chamber before being retro-reflected. The middle arm's height is raised by a two mirror periscope before traveling horizontally through the chamber and then retro-reflected. The chamber is indicated by the dotted black circle. Diagram not to scale.

8.2.4 Low cost laser shutters

The time sequence of the experiment requires fast shuttering of laser beams for imaging pulses and to remove any unwanted laser light that may cause atomic heating. AOMs can switch within a microsecond, however they never completely extinguish the light. A mechanical shutter to physically block the light source is also required. Commercial shutters are available but are expensive to buy. Low cost shutters, that performance match commercial devices, can easily be built from solenoids, piezoelectric actuators [183], speakers [184] and hard disk drives [185].

The experiment uses three different types of home built shutters. The performance of the three designs are compared in Table 8.1. The first are safety shutters installed at the laser output and are built from solenoids (Farnell 176583). Beam blocks are held above the beam, if the room's interlock circuit is broken or an emergency stop button is pressed the beam block drops under gravity in front of the laser beam. The simple design is relatively slow to switch off. However, using gravity is a fail safe method in case of power cuts. The second and third designs operate using an electronic push-pull circuit, see Figure 8.23, that has been based on a similar design given in ref. [184]. A TTL signal can change the direction of current flow in the shutter coil.

	Solenoid	Speaker coil	Hard disk
Cost	£20	£10	£20
Size (footprint)	2 cm^2	4 cm^2	2 cm × 6 cm
Switching speed	1 sec	0.1 ms	0.1 ms
Vibration	Low	Low	Moderate
Reliability	Low	Average	High
Swing length	8 mm	4 mm	30 mm
Ease of construction	Moderate	Easy	Moderate

Table 8.1: The three shutter designs are compared.

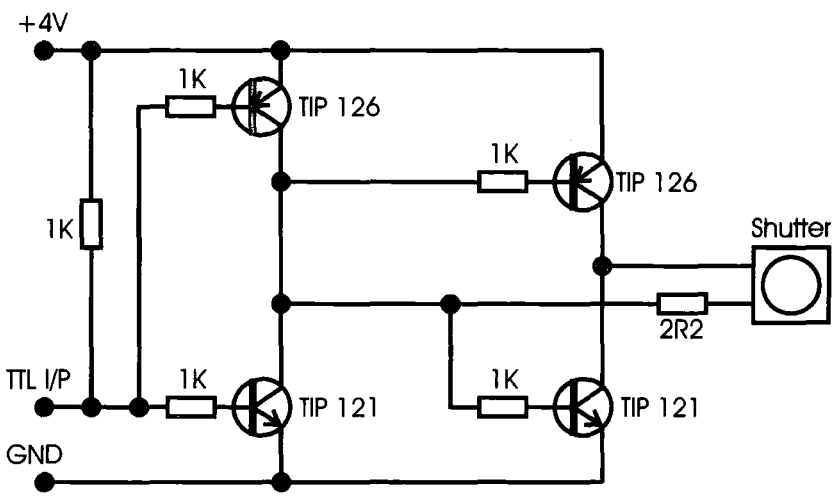

Figure 8.23: The laser shutter push-pull driving circuit. The 2Ω resistor in series with the shutter protects the coil from being damaged by power surges.

The second design uses the movement of a computer speaker coil to move a beam block into the laser beam [184]. The construction process is shown in

the series of photos in Figure 8.24. The 2.5" diameter, 0.2W speakers (Farnell 599-256) cost £2.50 each. The first stage is to remove the black cardboard disk, this is easily achieved with a scalpel and nail scissors. It is important to leave sufficient cardboard around the region near the thin delicate wires that link the electrical terminal to the coil. The outer metal rim is removed with tin snips. Then the orange webbing is cut away to only leave four tabs ($\sim$ 3 mm wide) linking the main body to the floating coil. Apart from damaging the wires (either breaking or short circuiting) the other major factor that reduces the lifetime of the speaker is the tabs ripping. Speakers made with less than fours tabs, or thin tabs, were observed to break easily. Also, like a lot of fabric, a tiny cut on the edge of the webbing is enough to cause severe weakening. The next step is to cut out the disk of cardboard that is inside the coil. The reduced mass and air drag shortens the shutter's switching time. At this point the permanent magnet within the speaker is exposed, so care must be taken to avoid metal filings entering the speaker's core. A beam block was fashioned from 0.2 mm thick brass shim and spray painted matte black before being glued onto the coil. The final stage involves mounting the speaker and attaching current leads.

Figure 8.24: A series of photos showing various stages of constructing a laser shutter made from a speaker coil.

The third design uses the voice-coil motor within a computer hard disk to move a beam block into the laser beam [185]. The construction process is shown in the series of photos in Figure 8.25. The hard disks used were acquired from broken computers, the design featured in the photos is a DiamondMax Plus 9 (80Gb SATA/150 HDD). However, most modern hard disks are adaptable.

The first stage in construction is removing the electronic circuitry on the back of the hard disk. Removing the front cover, the storage disk is found at one end and the voice coil motor and pick-up head circuitry at the other end. The next stage is to remove the strong earth magnet cover and the pick-up arm.

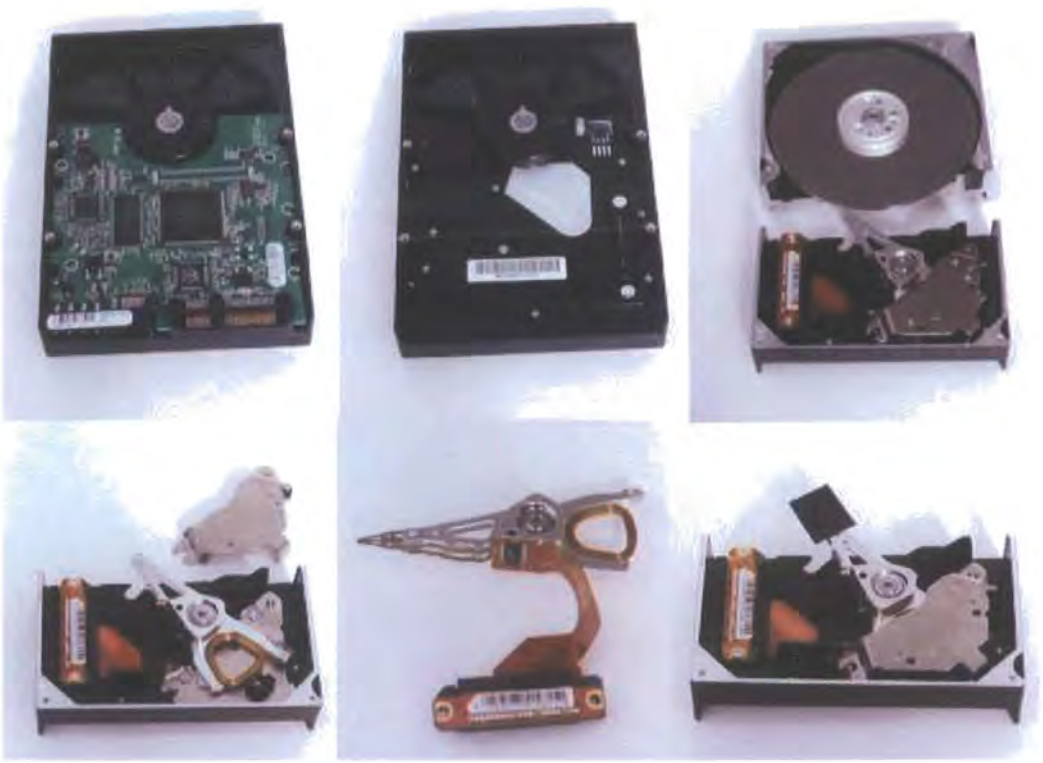

Figure 8.25: A series of photos showing various stages of constructing a laser shutter made from a hard disk drive.

Care must be taken doing this as the strong magnetic attraction can crush components and fingers once the mounting screws are removed. The storage disk is now removed. Depending upon the hard disk design, the pick-up arm and storage disk may need to be removed simultaneously. The stripped down case can now be cut down further with a saw. Before reattaching the pick-up arm, it is worthwhile removing as much mass from the arm as possible to increase the movement speed. A black cardboard beam block is glued on the end of the arm. The final stage is to attach electrical connections to the wires leading to the voice-coil motor.

There are two problems associated with the hard disk design. The swing action is very strong compared with the other two designs, and so has the potential to create undesired vibration. This is combatted with foam insulation on the arm movement stops and the base where it is clamped to the optics table. The second problem is some hard disks use the case for grounding. Any clamps used to hold the shutter to the table should therefore be insulated.

8.3 CO_2 laser and dipole trapping optics

The alignment of the CO_2 laser and the ZnSe optics on the experiment were performed by Kevin Weatherill, see ref. [163] for details. For completeness, the setup used and how it fits around the experiment is briefly described in this section. Figure 8.26 shows the initial optics path that will be used to create a 1D optical lattice.

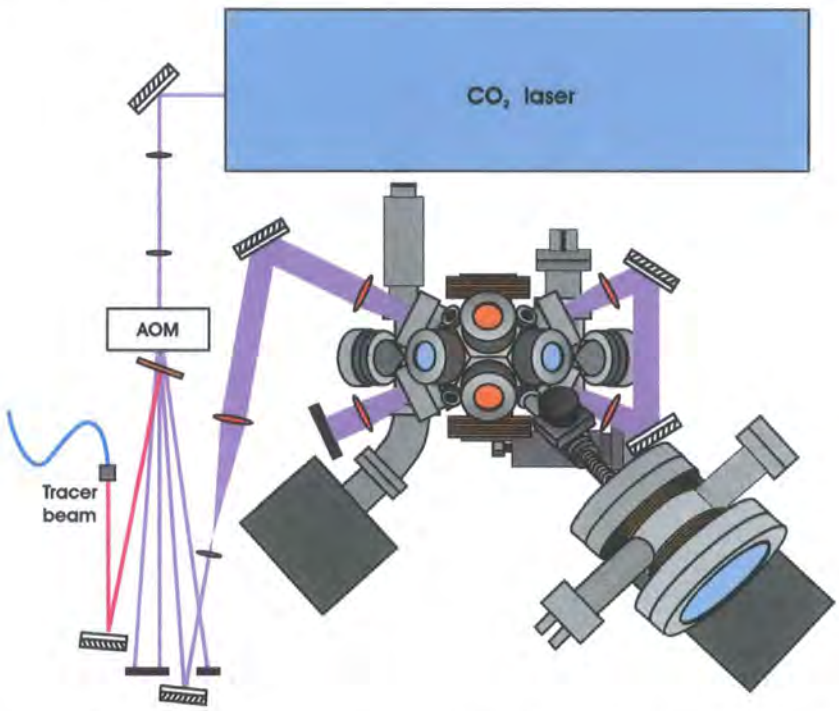

Figure 8.26: The CO_2 laser optics. The diode laser tracer beam is combined with the CO_2 beam (1st order diffraction) on the ZnSe slide. [Figure adapted from an original object created by Kevin Weatherill]

The CO_2 laser is a Coherent-DEOS GEM100 Select powered by a Agilent 657-3A DC power supply (35 V, 60 A). The laser is water cooled by a Thermo NesLab HX150 chiller. The first lens telescope is used to reduce the beam size to 3 mm $1/e^2$ radius to pass through the water cooled AOM (IntraAction Corp. AGM-406BIM) driven by a 30 W, 40 MHz rf-supply (IntraAction GE-4030). The AOM is used to control the laser power that enters chamber. The diffracted 1st order is sent to the chamber, whilst the -1st, 0th and 2nd orders are beam dumped on fire bricks. The second lens telescope is used to expand the beam to 8.6 mm $1/e^2$ radius before being focused by a 19.5 cm lens into the

centre of the chamber. The beam exiting the chamber is collimated and then refocused into the chamber by further mirrors and ZnSe lenses.

Alignment of the laser is both hazardous and complicated. The danger lies in the 100 W of invisible radiation, even reflections off windows have sufficient power to burn or blind. The complication lies both in tracing the beam path and in the large diffraction exhibited by the CO_2 laser ($z_R \propto 1/\lambda_T$). To aid alignment a diode laser tracer beam was overlapped with the CO_2 beam after the AOM. The coarse alignment of the mirrors and lenses could be performed with the tracer beam, and then the fine alignment is performed with the CO_2 laser switched on. Knife edge measurements, see Appendix H, using a water cooled thermopile power meter (Coherent) are a very useful method (albeit a tedious one!) for determining the beam profile. Multiple beam profiles along the axis of beam propagation can be used with knowledge of Gaussian optics to extrapolate the beams profile further up or down stream.

8.4 Imaging and computer control

The experiment makes use of three different cameras. The first are low cost, low resolution CCTV cameras used to monitor the MOTs. The second type are JAI CV-M50-IR CCD cameras that are used for image capturing through LabView. The third type is an electron multiplied CCD camera (EMCCD). The high resolution camera from Andor (iXon DV885) has 1004×1002 pixels with a pixel size of 8×8 μm. The purpose of this camera is to image the optical lattice sites.

A high resolution objective lens system was designed based upon a similar design by Wolfgang Alt [186]. Four lenses are used, the idea being that the aberrations of one surface can be canceled by other ones. Oslo LT design software was used to calculate the lens separations that minimise the spherical aberrations, see Table 8.2. A ray tracing of light passing through the four lenses and ZnSe window is shown in Figure 8.27. The resolution is measured using a 1951 USAF resolution test chart, see Figure 8.28.

Surface	Radius (mm)	Thickness (mm)	Material
1	0.0	4	BK7
2	77.2	10.0	Air
3	153.3	7.2	BK7
4	-153.3	0.1	Air
5	128.8	5.5	BK7
6	0.0	0.4	Air
7	153.8	5.0	BK7
8	393.4	10.0	Air
9	0.0	5.0	ZnSe
10	0.0	130.0	Vacuum

Table 8.2: The surface number, radius of curvature, thickness to next surface and material are tabulated for the four lens objective.

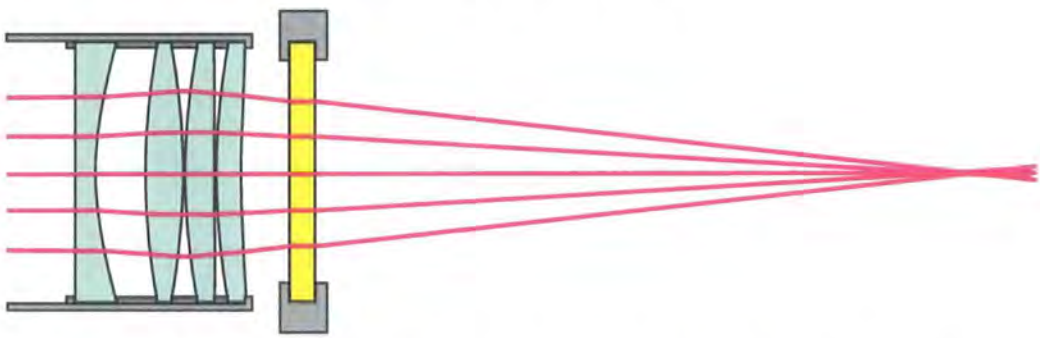

Figure 8.27: Ray tracing through the four lens objective and ZnSe window. The anti-reflected (near IR) coated lenses bought from Thorlabs are from left to right: -150 mm plano-concave (LC1611-B); +150 mm bi-convex (LB1374-B); +250 mm plano-convex (LA1301-B); +400 mm meniscus (LE1359-B). The focus occurs 145 mm away from the four lens system.

Two PCs are used in running the experiment, see Figure 8.29. The first PC controls the experiment with the aid of National Instruments' hardware and software. Three cards that use the PC's interface bus are used: an Analog card (PCI-6713) for controlling the CO_2 laser's AOM and providing a clock signal to run the experiment by; a Digital Input/Output (DIO) card (PCI-DIO-32HS) which sends TTL signals to the various shutters, coils, and AOM level boxes; an Image Acquisition (IMAQ PCI-1408) card to capture images from the JAI cameras. The three cards' timing are linked by a *real time synchronous interface* (RTSI) bus. The graphical programming language LabVIEW 7.0 is used to control the cards. The second PC operates the Andor camera and performs image analysis on the results. This type of operation is the most

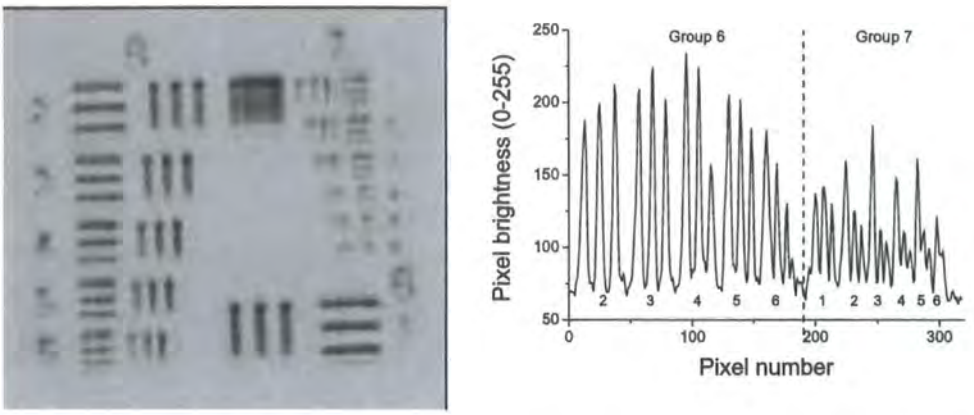

Figure 8.28: On the left is an image capture from the CCD camera of the 1951 USAF resolution test chart. To the right is a plot of brightness against pixel number. The three lines cease to be distinguishable at Group 7, Element 4. Corresponding to a line spacing of 5.52 μm, which should be sufficient to resolve the optical lattice sites.

computationally intensive, so the use of the second PC avoids any undesired slowing down of the LabVIEW routines.

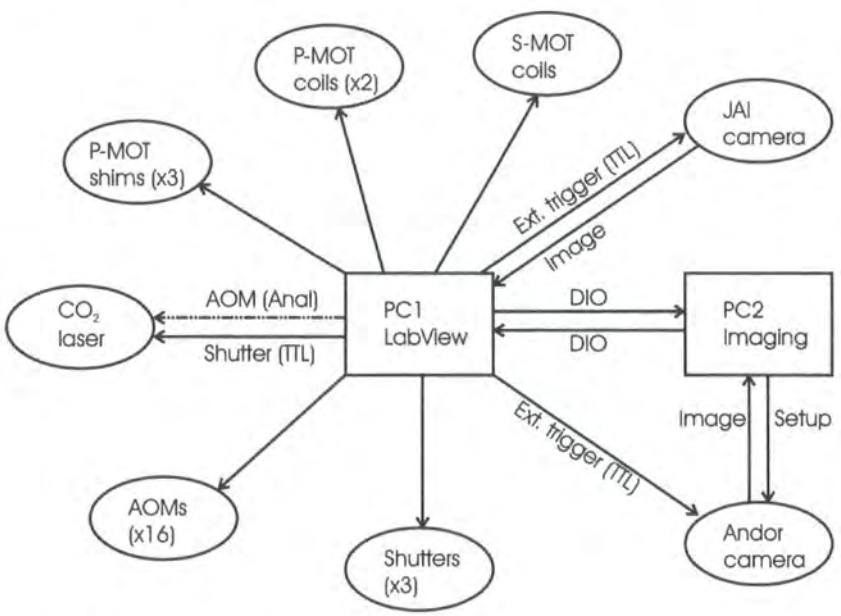

Figure 8.29: Experiment control wiring diagram. The majority of wires carry TTL signals, the exceptions are the analog line to the CO_2 laser's AOM and the imaging lines.

Chapter 8 summary

- The design and construction of the differentially pumped, dual-chamber vacuum system were described. The coils required to create the quadrupole magnetic field needed in the MOTs were presented along with switching circuits.
- The steps needed to frequency stabilise diode lasers were introduced. Three spectroscopy schemes to create suitable locking "error signals" were explained and spectrums presented.
- The optical layout for generating the laser cooling light was described. Three different designs for making low cost laser shutters were outlined. A basic overview of the CO_2 laser setup was given.
- The imaging cameras, lenses and computer infrastructure for controlling the experiment were described.

Chapter 9

Optimising the MOTs

"The major difference between a thing that might go wrong and a thing that cannot possibly go wrong is that when a thing that cannot possibly go wrong goes wrong it usually turns out to be impossible to get at or repair."
Douglas Adams

This chapter describes the initial results and optimisation process of the two MOTs. The fluorescence from the S-MOT is used to give an estimate for the number of trapped atoms.

9.1 P-MOT

Cold atoms were first observed in the P-MOT on 13th December 2004. This was shortly before the two chambers were combined together and re-baked. An image of the cold atoms is shown in Figure 9.1. The image is complicated by single and double reflections off the pyramid mirrors. The true cloud (circled) is determined by moving the cloud with the magnetic shim coils. When the cloud is moved close to the square hole at the pyramid apex, the cloud is seen to rapidly disappear down it. The cloud takes ~ 2 s to reform when the magnetic field centre has been moved away from the hole.

The P-MOT is a robust source of cold atoms and tolerates some misalignment before the cold atoms are lost. The $\lambda/4$ waveplate converting the incoming

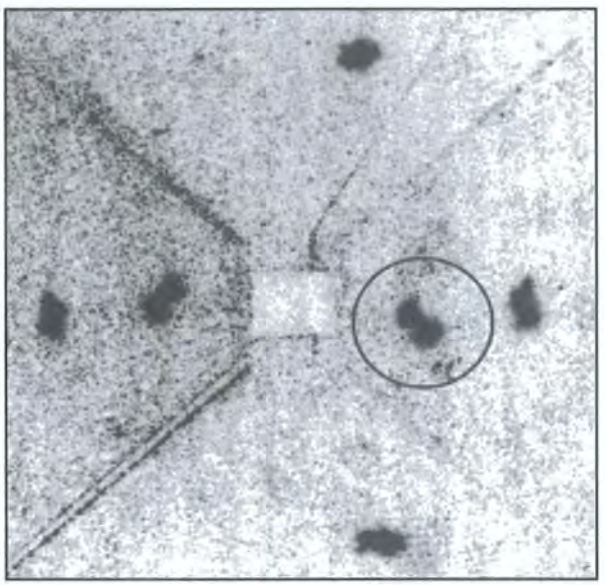

Figure 9.1: Inverted CCD image of the fluorescence from the cold atom cloud in the P-MOT. The image covers a 15×15 mm^2 area. The circle indicates the true cloud, and the five other clouds are reflections off the mirrors. The central faint square is the 2 mm hole at the apex of the pyramid. The darker diagonal lines occur at the prism-mirror interface.

linearly polarised light into circularly polarised light has a 45° tolerance on the rotation angle. The incoming angle of the light can be misaligned by up to 5° without losing the MOT. Laser cooling can occur at relatively low powers. The first P-MOT was obtained with 10 mW of cooling and 3 mW of repumping light. When the cooling light frequency detuning is brought closer to resonance the atom cloud becomes distorted and begins to oscillate before eventually being destroyed. A detuning of $-2\pi \times 12$ MHz produces an image of a large and stable cold atom cloud on the CCD camera. The repumping light detuning has a much higher tolerance and an atomic cloud is observed over a $2\pi \times 100$ MHz range. The detuning is set by optimising the fluorescence seen on the CCD camera.

9.2 S-MOT

After combining chambers and setting the experiment up in a new lab, cold atoms were first observed in the S-MOT on 31st July 2005. The first images obtained are shown in Figure 9.2. In this figure the left hand side shows the S-MOT being loaded by a flux of cold atoms from the P-MOT, the right image is with the P-MOT light shuttered off and therefore with the cold atom flux stopped. The lack of background scattering and multiple cloud images allows quantitative measurements to be made using the S-MOT fluorescence.

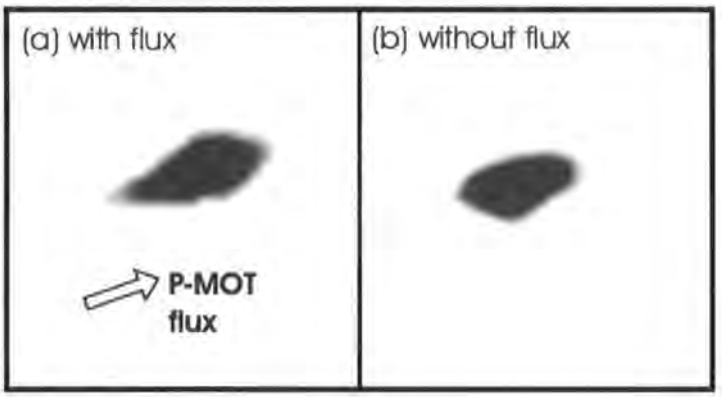

Figure 9.2: Inverted CCD image of the fluorescence from the cold atom cloud in the S-MOT. Image (a) is with the flux of cold atoms from the P-MOT present, and image (b) is without the flux and light from the P-MOT. The P-MOT flux is traveling in a north easterly direction. Each image covers approximately a 5×5 mm^2 area.

9.2.1 Fluorescence and atom number

The power emitted by the S-MOT is given by:

$$P_{\mathrm{MOT}} = \Gamma_{\mathrm{sc}} N E, \tag{9.1}$$

where Γ_{sc} is the scattering rate given by eqn. (2.9) on page 15, N is the number of atoms and $E = hc/\lambda_{\mathrm{C}}$ is the energy per photon (2.6×10^{-19} J at 780 nm).

A photodiode (Integrated Photomatrix Inc. IPL10050CW) is used to measure the fluorescence of the cold atom cloud in the S-MOT, see Figure 9.3. A pair of plano-convex 2" diameter lenses (f = 10 cm and 5 cm) focus the S-MOT light onto the photodiode. The photodiode is housed in a light tight box except

for a 1" diameter 780 nm filter (transmission $T_r = 0.65$) on the front. An OpAmp circuit provides a gain of $g_n = 50$ to the measured voltage (circuit design described in ref. [187]).

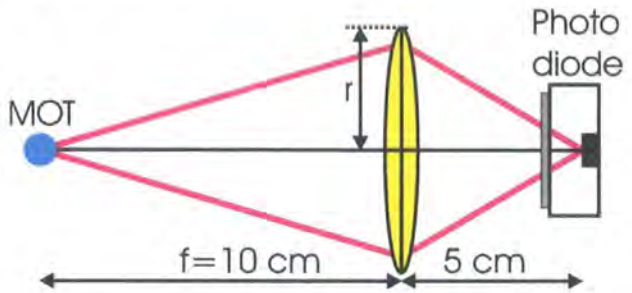

Figure 9.3: Photodiode, lens and filter used to collect S-MOT fluorescence.

The power measured by the photodiode is given by:

$$P_{PD} = \frac{V}{\kappa g_n G S T_r}, \tag{9.2}$$

where V is the voltage, G is the total impedance of the photo diode circuit ($G = 1$ MΩ) and S is the photodiode sensitivity ($S = 0.45$ A W^{-1}). The fractional solid angle for a lens of radius r and object distance f is:

$$\kappa = \frac{\pi r^2}{4\pi f^2} \simeq 0.0156. \tag{9.3}$$

Equating the two powers (eqns. (9.1) and (9.2)) gives an estimate of the atom number within the S-MOT:

$$N = \frac{V}{\kappa g_n G S T_r \Gamma_{sc} E}. \tag{9.4}$$

A voltage can therefore be converted into atom number. The majority of the terms in eqn. (9.4) are constants given by the specific photodiode setup. However, the scattering rate has an intensity and detuning dependence. In ref. [57] it was recommended that the saturation intensity for random polarisation should be used in calculating the scattering rate ($I_{sat} = 4.1$ mW/cm^2). Using eqn. (2.9), eqn. (9.4) and the values given in this section, the number of atoms per volt is estimated to be:

$$N/V = 1.5 \times 10^6 + 1.6 \times 10^{-9}\Delta^2. \tag{9.5}$$

9.2.2 Loading curves and optimisation

For a given S-MOT detuning, the atom number can be maximised by maximising the fluorescence (photodiode voltage). There are a number of parameters that can alter the final atom number captured: Rb dispenser current; shim coil currents; P-MOT current; loading time; P-MOT detuning. The remainder of this chapter optimises these parameters. Unfortunately most parameters are dependent on each other, which complicates the order of optimisation. LabVIEW was programmed to repeatedly load the S-MOT for a given time (usually 3 seconds) then release the cold atoms collected, see Figure 9.4. The average of the maximum voltage from ten loads is then plotted against the varied parameter.

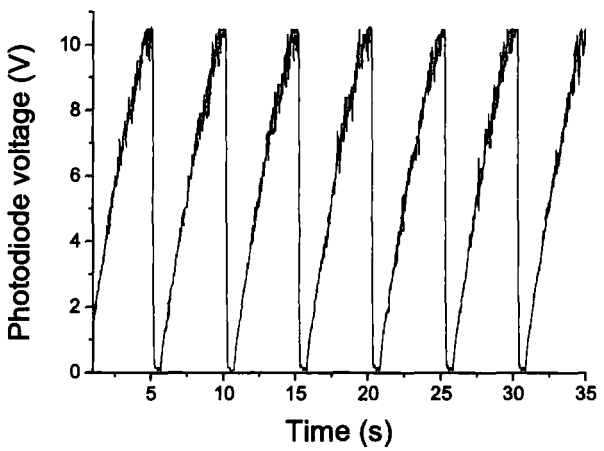

Figure 9.4: The photodiode voltage (fluorescence) from the S-MOT is plotted against time. LabVIEW was programmed to load and then release the cold atoms every 5 seconds.

The first step in optimisation is to determine the best Rb dispenser current. Figure 9.5 plots the photodiode voltage (S-MOT fluorescence) against dispenser current. Up to 2.5A the background Rb atoms create a small MOT and the dispenser does not contribute any atoms. Above the 2.5A threshold the dispenser releases Rb atoms that can be cooled in the MOT. The fluorescence begins to saturate at 3.5A. A compromise has to be made between obtaining high atom numbers and running the dispensers too hard, thus shortening their lifetime. Therefore running the dispensers at 3A was chosen.

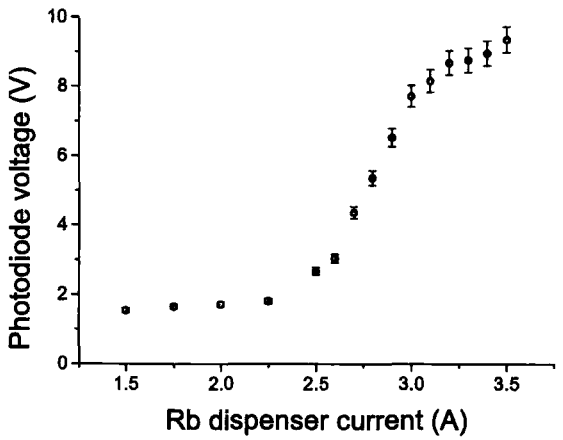

Figure 9.5: S-MOT photodiode voltage (fluorescence) is plotted against Rb dispenser current. A 3 s loading time was used.

The next stage is to optimise the position of the P-MOT cloud above the pyramid hole. By varying the current in the three independent shim coils (Up-Down, Left-Right and Forward-Back) the cloud can be moved. Figure 9.6 plots photodiode voltage against shim current for (a) the Left-Right direction and (b) the Up-Down direction.

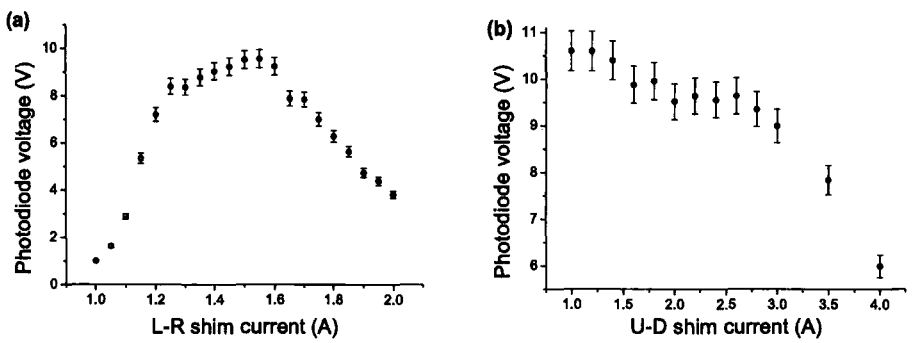

Figure 9.6: S-MOT photodiode voltage (fluorescence) is plotted against shim coil current in (a) the Left-Right direction and (b) the Up-Down direction (increasing the current lowers the cloud's position). A 3 s loading time was used.

In the Left-Right direction, the plateau between 1.25A and 1.8A is where the cloud is directly above the pyramid hole. A similar plot is obtained for the Forward-Back direction. The Up-Down plot displays a different behavior. The

fluorescence is maximised when the cloud is formed higher up in the P-MOT chamber (increasing the current lowers the cloud's position). A possible explanation for this is the higher cloud experiences more transverse cooling before exiting through the hole. A beam exiting the chamber will therefore diverge less, and produce a higher flux at the S-MOT.

Figure 9.7 plots photodiode voltage against the current in the anti-Helmholtz configuration coils on the P-MOT. The optimum fluorescence is achieved when a current of 10A is used, which corresponds to a magnetic field gradient of 5.2 G/cm.

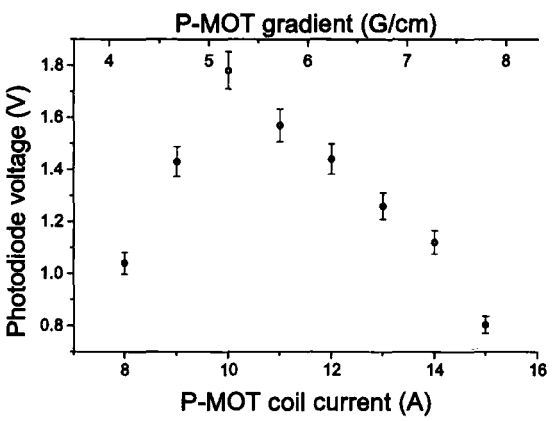

Figure 9.7: S-MOT photodiode voltage (fluorescence) is plotted against the current in the anti-Helmholtz configuration coils on the P-MOT. The corresponding magnetic field gradient is also shown on the additional x-axis. A 1 s loading time was used.

Attention is now turned to optimising the detuning of the S-MOT cooling light. As explained in Section 9.2.1, the maximum fluorescence does not necessarily correspond to the maximum atom number. Figure 9.8 (a) shows the photodiode voltage plotted against S-MOT detuning. Small detunings, being close to resonance, cause the MOT to oscillate and hence account for the large error bars on the right hand side of the figure. The maximum stable fluorescence occurs at $-2\pi \times 12.5$ MHz. The data is converted into an estimate of the atom number using eqn. 9.4, the result is plotted in Figure 9.8 (b). The maximum atom number is now achieved with a frequency detuning of $-2\pi \times 17$ MHz. Fluorescence is therefore a misleading measurement of atom number.

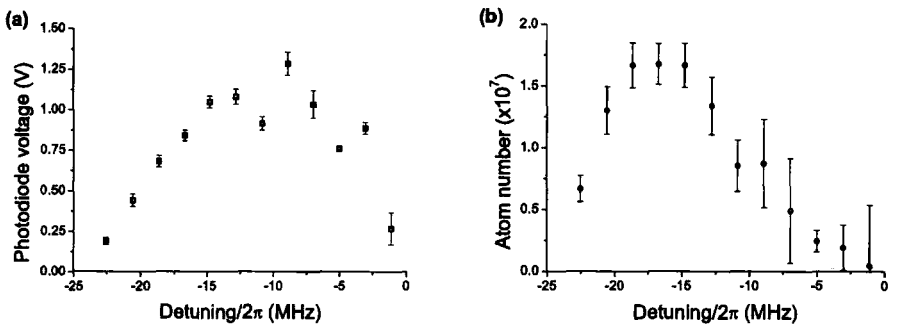

Figure 9.8: Plot (a): S-MOT photodiode voltage (fluorescence) is plotted against cooling light detuning. Plot (b): S-MOT atom number is plotted against cooling light detuning. The data from (a) are converted to atom number using eqn. 9.4. A 1 s loading time was used.

Figure 9.9, shows atom number against loading time for the now optimised S-MOT. The atom number saturates for a loading time greater than 5 seconds. 100 million cold atoms can be collected by the S-MOT. The trapping is not indefinite and Figure 9.10 shows the decay of the S-MOT fluorescence once the P-MOT flux has been extinguished. The exponential decay has a $1/e$ lifetime of 7 seconds. However, the lifetime of interest is that of the cold atoms trapped within the dipole trap. Due to the trapping light being far-off resonance, lifetimes in excess of 300 s have been measured in similar experiments [188].

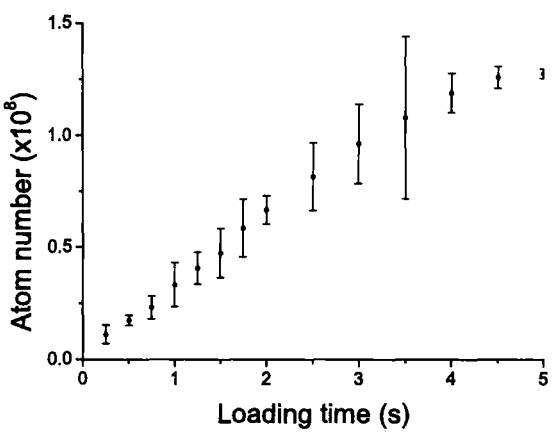

Figure 9.9: S-MOT number of atoms is plotted against loading time. The number of atoms saturates above 5 s loading time.

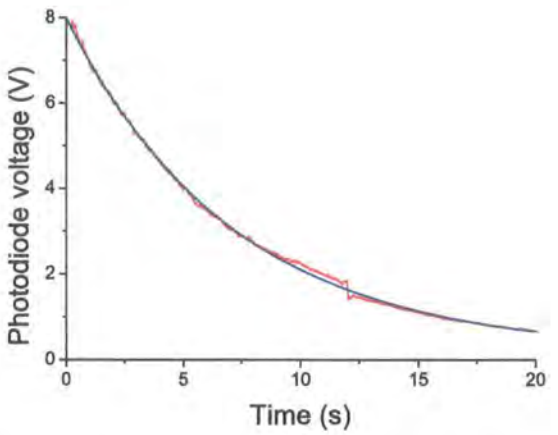

Figure 9.10: The photodiode voltage is plotted against time. The P-MOT flux was switched off at $t = 0$ s and therefore the curve represents the decay of the S-MOT fluorescence. The fitted $1/e$ lifetime (blue line) is 7.0 ± 0.5 s.

Chapter 9 summary

- An image of cold atoms fluorescing within the P-MOT was shown. The design is tolerant of misalignment and proves to be a good method of laser cooling atoms.
- A method of converting a measured fluorescence in the S-MOT to an estimate of atom number was presented. This was then used to optimise parameters to maximise the atom number collected in the S-MOT.
- 100 million atoms can be collected, and the atomic cloud has a $1/e$ lifetime of 7 seconds.

Chapter 10

Discussion and conclusions

"Begin at the beginning and go on till you come to the end; then stop."
Lewis Carroll

This chapter draws together the findings of the preceding chapters and outlines areas for future research.

10.1 Pulsed magnetic focusing

The limiting size of a focused launched cold cloud of atoms for various pulsed magnetic focusing strategies has been investigated using experimentally realistic parameters. The $\mathcal{ABCD}$ matrix formalism is convenient for giving an estimate as to the parameters needed for magnetic focusing, but does not contain the departure of the potential experienced by atoms from a perfect parabolic dependence for fields produced by real coils (and bars). In this thesis it has been shown how important it is to consider these aberrations as they drastically alter the results. The origin of these aberrations have been identified and techniques for minimising them have been described.

Single-coil lenses (Strategy I) have been discussed in Chapter 4, as well as five novel magnetic lenses (Strategies II-VI). Their performance and aberrations have been tested both analytically and numerically. For all of the strategies it was found that analytic results for aberrations (Section 4.5) tied in well with the numerical simulations of Chapter 6. It was demonstrated with Strategy II

(Strategy III) that a radially (axially) focusing lens formed from two coils with relative separation $S = 0.58$ (2.63) provided much tighter focusing than the single-coil lens (Strategy I). Amongst the isotropic 3D lenses it was found that the baseball lens (Strategy VI) was superior to the two coil lens of Strategy IV, which was in turn considerably better than the axially offset single coil lens of Strategy V. Of the single-impulse lenses, the baseball lens offers the best possibilities for isotropically focusing a cloud of weak-field-seeking atoms in 3D. Initial experiments to demonstrate the baseball lens have been conducted at Durham University [159, 158].

The loading and guiding of atoms by a far detuned laser beam has been analysed. A guided fountain is realised when atoms are launched vertically, the optical dipole force providing strong radial confinement. The axial width of the cloud grows by more than a order of magnitude. A hybrid approach using the optical dipole force for radial confinement and the Stern-Gerlach force for pulsed axial focusing was studied, and shows promise as a technique to refocus a cloud remotely into a second chamber with a smaller size than the initial sample.

Given comparable lens dimensions and strengths, double-impulse magnetic focusing is far superior to single-impulse magnetic focusing in terms of the relative density increases that can be achieved by a fraction of the atoms. This result is in stark contrast to the relative rms density increase of the entire cloud, which would lead to the opposite conclusion. If one wishes to minimise the rms image volume of a launched cloud then a single-impulse lens is preferable. If, however, one can selectively capture the central core of the bi-modal image, a double-impulse (alternate-gradient) lens can lead to orders of magnitude relative density increases for both pancake- and sausage-shaped image clouds. This spatial focusing would find applications in lithography or sending the atomic cloud through micro-sized apertures. The main application of interest for the magnetically imaged atoms will be loading a magnetic microtrap or optical dipole trap, for which alternate-gradient imaging is well-suited. Although only cold thermal atomic clouds have been considered in this thesis, the effects of aberrations will also be important for tight focusing of coherent matter waves [40, 41, 42, 189].

When loading a remote conservative trap there are three different approaches, see Figure 10.1. In the first method the atoms are launched vertically with enough kinetic energy (KE) that they overcome the potential energy barrier.

The problem with this is that when they fall down into the trap they are left with the unwanted KE. The second method avoids this by only switching the trap on once the atom cloud has come to rest at the apex of its flight. This loading can be repeated with subsequent clouds, if the trap is switched off briefly before the cloud arrives. A small fraction of the initial cloud is lost however, so a limit on the number of trapped atoms is eventually reached [76]. The third method utilises a magnetic anti-trap. When the atomic cloud reaches the centre of the anti-trap, the atomic state is switched so the atoms become trapped. The switching could be achieved by optically pumping to the opposite stretched state. Again, in this loading scheme, the problem of excess KE is avoided. If the atom's state is irreversibly flipped, the trap can accumulate atoms from subsequent clouds without suffering loss.

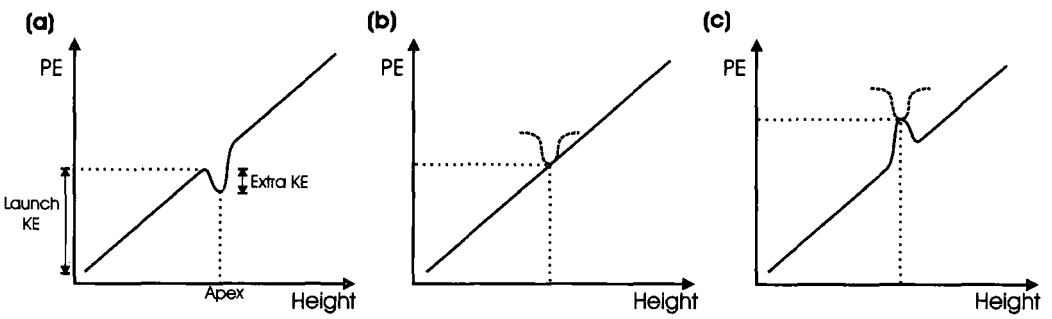

Figure 10.1: The figure depicts three different approaches to loading a trap from a guided fountain. Potential energy is plotted against height. Image (a): The trap is left on during the loading process. The atoms need sufficient energy to overcome the potential barrier, but are then left with excess kinetic energy. Image (b): The trap is switched on when the atoms have reached the flight apex. The atoms avoid having excess kinetic energy. However, the process cannot be repeated indefinitely as a maximum load is reached. Image (c): An anti-trap is created and when the atoms have reached the centre of the trap, their spins are flipped so they become trapped. The different strategies require different launch velocities.

10.1.1 Future work

The next step is to experimentally test the calculations made in this thesis. It would be good to compare the focusing properties of single-coil lenses and the optimised double-coil lenses. The lenses can then be used to construct an alternate-gradient lens system. Theory predicts a dense core at the focus, therefore an experimental cross-section through the focused cloud would reveal the atomic distribution. Finally, proof of the effectiveness of the hybrid approach of

laser guiding and magnetic lensing would be good. Magnetic lenses could also be used to help improve the atom loading efficiency of the laser guides.

10.2 3D quasi-electrostatic lattices

A quasi-electrostatic trap (QUEST) is an ideal way to store cold atoms due to the very low heating experienced (Chapter 2). The multiple states and species that can be trapped is a further benefit. A CO_2 laser acts as a QUEST for Rb atoms. The long wavelength allows optically resolvable lattices to be formed when multiple beams are overlapped (Chapter 7). In such 3D lattices there are high trap frequencies which are needed to stop motional decoherence. The above features makes a 3D lattice an ideal system to implement quantum information processing. The design of a face-centred cubic lattice experiment is given in Chapter 7. The progress in constructing and optimising the experiment have been outlined in Chapters 8 and 9. Currently cold atoms are produced in a Pyramid MOT before being moved down and recaptured in the Science MOT.

10.2.1 Future work

The short term work on the experiment involves obtaining measurements for the cold atom cloud size and temperature. This can be achieved when the Andor EMCCD camera has been installed and calibrated. Timing issues with the JAI cameras made it difficult to trigger and capture an image. The other short term aim is to trap atoms in the CO_2 laser dipole trap. A measurement of the trap lifetime can then be made. In the medium term, the priority will be the imaging and manipulation of individual sites within a 1D optical lattice. It is hoped to demonstrate enhanced loading of lattice sites with a near resonant diode laser beam superimposed on the lattice site. Two-photon Raman transitions can also be made to change the hyperfine ground state level of a site. The longer term work will involve extending the lattice to 3D and implementing two-qubit gates. There is also the option to Bose condense the atoms in individual sites. Regardless of which route is taken, there is certainly interesting physics to be discovered. The unique features of the experiment make it an ideal vehicle to travel with.

Appendix A

Abbreviations used

Abbreviation	Meaning
AOM	Acousto-optical modulator
BEC	Bose Einstein condensate
CCD	Charge coupled device
DAVLL	Dichroic atomic vapour laser lock
ECDL	External cavity diode laser
EMCCD	Electron multiplied charge couple device
LCD	Liquid crystal device
MOT	Magneto optical trap
Nd:YAG	Neodymium-doped yttrium aluminium garnet
ND	Neutral density
PBS	Polarising beam splitter
P-MOT	Pyramid magneto optical trap
QIP	Quantum Information Processing
QUEST	Quasi electrostatic
rf	Radio frequency
rms	Root mean square
RWA	Rotating wave approximation
SFS	Strong field seeking
S-MOT	Science magneto optical trap
UHV	Ultra high vacuum
WFS	Weak field seeking

Table A.1: Abbreviations and acronyms used in the thesis.

Appendix B

Symbol definitions

In Table B.1 the majority of the symbols used in the thesis are tabulated in alphabetical order with their definition. Some symbols have dual definitions but the context is sufficient to work out which one is relevant. The rules for subscripts are: i denotes an initial value; x, y, z are the Cartesian components; r is the radial component. Vectors have a bold font. Primes are used in four contexts: to distinguish 'thin lens' times from their 'thick lens' counterparts; to indicate excited states; to distinguish currents in coils and bars; to distinguish harmonic trap and laser guide angular frequencies.

Symbol	Physical meaning
α	Polarisability
α_0	Scalar polarisability
α_2	Tensor polarisability
a	Coil radius
a_0	Bohr radius
$\mathbf{a}_0$	Acceleration due to B-field gradient
$\mathbf{a}_\mathrm{F}$	Full Biot-Savart lens acceleration
$\mathbf{a}_\mathrm{H}$	Acceleration from harmonic fit to B-field
a_S	Scattering length
$\mathcal{A}, \mathcal{B}, \mathcal{C}, \mathcal{D}$	$\mathcal{ABCD}$-matrix elements
A_hfs	Hyperfine structure constant
β	Viscosity constant
$B(x, y, z)$	Magnetic field magnitude
$\mathbf{B}(x, y, z)$	Magnetic field
B_0	Bias field of magnetic field
B_1	Gradient of magnetic field
B_2	Curvature of magnetic field
B_hfs	Hyperfine structure constant
$\mathbf{BZ}(x, y, z)$	Magnetic field of current bar along z-axis

Table B.1: Symbols used and their meanings.

Symbol	Physical meaning
χ	Loading efficiency
c	Speed of light
Δ	Angular detuning ($\Delta = 2\pi\delta$)
d	Grating line spacing
$\epsilon(R, Z)$	Harmonicity
ϵ_0	Permittivity of free space
η	$\eta = \mu_0 NI/2$
E	Energy
$E(k)$	Complete elliptic integral (1st kind)
$\mathbf{E}$	Electric field
E_{hfs}	Hyperfine interaction matrix
f	Focal length of lens
$\mathcal{F}$	Fraction of atoms in the Gaussian focus
F	Total atomic angular momentum
$F_{\pm,\text{tot}}$	Scattering forces in a MOT
$\mathbf{F}_{\text{Dip}}$	Dipole force
Γ	Natural line width. Excited state decay rate.
$\Gamma(a, b, c)$	Generalised incomplete gamma function
$\Gamma_{\text{sc}}(\mathbf{r})$	Scattering rate
g	Acceleration due to gravity
g_{n}	Gain of photodiode circuit
G	Total transimpedance
h	Height
$\hbar$	Plank's constant/2π
$\mathbb{I}$	Identity matrix
I	Current in coil
I'	Current in bar
$I(\mathbf{r})$	Intensity
I_{AH}	Current in the opposite sense ($2I_{\text{AH}} = I_1 - I_2$)
I_{H}	Current in the same sense ($2I_{\text{AH}} = I_1 + I_2$)
I_{n}	Nuclear quantum number
I_{sat}	Saturation intensity
J	Total electronic angular momentum
κ	fractional solid angle
k	Substitution used in circular coil expression (eqn. (4.10))
$\mathbf{k}$	Wavevector
k_{B}	Boltzmann's constant
K	Sum of quantum numbers (eqn. (2.17))
$K(k)$	Complete elliptic integral (2nd kind)
λ	Focusing parameter (single-impulse)
$\lambda_{1,2}$	Focusing parameter (double-impulse)
λ_{C}	Wavelength of cooling laser
λ_{T}	Wavelength of trapping laser
$L = l/a$	Scaled length of current bar in baseball lens
μ_0	Permeability of free space
μ_{B}	Bohr magneton
m	Mass
m_F	Magnetic quantum number

Symbol	Physical meaning
M	System matrix
M_{ag}	Magnification
n	Density OR Diffraction order
N	Number of atoms OR coil turns
$\Phi(r,p)$	Phase space distribution
p	Radial momentum
$\mathbf{p}$	Dipole moment
P	Laser power
P_{MOT}	Power emitted by MOT
P_{PD}	Power measured by photodiode
q	Integral substitution (Section 3.3)
Q	Q-matrix
r	Polar coordinate
σ	Spatial standard deviation
σ_{el}	Collision cross section
σ_v	Velocity standard deviation
σ_R	Initial isotropic spatial standard deviation
σ_V	Initial isotropic velocity standard deviation
$S = s/a$	Scaled coil separation
S	Photodiode sensitivity
τ	Pulse duration (single-impulse)
$\tau_{1,2}$	Pulse duration (double-impulse)
θ	Angle of diffraction
t	Time
$t_{1,2}$	Time of lens pulse
T	Temperature
T_{D}	Doppler limit
T	Total focusing time
T_{osc}	Laser guide oscillation period
T_{r}	Transmission
U_{Dip}	Dipole potential
$v_{z_{\mathrm{i}}}$	Vertical launch velocity
$\mathbf{v}$	Velocity
V	Photodiode voltage
ω	Lens angular frequency (single-impulse)
ω'	Harmonic trap angular frequency
ω_0	Atomic transition angular frequency
$\omega_{1,2}$	Lens angular frequency (double-impulse)
$\omega_{r_{\mathrm{L}}}$	Laser light's angular frequency
$w(z)$	$1/e^2$ intensity radius
w_0	Beam waist
$W = w/a$	Scaled length of current bar in baseball lens
$\xi = \sigma_z/\sigma_r$	Cloud aspect ratio
x, y, z	Cartesian coordinate
X, Y, Z, R	Scaled position coordinate (eg. $X = x/a$)
z_0	Focal point
z_{c}	Vertical position of the lens centre
z_{R}	Rayleigh length

Appendix C

Values and constants

Quantity	Symbol	Value	Unit
Acceleration due to gravity	g	9.807	m s^{-2}
Atomic mass unit	u	1.661×10^{-27}	kg
Boltzmann's constant	k_B	1.381×10^{-23}	J K^{-1}
Bohr magneton	μ_B	9.274×10^{-24}	J T^{-1}
Bohr radius	a_0	5.292×10^{-11}	m
Electron charge	e	1.602×10^{-19}	C
Electron mass	m_e	9.109×10^{-31}	kg
Permeability of free space	μ_0	$4\pi \times 10^{-7}$	N A^{-2}
Permittivity of free space	ϵ_0	8.854×10^{-12}	F m^{-1}
Planks constant/2π	$\hbar$	1.055×10^{-34}	J s
Speed of light in a vacuum	c	2.999×10^{8}	m s^{-1}
Rubidium natural linewidth [126]	Γ	$2\pi \times 5.9$	MHz
Hyperfine structure constants [132]	A_{hfs}	$2\pi \times 25.009$	MHz
	B_{hfs}	$2\pi \times 25.88$	MHz
D2 line wavelength [123]	λ_C	780.24	nm

Table C.1: Values and constants used. Values for the fundamental constants are the CODATA recommended values [190].

Appendix D

Atomic structure of Rb

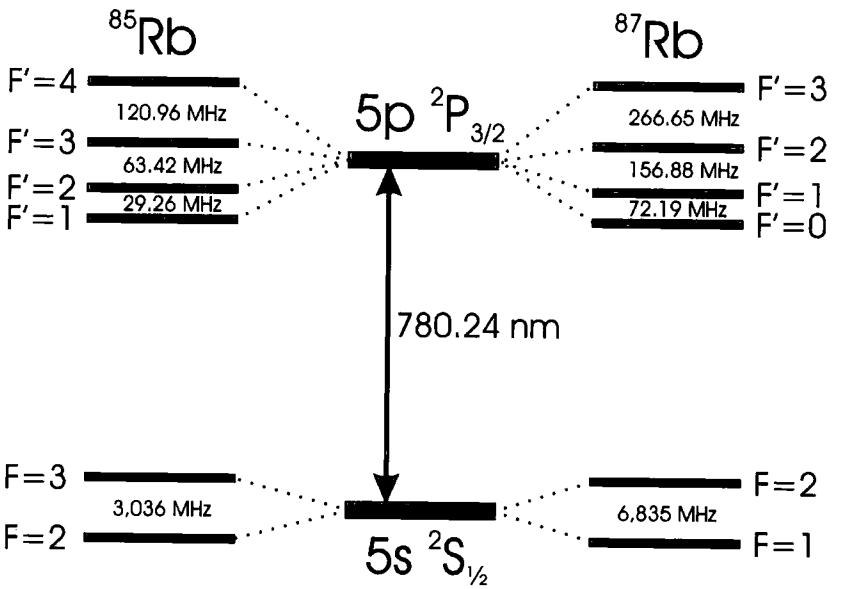

Figure D.1: The hyperfine energy level diagram on the D2 line for the ^{85}Rb and ^{87}Rb isotopes [191, 192].

Appendix E

Collision rate

Following the approach taken in ref. [154] to calculate the collision rate within a MOT. The density of a spherically symmetric Gaussian spatial distribution with N atoms and a spatial standard deviation of σ_R is:

$$n(\mathbf{r}) = n_0 \exp\left(-\frac{x^2+y^2+z^2}{2{\sigma_R}^2}\right), \tag{E.1}$$

where the peak density is:

$$n_0 = \frac{N}{(2\pi)^{3/2}{\sigma_R}^3}. \tag{E.2}$$

The spatially averaged elastic collision rate is:

$$\begin{aligned}\Gamma_{\text{el}} &= \sigma_{\text{el}} \frac{\int n^2(\mathbf{r}) v_{\text{rel}}\, d^3r}{\int n(\mathbf{r})\, d^3r} = \sigma_{\text{el}} \langle n \rangle \langle v_{\text{rel}} \rangle, \\ &= \sigma_{\text{el}}\, n_0 \sqrt{\frac{3k_{\text{B}}\mathcal{T}}{4m}},\end{aligned} \tag{E.3}$$

where the density-weighted density for a Gaussian distribution is $\langle n \rangle = n_0/\sqrt{8}$ and the rms average velocity between atoms of mass m is $\langle v_{\text{rel}} \rangle = \sqrt{6k_{\text{B}}\mathcal{T}/m}$. The dominant collision at ultracold temperatures is s-wave elastic collisions:

$$\sigma_{\text{el}} = \frac{8\pi {a_{\text{S}}}^2}{1 + k^2 {a_{\text{S}}}^2}, \tag{E.4}$$

where $k = \sqrt{2\pi m k_{\text{B}}\mathcal{T}}/\hbar$ and a_{S} is the scattering length. Combining eqns. (E.2), (E.3) and (E.4), and using the experimentally measured ^{85}Rb background scattering length $a_{\text{S}} = -433\ a_0$ from ref. [193], the MOT average collision rate is: $\Gamma_{\text{el}} = 3\ \text{s}^{-1}$.

Appendix F

Mathematica computer code

Below is an example *Mathematica* computer code that calculates the trajectories of atoms passing along a laser guide.

Define fundamental constants.

```
Bohr = 0.5292 * 10^-10;
c = 2.999 * 10^8; g = 9.807;
kb = 1.381 * 10^-23; m = 85 x 1.661 x 10^-27;
```

Calculate the laser beam potential using the ground state polarisability of Rb.

```
waist = 250 * 10^-6; z0 = 0.0;
λ = 1064 * 10^-9; ray = π waist^2 / λ;
power = 19;
wl[z_] := waist Sqrt[1 + (z - z0)^2 / ray^2];
int[r_, z_] = 2 * power / (π wl[z]^2) Exp[-2 (r / wl[z])^2];
α0 = 693.5;
U0 = α0 * 4 * Pi / (2 c) Bohr^3;
U[x_, y_, z_] := -U0 int[Sqrt[x^2 + y^2], z];
```

Calculate the acceleration due to the dipole potential. The dummy variables used in the differentiation are replaced with the correct coordinate at the end.

```
(*Calculates acceleration on atoms*)
accx[x_, y_, z_] = -D[U[ρ, y, z], ρ] / m /. {ρ → x} // Evaluate // Simplify;
accy[x_, y_, z_] = -D[U[x, ϒ, z], ϒ] / m /. {ϒ → y} // Evaluate // Simplify;
accz[x_, y_, z_] = -D[U[x, y, ζ], ζ] / m /. {ζ → z} // Evaluate // Simplify;
```

Setup the Gaussian spatial and velocity distributions for the atomic sample. Table "mix1" contains the x-direction data, "mix2" y-direction and "mix3" z-direction.

```
atoms = 25;
cloudradius = 0.0002;
temp = 20 * 10^-6; thermalvel = Sqrt[kb * (temp / m)];
<< "Statistics`NormalDistribution`"
ndistpos := Random[NormalDistribution[0, cloudradius]];
ndistvel := Random[NormalDistribution[0, thermalvel]];
xcom = 10^-8; xvcom = 0; ycom = 10^-8; yvcom = 0; zcom = 0;
mix1 = Table[{xcom + ndistpos, xvcom + ndistvel}, {atoms}];
mix2 = Table[{ycom + ndistpos, yvcom + ndistvel}, {atoms}];
mix3 = Table[{zcom + ndistpos, ndistvel}, {atoms}];
```

Calculate the launch velocity and flight duration based on a given height.

```
height = 0.22;
zvcom = Sqrt[2 * g * height];
tfocus = Sqrt[(2 * height) / g];
tmx = 0.02 + tfocus;
```

The equations of motion for the system. *Mathematica* produces interpolating functions for each atom. Only the x-direction table is generated in this example.

```
Clear[Coord];
Coord[xpos_, xvel_, ypos_, yvel_, zpos_, zvel_] :=
  Coord[xpos, xvel, ypos, yvel, zpos, zvel] =
   NDSolve[{vx'[t] == accx[x[t], y[t], z[t]], x'[t] == vx[t], vx[0] == xvel, x[0] == xpos,
     vy'[t] == accy[x[t], y[t], z[t]], y'[t] == vy[t], vy[0] == yvel, y[0] == ypos,
     vz'[t] == accz[x[t], y[t], z[t]] - g, z'[t] == vz[t], vz[0] == zvel, z[0] == zpos},
    {x[t], vx[t], y[t], vy[t], z[t], vz[t]}, {t, 0, tmx}, MaxSteps → 10000];

xtraj = Table[{x[t] - (xvcom * t + xcom) /.
      Coord[mix1[[shelf, 1]], mix1[[shelf, 2]], mix2[[shelf, 1]], mix2[[shelf, 2]],
       mix3[[shelf, 1]], mix3[[shelf, 2]] + zvcom]}[[1]], {shelf, 1, atoms}];
```

Plots the x position against time and generates a data table that can be further analysed or exported.

```
Plot[Evaluate[xtraj], {t, 0, tmx}]; dt = 2000;
xstatdata = Table[Evaluate[Flatten[xtraj]], {t, 0, tmx, 1 / dt}];
```

Appendix G

Fibre optic alignment

Due to the elliptical cross-section, polarisation preserving fibre optics will only function properly if the incoming linearly polarised light is aligned to one of the two orthogonal axes running along the fibre (semi-major or semi-minor axis). If the axes are not marked, a simple way to determine the correct polarisation is outlined in this Appendix. The experimental setup is shown in Figure G.1.

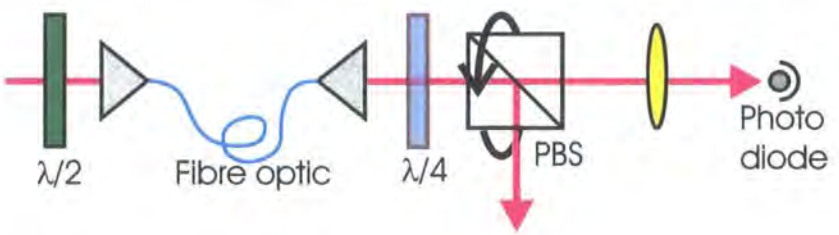

Figure G.1: Experimental setup used to align the polarisation of light going into the fibre optics. The $\lambda/4$ waveplate is only used when converting the light into circular polarisation.

The initial alignment does not make use of the $\lambda/4$ waveplate. A rotatable polarising beam splitting (PBS) cube is used with a either a photodiode or power meter (Coherent Field Master) to analyse the polarisation of the light exiting the fibre. The PBS cube is rotated to obtain values for the maximum and minimum powers measured by the photodiode. The signature of linear light exiting from the fibre optic is that the ratio of maximum power to minimum power is maximised. The initial $\lambda/2$ waveplate is used to rotate the polarisation of the light entering the fibre. A plot of the max/min power ratio against $\lambda/2$ waveplate rotation angle is given in Figure G.2 (a). As expected from the 2θ rotation property of the waveplate, one finds a maximum every 45°. A close-up of the first maximum is shown in Figure G.2 (b).

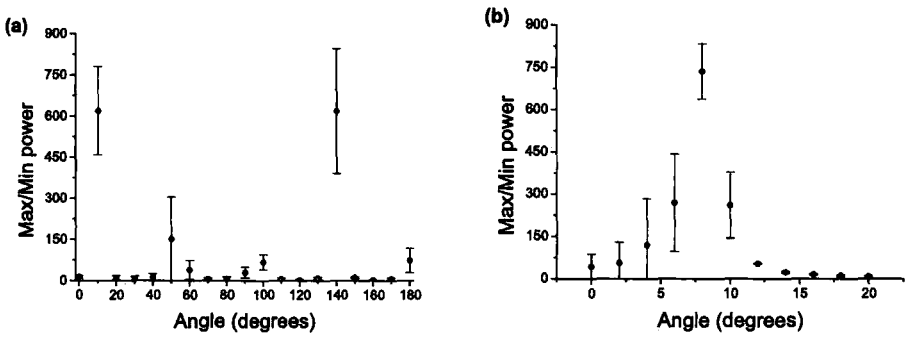

Figure G.2: The maximum to minimum power ratio is plotted against $\lambda/2$ waveplate angle. Plot (b) examines the first maximum in (a).

The correct angle of a $\lambda/4$ waveplate to convert linear light into circular polarisation can be similarly determined. In this case the $\lambda/4$ waveplate is rotated and the ratio of minimum to maximum power is plotted, see Figure G.3. In this case the waveplate is set to one of the maximum angles.

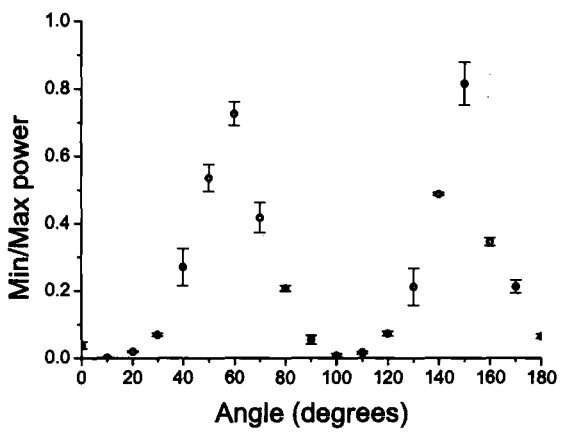

Figure G.3: The minimum to maximum power ratio is plotted against $\lambda/4$ waveplate angle.

Another method to align the linear polarisation into the fibre that does not involve rotating the PBS cube is to plot the peak-to-peak noise on the photodiode voltage against the rotation angle of the $\lambda/2$ waveplate. During the measurement, the fibre is deliberately stressed and heated by gently massaging the fibre. When the light is propagating down one of the orthogonal axes the effect of the perturbation is minimised and is seen by a dramatic reduction in the photodiode noise.

Appendix H

Knife edge measurements

A crude, but nonetheless effective, method of measuring a laser beam's profile is now described. A knife edge is translated through the beam's cross-section. The resulting change in power as a function of knife edge position allows the $1/e^2$ beam radius $w(z)$ to be calculated (see Section 3.1). Multiple readings at different z positions allow a full description of the laser beam's spatial profile. Treating the x- and y-direction beam waists as being independent i.e. an elliptical beam profile, the total power in the beam is given by integrating eqn. (3.1) on page 26:

$$P_{total} = \int_{-\infty}^{\infty}\int_{-\infty}^{\infty} I(x,y)dydx = \frac{\pi}{2} I_0 w_x w_y. \tag{H.1}$$

As the knife edge moves across the beam in the x-direction the power measured at the photodiode varies as:

$$P(X) = P_{total} - \int_{-\infty}^{X}\int_{-\infty}^{\infty} I(x,y)dydx. \tag{H.2}$$

After integration and substituting in the error function:

$$\mathrm{erf}(u) = \frac{2}{\sqrt{\pi}}\int_0^u e^{-u^2}\,du\,, \tag{H.3}$$

the power measured by the photodiode vs. knife edge position, X, will have the following form:

$$P(X) = \frac{P_{total}}{2}\left(1 - \mathrm{erf}\left(\frac{\sqrt{2}\,X}{w_x}\right)\right). \tag{H.4}$$

An example of this measurement can be found in Figure H.1. The data were recorded by translating the knife edge through one of the three arms of the

S-MOT cooling beams; see Figure 8.22. A fit to the data gives the $1/e^2$ beam radius as 7.5 mm and the peak intensity as 7.1 mW/cm^2.

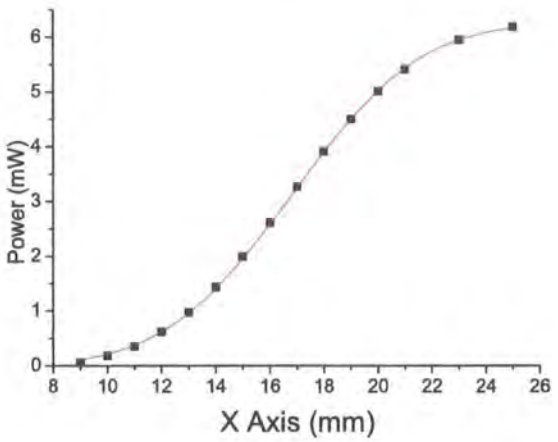

Figure H.1: Knife edge measurement of the S-MOT laser beam.

Bibliography

[1] S. Chu, C. N. Cohen-Tannoudji, and W. D. Phillips, Rev. Mod. Phys. **70**, 707 (1998).

[2] C. S. Adams and E. Riis, Prog. Quant. Electr. **21**, 1 (1997).

[3] http://www.uibk.ac.at/exphys/ultracold/atomtraps.html.

[4] E. A. Cornell and C. E. Wieman, Rev. Mod. Phys. **74**, 875 (2002).

[5] W. Ketterle, Rev. Mod. Phys. **74**, 1131 (2002).

[6] B. DeMarco and D. S. Jin, Science **285**, 1703 (1999).

[7] D. Budker *et al.*, Rev. Mod. Phys. **74**, 1153 (2002).

[8] B. Levy, Phys. Today **44**, 17 (1991).

[9] J. Helmcke, F. Riehle, A. Witte, and T. Kisters, Phys. Scripta **T40**, 32 (1992).

[10] F. G. Major, *The Quantum Beat: The Physical Principles of Atomic Clocks* (Springer-Verlag, New York, 1998).

[11] C. Salomon *et al.*, C. R. Acad. Sci. Paris. **Serie IV**, 1313 (2001).

[12] H. J. Briegel, T. Calarco, D. Jaksch, J. Cirac, and P. Zoller, J. Mod. Opt. **47**, 415 (2000).

[13] M. A. Nielson and I. L. Chuang, *Quantum Computation and Quantum Information* (CUP, Cambridge, 2000).

[14] A. M. Steane, Appl. Phys. B. **64** (1997).

[15] C. S. Adams, M. Sigel, and J. Mlynek, Phys. Rep. **240**, 143 (1994).

[16] V. I. Balykin and W. Jhe, J. Korean Phys. Soc. **37**, 654 (2000).

[17] N. F. Ramsey, *Molecular beams* (Oxford, OUP, 1985).

[18] L. Estermann and O. Stern, Z. Phys. **61**, 95 (1930).

[19] O. R. Frish and O. Stern, Z. Phys **84**, 430 (1933).

[20] D. W. Keith, M. L. Schattenburg, H. I. Smith, and D. E. Pritchard, Phys. Rev. Lett. **61**, 1580 (1988).

[21] O. Carnal, M. Sigel, T. Sleator, H. Takuma, and J. Mlynek, Phys. Rev. Lett. **67**, 3231 (1991).

[22] J. J. Berkhout, O. J. Luiten, I. D. Setija, T. Mizusaki, and J. T. M. Walraven, Phys. Rev. Lett. **63**, 1689 (1989).

[23] B. Holst and W. Allison, Nature **390**, 244 (1997).

[24] R. J. Wilson, B. Holst, and W. Allison, Rev. Sci. Instrum. **70**, 2960 (1999).

[25] J. P. Gordon, H. J. Zeiger, and C. Townes, Phys. Rev. **99**, 1264 (1955).

[26] J. A. Maddi, T. P. Dinneen, and H. Gould, Phys. Rev. A **60**, 3882 (1999).

[27] H. B. Bethlem and G. Meijer, Int. Rev. Phys. Chem. **22**, 73 (2003).

[28] M. R. Tarbutt *et al.*, Phys. Rev. Lett. **92**, 173002 (2004).

[29] H. L. Bethlem *et al.*, J. Phys. B **39**, R263 (2006).

[30] J. J. Hudson, B. E. Sauer, M. R. Tarbutt, and E. A. Hinds, Phys. Rev. Lett. **89**, 023003 (2002).

[31] E. A. Hinds and I. G. Hughes, J. Phys. D **32**, R119 (1999).

[32] T. M. Roach *et al.*, Phys. Rev. Lett. **75**, 629 (1995).

[33] A. I. Sidorov *et al.*, Quantum Semiclass. Opt. **8**, 713 (1996).

[34] D. C. Lau *et al.*, Eur. Phys. J. D **5**, 193 (1999).

[35] I. G. Hughes, P. A. Barton, T. M. Roach, M. G. Boshier, and E. A. Hinds, J. Phys. B **30**, 647 (1997).

[36] I. G. Hughes, P. A. Barton, T. M. Roach, and E. A. Hinds, J. Phys. B **30**, 2119 (1997).

[37] I. G. Hughes, T. Darlington, and E. A. Hinds, J. Phys. B **34**, 2869 (2001).

[38] C. V. Saba *et al.*, Phys. Rev. Lett. **82**, 468 (1999).

[39] D. Kadio, O. Houde, and L. Pruvost, Europhys. Lett. **54**, 417 (2001).

[40] I. Bloch, M. Köhl, M. Greiner, T. W. Hänsch, and T. Esslinger, Phys. Rev. Lett. **87**, 030401 (2001).

[41] A. S. Arnold, C. MacCormick, and M. G. Boshier, Phys. Rev. A **65**, 031601(R) (2002).

[42] A. S. Arnold, C. MacCormick, and M. G. Boshier, J. Phys. B **37**, 485 (2004).

[43] P. Rosenbusch, B. V. Hall, I. G. Hughes, C. V. Saba, and E. A. Hinds, Phys. Rev. A **61**, 031404 (2000).

[44] P. Rosenbusch, B. V. Hall, I. G. Hughes, C. V. Saba, and E. A. Hinds, Appl. Phys. B **70**, 709 (2000).

[45] H. Friedburg and W. Paul, Naturwissenschaft **38**, 159 (1951).

[46] H. Friedburg, Z. Phys. **130**, 493 (1951).

[47] H. Metcalf, W. Philips, and J. Prodan, Bull. Am. Phys. Soc. **29**, 785 (1984).

[48] W. G. Kaenders *et al.*, Phys. Rev. A **54**, 5067 (1996).

[49] E. A. Cornell, C. Monroe, and C. E. Wieman, Phys. Rev. Lett. **67**, 2439 (1991).

[50] E. Maréchal *et al.*, Eur. Phys. J. D **2**, 195 (1998).

[51] E. Maréchal *et al.*, Phys. Rev. A **59**, 4636 (1999).

[52] T. Miossec, R. Barbé, J. C. Keller, and O. Gorceix, Opt. Commun. **209**, 349 (2002).

[53] S. H. Myrskog, J. K. Fox, H. S. Moon, J. B. Kim, and A. M.Steinberg, Phys. Rev. A **61**, 053412 (2000).

[54] T. Aoki, T. Kato, Y. Tanami, and H. Nakamatsu, Phys. Rev. A **73**, 063603 (2006).

[55] S. Goldberg *et al.*, Phys. Rev. A **68**, 043410 (2003).

[56] M. Greiner, I. Bloch, T. W. Hänsch, and T. Esslinger, Phys. Rev. A **63**, 031401 (2001).

[57] H. J. Lewandowski, D. M. Harber, D. L. Whitaker, and E. A. Cornell, J. Low Temp. Phys. **132**, 309 (2003).

[58] J. Goldwin, M. L. Olsen, B. Newman, B. D. DePaola, and D. S. Jin, Phys. Rev. A **70**, 021 601(R) (2004).

[59] K. Nakagawa, Y. Suzuki, M. Horikoshi, and J. Kim, Appl. Phys. B **81**, 791 (2005).

[60] T. Lahaye, G. Reinaudi, Z. Wang, A. Couvert, and D. Guéry-Odelin, arXiv:cond-mat , 0605302 (2006).

[61] T. W. Hansch and A. L. Schawlow, Opt. Comm. **13**, 68 (1975).

[62] D. Wineland and H. Dehmelt, Bull. Am. Phys. Soc. **20**, 637 (1975).

[63] S. Chu, L. Hollberg, J. E. Bjorkholm, A. Cable, and A. Ashkin, Phys. Rev. Lett **55**, 48 (1985).

[64] E. L. Raab, M. Prentiss, A. Cable, S. Chu, and D. E. Pritchard, Phys. Rev. Lett. **59**, 2631 (1987).

[65] G. A. Askar'yan, Sov. Phys. JETP **15**, 1088 (1962).

[66] V. S. Letokhov, JETP Lett. **7**, 272 (1968).

[67] A. Ashkin, Phys. Rev. Lett. **24**, 156 (1970).

[68] A. Ashkin, Phys. Rev. Lett. **40**, 729 (1978).

[69] J. E. Bjorkholm, R. E. Freeman, A. A. Ashkin, and D. B. Pearson, Phys. Rev. Lett. **41**, 1361 (1978).

[70] S. Chu, J. E. Bjorkholm, A. Ashkin, and A. Cable, Phys. Rev. Lett **56**, 314 (1986).

[71] T. Sleator, T. Pfau, V. Balykin, O. Carnal, and J. Mlynek, Appl. Phys. B **54**, 375 (1992).

[72] M. A. Kasevich, D. S. Weiss, and S. Chu, Opt. Lett. **15**, 607 (1990).

[73] C. G. Aminoff *et al.*, Phys. Rev. Lett. **71**, 3083 (1993).

[74] K. Szymaniec, H. J. Davies, and C. S. Adams, Europhys. Lett. **45**, 450 (1999).

[75] H. J. Davies and C. S. Adams, J. Phys. B **33**, 4079 (2000).

[76] H. J. Davies, K. Szymaniec, and C. S. Adams, Phys. Rev. A **62**, 013412 (2000).

[77] L. Pruvost, D. Marescaux, O. Houde, and H. T. Duong, Opt. Comm. **166**, 199 (1999).

[78] H. R. Noh, X. Xu, and W. Jhe, Adv. At. Mol. Opt. Phys. **48**, 153 (2002).

[79] D. P. Rhodes *et al.*, J. Mod. Opt. **53**, 547 (2006).

[80] M. J. Renn *et al.*, Phys. Rev. Lett. **75**, 3253 (1995).

[81] M. J. Renn, E. A. Donley, E. A. Cornell, C. E. Wieman, and D. Z. Anderson, Phys. Rev. A **53**, R648 (1996).

[82] M. J. Renn, A. A. Zozulya, E. A. Donely, E. A. Cornell, and D. Z. Anderson, Phys. Rev. A **55**, 3684 (1997).

[83] H. Ito, K. Sakaki, M. Ohtsu, and W. Jhe, Appl. Phys. Lett. **70**, 2496 (1997).

[84] T. L. Gustavson *et al.*, Phys. Rev. Lett. **88**, 020401 (2001).

[85] J. P. Dowling and J. Gea-Banacloche, Adv. At. Mol. Opt. Phys. **36**, 1 (1996).

[86] V. I. Balykin, Adv. At. Mol. Opt. Phys. **41**, 181 (1999).

[87] R. Grimm, M. Weidemuller, and Y. B. Ovchinnikov, Adv. Atom. Mol. Phys. **42**, 95 (2000).

[88] J. D. Miller, R. A. Cline, and D. J. Heinzen, Phys. Rev. A **47**, R4567 (1993).

[89] T. Takekoshi, J. R. Yeh, and R. J. Knize, Opt. Comm. **114**, 421 (1995).

[90] T. Takekoshi and R. J. Knize, Optics Lett. **21**, 77 (1996).

[91] A. Mosk, S. Kraft, and M. Mudrich, Appl. Phys. B **73**, 791 (2001).

[92] M. Mudrich *et al.*, Phys. Rev. Lett. **88**, 253001 (2002).

[93] R. Scheunemann, F. S. Cataliotti, T. W. Hänsch, and M. Weitz, Phys. Rev. A **62**, 051801 (2000).

[94] R. Scheunemann, F. S. Cataliotti, T. W. Hänsch, and M. Weitz, J. Opt. B. **2**, 645 (2000).

[95] C. S. Adams, H. J. Lee, N. Davidson, M. Kasevich, and S. Chu, Phys. Rev. Lett. **74**, 3577 (1995).

[96] W. Ketterle and N. J. van Druten, Adv. At. Mol. Opt. Phys. **37**, 181 (1996).

[97] M. D. Barrett, J. A. Sauer, and M. S. Chapman, Phys. Rev. Lett. **87**, 010404 (2001).

[98] K. M. O'Hara, M. E. Gehm, S. R. Granade, and J. E. Thomas, Phys. Rev. A **64**, 051403(R) (2001).

[99] T. Weber, J. Herbig, M. Mark, H. C. Nägerl, and R. Grimm, Science **299**, 232 (2003).

[100] D. J. Han, M. T. DePue, and D. S. Weiss, Phys. Rev. A **63**, 023405 (2001).

[101] T. Kinoshita, T. Wenger, and D. S. Weiss, Phys Rev. A **71**, 011602(R) (2005).

[102] D. Rychtarik, B. Engeser, and H. C. Nägerl, Phys. Rev. Lett. **92**, 173003 (2004).

[103] Y. Takasu *et al.*, Phys. Rev. Lett. **90**, 023003 (2003).

[104] A. Marte *et al.*, Phys. Rev. Lett. **89**, 283202 (2002).

[105] P. S. Jessen and I. H. Deutsch, Adv. At. Mol. Opt. Phys. **37**, 95 (1996).

[106] L. Guidoni and P. Verkerk, J. Opt. B **1**, R23 (1999).

[107] M. Greiner, O. Mandel, T. Esslinger, T. W. Hänsch, and I. Bloch, Nature **415**, 39 (2002).

[108] O. Mandel *et al.*, Phys. Rev. Lett. **91**, 010407 (2003).

[109] S. Peil *et al.*, Phys. Rev. A **67**, 051603(R) (2003).

[110] R. Folman, P. Kruger, J. Schmiedmayer, J. Denschlag, and C. Henkel, Adv. At. Mol. Opt. Phys. **48**, 263 (2002).

[111] J. Reichel, Applied Physics B **74**, 469 (2002).

[112] D. Müller, D. Z. Anderson, R. J. Grow, P. D. D. Schwindt, and E. A. Cornell, Phys. Rev. Lett. **83**, 5194 (1999).

[113] N. H. Dekker *et al.*, Phys. Rev. Lett. **84**, 1124 (2000).

[114] M. Key *et al.*, Phys. Rev. Lett. **84**, 1371 (2000).

[115] J. A. Sauer, M. D. Barrett, and M. S. Chapman, Phys. Rev. Lett. **87**, 270401 (2001).

[116] S. Wu, W. Rooijakkers, P. Striehl, and M. Prentiss, Phys. Rev. A **70**, 013409 (2004).

[117] D. Meschede and H. Metcalf, J. Phys. D **36**, R17 (2003).

[118] D. P. DiVincenzo, Fortschr. Phys. **48**, 771 (2000).

[119] Neutral atom approaches to quantum information processing and quantum computing, http://qist.lanl.gov/pdfs/neutral_atom.pdf.

[120] P. F. Griffin, K. J. Weatherill, S. G. MacLeod, R. M. Potvliege, and C. S. Adams, New J. Phys. **8**, 11 (2006).

[121] G. K. Brennen, C. M. Caves, P. S. Jessen, and I. H. Deutsch, Phys. Rev. Lett. **82**, 1060 (1999).

[122] D. Jaksch, Contemporary Physics **45**, 367 (2004).

[123] H. J. Metcalf and P. van der Straten, *Laser cooling and trapping* (Springer-Verlag, New York, 1999).

[124] I. G. Hughes and M. J. Pritchard, Cool things to do with lasers, Accepted for publication in Physics Education.

[125] C. Cohen-Tannoudji, J. Dupont-Roc, and G. Grynberg, *Atom-Photon Interactions* (Wiley, 1998).

[126] U. Volz and H. Schmoranzer, Physica Scripta Volume T **65**, 48 (1996).

[127] J. Dalibard and C. Cohen-Tannoudji, J. Opt. Soc. Am. B **6**, 2023 (1989).

[128] G. K. Woodgate, *Elementary Atomic Structure*, Second ed. (Clarendon press, Oxford, 1983).

[129] J. R. P. Angel and P. G. H. Sanders, Proc. Roy. Soc. A. **305**, 125 (1968).

[130] R. W. Schmieder, Am. J. Phys. **40**, 297 (1972).

[131] C. Schwarz, Phys. Rev. **97**, 380 (1955).

[132] E. Arimondo, M. Inguscio, and P. Violino, Rev. Mod. Phys. **49**, 31 (1977).

[133] F. L. Kien, V. I. Balykin, and K. Hakuta, J. Phys. Soc. Jpn. **74**, 910 (2005).

[134] A. R. Edmonds, *Angular Momentum in Quantum Mechanics*, 2nd ed. (Princeton University Press, Princeton, 1996).

[135] K. D. Bonin and M. A. Kadar-Kallen, Phys. Rev. A **47**, 944 (1993).

[136] M. Marinescu, H. R. Sadeghpour, and A. Dalgarno, Phys. Rev. A **49**, 5103 (1994).

[137] M. S. Safronova, W. R. Johnson, and A. Derevianko, Phys. Rev. A **60**, 4476 (1999).

[138] S. Magnier and M. Aubert-Frécon, J. Quant. Spect. Rad. Trans. **75**, 121 (2002).

[139] C. Zhu, A. Dalgarno, S. G. Porsev, and A. Derevianko, Phys. Rev. A **70**, 032722 (2004).

[140] M. S. Safronova, C. J. Williams, and C. W. Clark, Phys. Rev. A **69**, 022509 (2004).

[141] M. J. Pritchard *et al.*, Transport of launched cold atoms with a laser guide and pulsed magnetic fields, In preparation.

[142] P. D. Lett *et al.*, J. Opt. Soc. Am. B **6**, 2084 (1989).

[143] B. T. Wolschrijn, R. A. Cornelussen, R. J. C. Spreeuw, and H. B. van Linden van den Heuvell, New J. Phys. **4**, 69 (2002).

[144] T. W. B. Kibble and F. H. Berkshire, *Classical Mechanics*, 4th ed. (Addison Wesley Longman, London, 1996).

[145] M. J. Pritchard, D. A. Smith, A. S. Arnold, and I. G. Hughes, J. Phys. B **37**, 4435 (2004).

[146] A. S. Arnold, M. J. Pritchard, D. A. Smith, and I. G. Hughes, New J. Phys. **8**, 53 (2006).

[147] W. Petrich, M. H. Anderson, J. R. Ensher, and E. A. Cornell, Phys. Rev. Lett. **74**, 3352 (1995).

[148] S. Earnshaw, Trans. Cambridge Philos. Soc. **7**, 97 (1842).

[149] W. H. Wing, Prog. Quant. Electr. **8**, 181 (1984).

[150] W. R. Smythe, *Static and Dynamic Electricity*, 3rd edition ed. (McGraw-Hill, New York, 1968), eqns. (5) and (6).

[151] T. Bergeman, G. Erez, and H. J. Metcalf, Phys. Rev. A **35**, 1535 (1987).

[152] Y. V. Gott, M. S. Ioffe, and V. G. Tel'kovskii, Nucl. Fusion Suppl. **3**, 1045 (1962).

[153] D. E. Pritchard, Phys. Rev. Lett. **51**, 1336 (1983).

[154] A. S. Arnold, PhD thesis, University of Sussex, (1999).

[155] J. D. Lawson, *The Physics of Charged Particle Beams* (OUP, Oxford, 1977).

[156] H. R. Noh, K. Shimizu, and F. Shimizu, Phys. Rev. A **61**, 041601(R) (2000).

[157] W. Ketterle and D. E. Pritchard, Phys. Rev. A **46**, 4051 (1992).

[158] D. A. Smith, M. J. Pritchard, A. S. Arnold, and I. G. Hughes, Experimental single-impulse magnetic focusing of launched cold atoms, In preparation.

[159] D. A. Smith, PhD thesis, University of Durham, (2005).

[160] W. Ketterle, K. B. Davis, M. A. Joffe, A. Martin, and D. E. Pritchard, Phys. Rev. Lett. **70**, 2253 (1993).

[161] K. I. Petsas and G. Grynberg, Phys. Rev. A **50**, 5173 (1994).

[162] C. S. Adams, S. G. Cox, E. Riis, and A. S. Arnold, J. Phys. B **36**, 1933 (2003).

[163] K. J. Weatherill, PhD thesis, University of Durham, (2006).

[164] J. J. Arlt, O. Marago, S. Webster, S. Hopkins, and C. J. Foot, Opt. Comm. **157**, 303 (1998).

[165] R. S. Williamson, P. A. Voytas, R. T. Newell, and T. Walker, Opt. Exp. **3**, 111 (1998).

[166] S. G. Cox, P. F. Griffin, C. S. Adams, D. DeMille, and E. Riis, Rev. Sci. Instrum. **74**, 3185 (2003).

[167] W. M. Frix, G. G. Karady, and B. A. Venetz, IEEE Trans. Power Delivery **9**, 100 (1994).

[168] M. Misakian, J. Res. Natl. Inst. Stand. Technol. **105**, 557 (2000).

[169] C. E. Wieman and L. Hollberg, Rev. Sci. Instrum. **62**, 1 (1991).

[170] L. Ricci *et al.*, Opt. Comm. **117**, 541 (1995).

[171] A. S. Arnold, J. S. Wilson, and M. G. Boshier, Rev. Sci. Instrum. **69**, 1236 (1998).

[172] M. W. Hamilton, Contemp. Phys. **30**, 21 (1989).

[173] G. D. Rovera, G. Santarelli, and A. Clairon, Rev. Sci. Instrum. **65**, 1502 (1994).

[174] W. Demtroder, *Laser Spectroscopy: Basic concepts and instrumentation*, 2nd ed. (Springer-Verlag, New York, 1996).

[175] D. A. Smith and I. G. Hughes, Am. J. Phys. **72**, 631 (2004).

[176] C. P. Pearman *et al.*, J. Phys. B **35**, 5141 (2002).

[177] A. Ratnapala *et al.*, Opt. Lett. **29**, 2704 (2004).

[178] M. L. Harris *et al.*, Phys. Rev. A , 062509 (2006).

[179] K. L. Corwin, Z. Lu, C. F. Hand, R. J. Epstein, and C. E. Wieman, Applied Optics **37**, 3295 (1998).

[180] V. V. Yashchuk, D. Budker, and J. R. Davis, Rev. Sci. Instrum. **71**, 341 (2000).

[181] L. D. Turner, K. P. Weber, C. J. Hawthorn, and R. E. Scholten, Opt. Comm. **201**, 391 (2002).

[182] K. Razdan and D. A. V. Baak, Am. J. Phys. **70**, 1061 (2002).

[183] C. S. Adams, Rev. Sci. Instrum. **71**, 59 (2000).

[184] K. Singer, S. Jochim, M. Mudrich, A. Mosk, and M. Weidemüller, Rev. Sci. Instrum. **73**, 4402 (2002).

[185] L. P. Maguire, S. Sziagyi, and R. E. Scholten, Rev. Sci. Instrum. **75**, 3077 (2004).

[186] W. Alt, Optik **113**, 142 (2002).

[187] P. F. Griffin, PhD thesis, University of Durham, (2005).

[188] S. R. Granade, M. E. Gehm, K. M. O'Hara, and J. E. Thomas, Phys. Rev. Lett. **88**, 120405 (2002).

[189] D. R. Murray and P. Öhberg, J. Phys. B **38**, 1227 (2005).

[190] P. J. Mohr and B. N. Taylor, Rev. Mod. Phys. **77**, 1 (2005).

[191] U. D. Rapol, A. Krishna, and V. Natarajan, Eur. Phys. J. D **23**, 185 (2003).

[192] D. A. Steck, Rubidium 87 D line data, http://steck.us/alkalidata.

[193] N. R. Claussen *et al.*, Phys. Rev. A **67**, 060701(R) (2003).